General Disclaimer

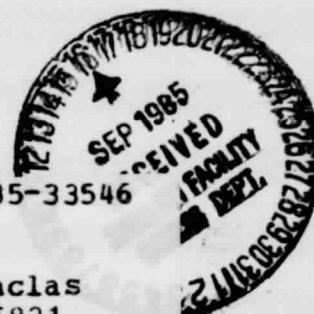## One or more of the Following Statements may affect this Document

NCCI - 15

VIRGINIA TECH

CENTER FOR COMPOSITE MATERIALS AND STRUCTURES

Nonlinear Response and Failure
Characteristics of Internally Pressurized
Composite Cylindrical Panels

Richard L. Boitnott
Eric R. Johnson
James H. Starnes, Jr.
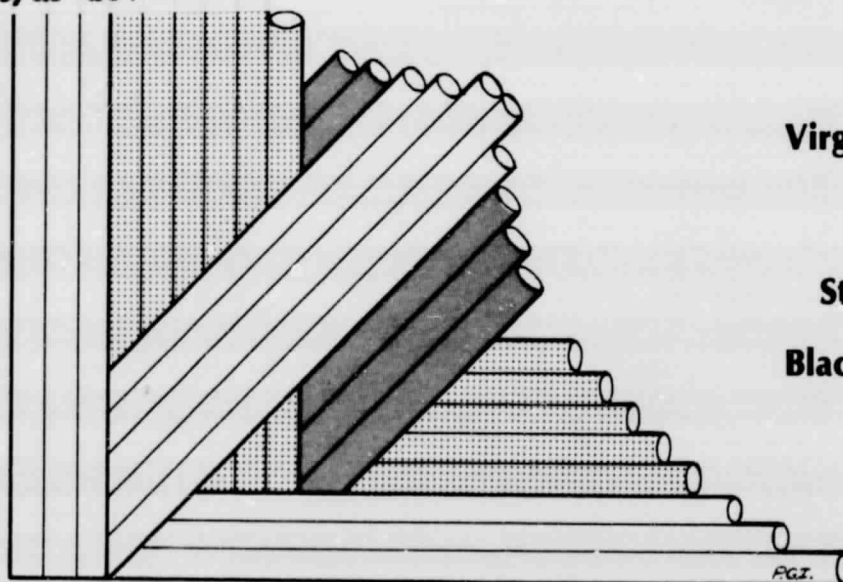
Virginia Polytechnic
Institute
and
State University

Blacksburg, Virginia
24061

P.G.I.

College of Engineering

Virginia Polytechnic Institute and State University

Blacksburg, VA 24061

VPI-E-85-16   June 1985
CCMS-85-07

Nonlinear Response and Failure Characteristics of Internally
Pressurized Composite Cylindrical Panels

Richard L. Boitnott[1]
Eric R. Johnson[2]
James H. Starnes, Jr.[3]

Department of Engineering Mechanics

[1]Research Assistant, Department of Aerospace & Ocean Engineering

[2]Assistant Professor, Department of Aerospace & Ocean Engineering

[3]Structural Mechanics Branch Head, NASA Langley Research Center,
 Hampton, VA

TABLE OF CONTENTS

ii

LIST OF FIGURES

LIST OF TABLES

LIST OF TABLES

Chapter 1

INTRODUCTION

Rising fuel costs have encouraged weight reductions of commercial transport aircraft. Weight reductions of approximately 20-30 percent may occur with the replacement of existing aluminum construction with advanced composite materials. Composite materials offer both high strength- and stiffness-to-weight ratios. Also, the directionality of these composite materials allows designers to tailor the properties of a structure and, thus, design more efficiently. Composite materials have additional advantages over metallic materials in their tension-tension fatigue and corrosion properties.

Although composites offer many inherent advantages over metals, there are still many problems which must be solved before they can be used for primary load carrying structure. Past research has uncovered shortcomings of composites which are not found in metals such as delamination, free edge effects, and poor impact damage tolerance. Much work has been done on the response and failure of composite materials subjected to in-plane loadings. However, little experimental work has been done on composite materials under combined membrane and bending loads. A combined stress state occurs in the skin of a fuselage which is internally pressurized. This internal pressure could be carried most efficiently in a uniform membrane state of stress if the skin were free to expand uniformly in the radial direction. Internal stiffeners necessary to support mechanical loads applied to a fuselage restrain the skin

locally and prevent uniform radial expansion consistent with a membrane state. The pressure-induced deformation of the skin in a typical bay of a stiffened fuselage is illustrated in Figure 1 and is often referred to as "pillowing."

The product of the large pressure-generated membrane tension and change in slope of the skin's reference surface, which results from non-uniform radial expansion, produces a geometrically nonlinear pressure response. This nonlinearity is included in this study and is essential for accurate response prediction. The degree of radial constraint also introduces bending strains which occur in the skin adjacent to the stiffeners. The bending strains, which are a maximum at the panel's edge, combine with the membrane tension strains to initiate failure in the skin.

The primary structural configurations of composite pressure vessel research are thick unstiffened shells which carry very high pressures. Much literature has been published on this research area due to the development of high strength fibers and filament winding techniques. Analysis of these structures using geometrically linear membrane theory is sufficiently accurate for design. Thin stiffened shells such as a fuselage require a different procedure. Bending in addition to membrane action must be included in the analysis of these structures. References 1-7 report on studies of fuselage-type structures under internal pressure. Portions of the material presented in this thesis are documented in Reference 8.
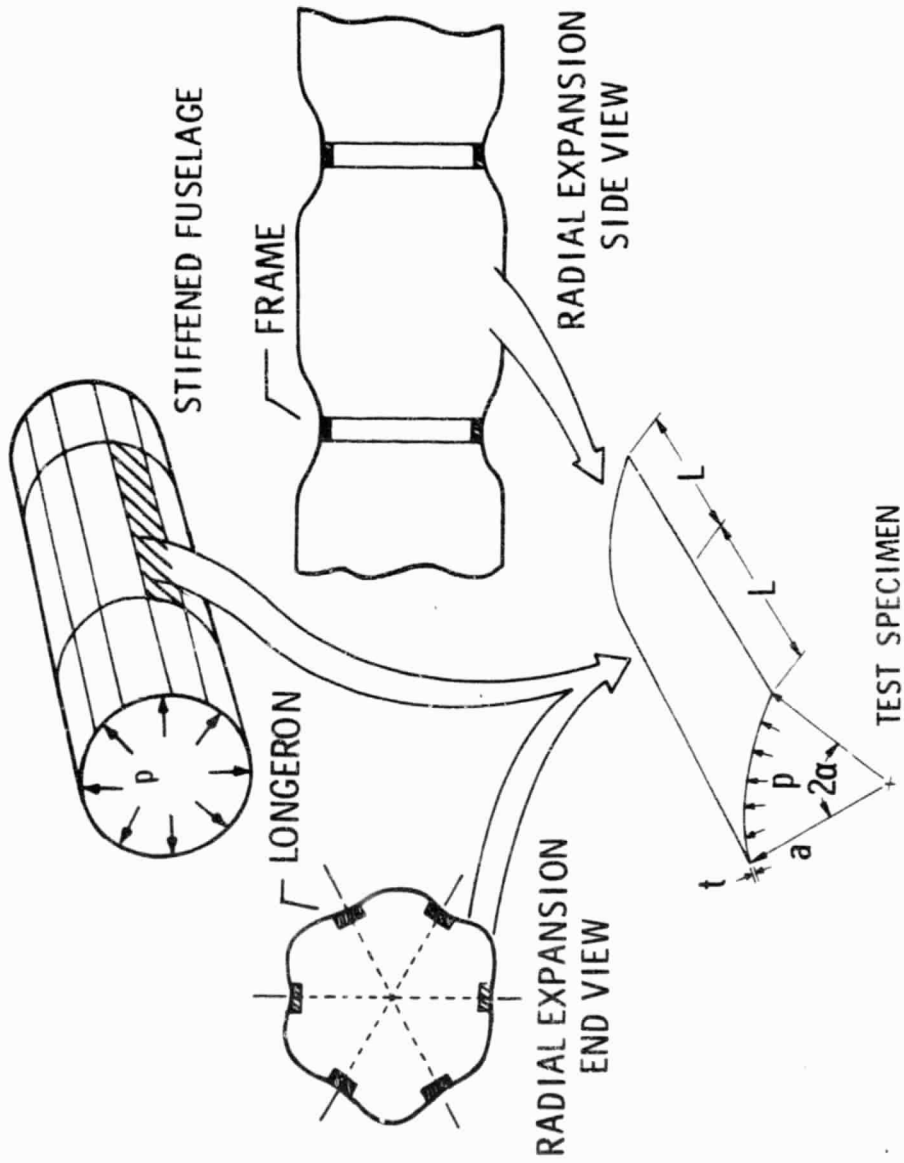
Figure 1.— Test specimen's relationship to an internally pressurized fuselage.

Reference 1 reports on a one-dimensional nonlinear elastic membrane analysis for long flat or slightly curved metal panels. This work illustrates the nonlinear nature of the problem but does not address the severe bending gradients which occur in the fuselage skin at the stiffener support.

Flügge (Ref. 2) addresses a number of problems which arise in the internal pressurization of an airplane fuselage. The importance of the nonlinear response is illustrated by a membrane example similar to that described in Reference 1. Local bending stresses induced by the restraint of the stiffeners on the fuselage skin are not predicted with the membrane approximation of Flügge. Neither can these local bending stresses be correctly examined with a linear axisymmetric approximation of the pressurized fuselage as used by Flügge. In this approximation the skin and longerons are lumped together to obtain an equivalent "smeared" orthotropic shell with the individual rings modeled discretely. Skin bending adjacent to a ring will not be properly predicted with this approach and bending adjacent to a longeron is not allowed by the analysis.

Additional axisymmetric analyses are included in References 3 and 4. Williams (Ref. 4) included in his analysis the important geometric nonlinear term which accounts for the product of the in-plane axial load and slope in the radial equilibrium equation. However, the importance of the nonlinear effect of this term is lost when "smeared" longeron theory is used which makes the skin effectively very thick and the contributions of the nonlinear term small. This approach therefore

does not accurately address the "pillowing" which results in local skin bending.

Wang (Ref. 5) modeled the fuselage as a shell connected to discrete internal rings and stringers. The analysis was linear; and it was assumed that the interaction between elements consisted only of normal stresses, thus excluding shear. Series solutions were used to satisfy the equilibrium equations for each individual component. Displacement compatibility between the individual elements couples these elements and allows for the determination of the interaction forces. This analysis for isotropic materials does address "pillowing" effects but geometrically linear behavior is assumed. Linear behavior would become more appropriate as the skin thickness increases or as the stiffnesses of the frames and longerons decrease.

Formulas are given in Reference 6 for stresses in an isotropic skin adjacent to individual frames and longerons. Although the details of the derivation are not discussed nor a reference given, nonlinear terms are apparent in the formulas given.

Reference 7 reported axial and circumferential strain distributions for a typical bay of a composite stiffened circular cylindrical shell under internal pressure. These results were generated from a Lockheed in-house computer program. The analysis developed by Wang (Reference 5) has been extended to include composite skins. The analysis is again linear with numerical results given for a fuselage skin laminate at an ultimate ground test condition of 17.63 psi.

References 1-7 all deal with pressurization of a fuselage but none show how the geometric nonlinearities effect the severity of the bending gradients in a composite skin adjacent to a stiffener. Only Reference 6 has experimental pressurization results. This work is on large scale stiffened adhesively bonded aluminum fuselage structures and does not as such focus on the response of the skin. For panels with longitudinal cracks in the center of the bay, the crack propagated until it met a frame and turned and ran parallel to the frame along its intersection with the skin. For aluminum pressurized panels, the high stresses which occurs in the local bending gradient are relieved by material yielding. For composite panels, strain relief must come primarily from other sources such as transverse matrix cracking, local fiber failure, and delamination.

In the edge bending gradient region, interlaminar stresses become large and must be examined because of inherent transverse strength weaknesses of composites. The majority of references on interlaminar stresses is directed towards the free edge problem of a composite laminate. References 9 and 10 examine the distribution of interlaminar stresses near the supported edges of composite circular cylinders under internal pressure. Linear shell analysis was used on a layer-by-layer basis to determine the axial distribution of interlaminar stresses for clamped or simply supported axial boundary conditions. Because linear theory was used in the above studies, the same response characteristics would be found at any pressure. The response character will vary with pressure when geometrically nonlinear behavior is considered.

A one-dimensional approach is used in the present study to concen-
trate on the nonlinearities and local skin bending important in a pres-
surized fuselage skin. The skin is approximated by an infinitely long
shallow cylindrical panel. This geometry approximates typical fuselage
skin bays which are long in the axial direction relative to their cir-
cumferential arc length. In addition to the in-plane circumferential
stresses, interlaminar stress distributions are examined. Nonlinear
equations of elasticity, which include geometric shallowness and
Donnell's approximations, are integrated to determine the interlaminar
stresses. Past research has not examined these stresses with geometric
nonlinearities considered.

Experiments were conducted to verify the analysis and identify the
ultimate failure pressures and modes. Comparison between analysis and
experiment points out the range of applicability of the analysis. The
test article is a shallow cylindrical panel of the same approximate
dimensions as a typical fuselage skin panel. Under internal pressure
the radial deflections of the fuselage skin are symmetrically dis-
tributed along lines perpendicular to the frames and longerons as shown
in Figure 1. Because of this symmetry the slope of the deflection curve
normal to the boundary is zero. To approximate this slope condition,
curved graphite-epoxy and aluminum panels were tested in a fixture with
clamped edges. The outward radial deflections at the stiffeners of an
actual fuselage were not duplicated in the experiment. The panels were
constructed of 4, 5, 8, or 16 plies of unidirectional graphite-epoxy
tape to illustrate a range of responses and failures.

Chapter 2

EXPERIMENTAL PROGRAM

2.1 Test Specimens

The materials used in this study include 2024-T3 aluminum and commercially available 0.005-inch-thick unidirectional Thornel 300 graphite fiber tapes preimpregnated with 350°F cure Narmco 5208 thermo- setting epoxy resin referred to as T300-5208 graphite-epoxy. The aluminum panels were cut to size from flat sheets which had nominal thicknesses of 0.020 and 0.040 inches. Unidirectional preimpregnanted tape was layed up on a smooth cylindrical surface with a 60 inch radius at specified orientations to form uncured laminates. These panels were cured in an autoclave following the resin manufacturer's recommendations and then inspected with ultrasonic C-scan. Typical lamina properties are 19.0 msi for the longitudinal Young's modulus E_{11}, 1.89 msi for the transverse Young's modulus E_{22}, 0.93 msi for the in-plane and shearing deformation moduli G_{12} and G_{13}, 0.60 msi for the shearing deformation modulus G_{23}, and 0.38 for the major Poisson's ratio ν_{12}. The panels and their stacking sequence are shown in Table 1. The aluminum specimens are designated specimens A1 and A2 and the graphite-epoxy specimens are designated G1 through G11.

After trimming the panels to an approximate size of 23 inches by 11 inches, bolt holes were drilled around the panel's edge for securing the panel to the fixture as shown in Figure 2. A special drill fix- ture was used for drilling thirty-two 0.25-inch holes into each panel.

8

Table 1. Test Specimens

Specimen	Number of Plies	Thickness, in.	Laminate Stacking Sequence
A1	1	0.0203	2024-T3 Aluminum
A2	1	0.0389	2024-T3 Aluminum
G1	4	0.0206	$[\pm 45]_s$
G2	4	0.0207	$[\pm 45]_s$
G3	5	0.0251	$[\pm 45/\overline{90}]_s$
G4	5	0.0247	$[\pm 45/\overline{90}]_s$
G5	8	0.0387	$[90/\pm 45/0]_s$
G6	8	0.0397	$[90/0/\pm 45]_s$
G7	8	0.0400	$[90/0/\pm 45]_s$
G8	8	0.0912	$[\pm 45]_{2s}$
G9	16	0.0901	$[\pm 45/\pm 45/90_2/0_2]_s$
G10	16	0.0880	$[90_2/\pm 45/\pm 45/0_2]_s$
G11	16	0.0893	$[90_2/0_2/\pm 45/\pm 45]_s$
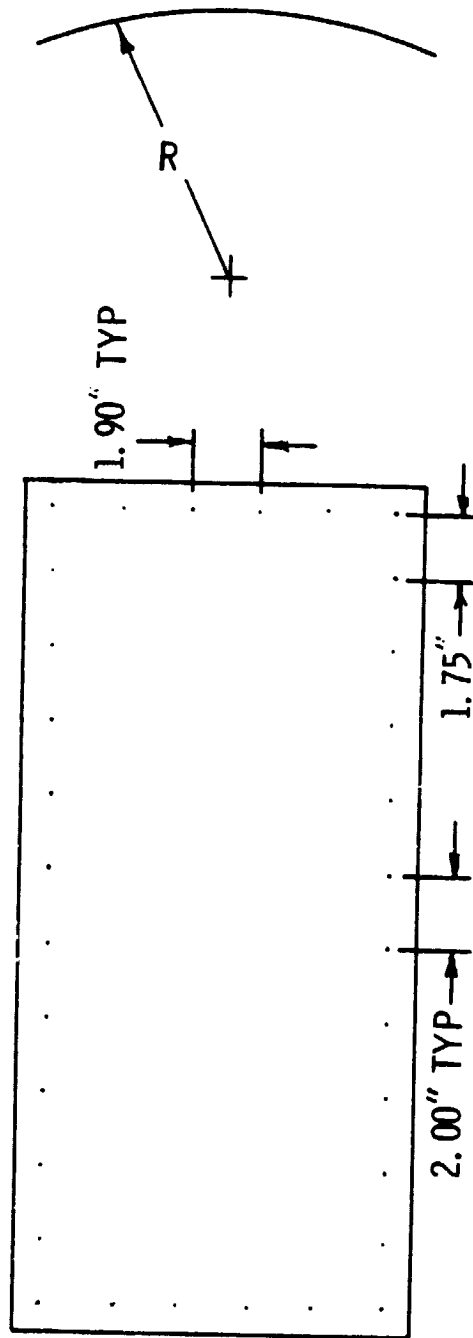
Figure 2.- Machined bolt hole pattern in test specimen for clamping specimen to test fixture.

The drill fixture consists of a top and bottom part. The trimmed panels were placed between the two curved surfaces of the drill fixture for drilling the holes. Force was applied to the top and bottom parts of the drill fixture with C-clamps to force the panel into an untwisted 60 inch radius configuration and to prevent any movement during the drilling operation.

The drill fixture design had an important effect on the circumferential distance between bolt holes of different thickness panels. The drill fixture design provided for constant opening angles between the arc-wise position of the bolt holes drilled in all the panels. However, it did not compensate for the various panel thicknesses. Thus differences occur in the middle surface arc lengths between the bolt holes used in clamping the straight edge. The middle surface arc length difference between the thickest panel (0.080 in. nominal) and the thinnest panel (0.020 in. nominal) was predicted to be approximately 0.004 in. Although this difference may seem like a minor variation in the middle surface arc length, it will be shown later that small changes in the arc length for shallow panels can result in very large changes in the middle surface radius.

Fiberglass tabs of uniform thickness (approximately 0.1 in.) were used to reinforce the bolt holes against bearing failure along the straight edges of the panels. These flat tabs measured 1.5 in. in width and 20 in. in length and were drilled separately and bonded onto the convex surface of the predrilled composite panels.

To measure the bending gradient away from the clamped edges, the panels were instrumented with strain gages. Back-to-back strain gages were bonded to the panels from the edges to the center along the circumferential and axial center lines of the panel. Because of the rapid strain variation at the panel's edge, strain gages with short gage lengths were located as close as possible to the clamped boundary to determine the best pointwise estimate of the edge strains. Gages with an effective gage length of 0.015 inches were used close to the edge. Since the strains were almost constant outside the edge bending boundary layer, larger gages could be used away from the edge. These strain gages had an effective gage length of 0.187 inches.

2.2 Test Apparatus

The test apparatus consisted of the test fixture, pressure source, and instrumentation. A cross sectional drawing of the assembled test fixture is shown in Figure 3. The test fixture consists of three components: test frame, strain gage lead feed-through panel, and top clamping bars. The test frame was machined from a solid steel block and has a 60-inch radius machined surface around the edges where the curved panels were clamped. The strain gage lead feed-through panel allows recording a maximum of 16 strain gages bonded to the panel concave surface. The feed-through panel allows the strain gage signals to be transmitted out of the pressurized interior of the test fixture. The feed-through panel also has an inlet port for the pressurizing media, a bleed valve, and a pressure transducer port. Six bars were used for
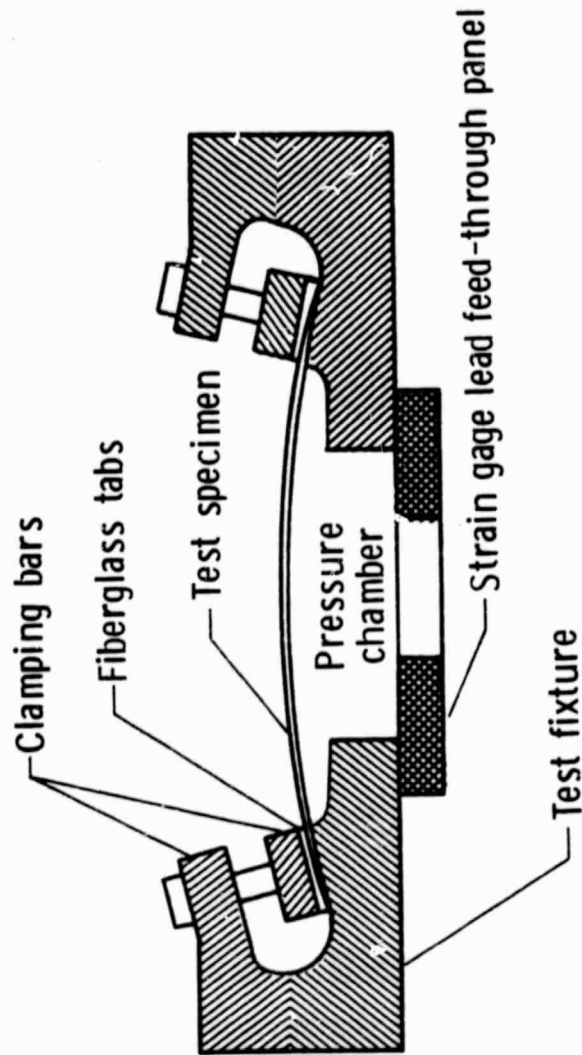
Figure 3.— Cross section of test specimen in test fixture.

clamping the specimen to the fixture. These include two straight bars

and two curved bars, rectangular in cross section, which were used to

clamp the panel to the test frame. Thirty-two 0.25-inch bolts secured

these bars and the test panel to the test frame. These bolts were

torqued to 100 in-lb. Two larger bars, L-shaped in cross section,

allowed application of very large normal forces to the straight edges of

the panel in an attempt to minimize in-plane slippage of the panels in

the clamped support. The bolts which passed through the flange of the

larger bars are tightened down on the smaller bar as shown in Figure 3.

A photograph of a failed test specimen assembled in the test fixture is

shown in Figure 4. The L-shaped bars are not shown in the photograph.

During the course of the experimental program various methods were

used to pressurize the curved panels. Pressure sources include the use

of low pressure shop air (to 50 psi), city water (to 60 psi), an

1800 psi bottled nitrogen source, and a hydrostatic tester. A pressure

regulator between the pressure source and the interior of the test panel

was used to control the pressure.

After the manufacturing and drilling of the composite curved pan-

els, their shapes deviated from the desired 60-inch radius right cir-

cular cylinder. Therefore, geometric imperfection equipment was used to

measure the initial shape of the curved panels. A DCDT (direct-current

displacement transducer) was fixed to a trolley which rolled on

straight, flat rails. Scans of the panels were made in the two direc-

tions parallel to the supports to determine the true geometry of the

panels.
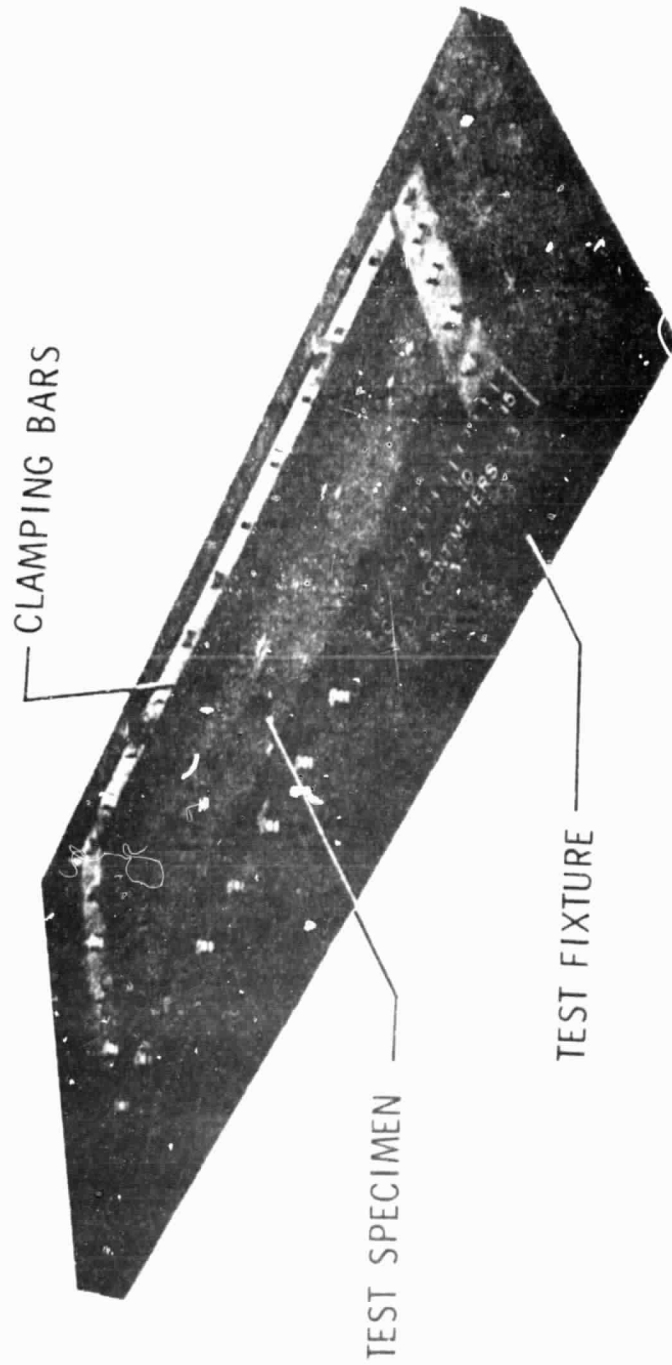
Figure 4.- Test specimen clamped in test fixture.

The test procedure consisted of the following steps. A panel was placed in the test fixture and the clamping bars were torqued symmetrically. Next, the panels were surveyed with the geometric imperfection measuring equipment. The imperfection measuring equipment was removed and DCDT's were positioned normal to the panels surface at selected points along the axial and circumferential centerlines to monitor displacements of the panels to the applied pressure. Pressure was increased until failure of the panels occurred. Digital strain, displacement, and pressure data were recorded on a data acquisition system.

Chapter 3

ANALYSIS

In this chapter the energy method is used to derive two sets of geometrically nonlinear equilibrium equations for the response of cylindrical panels to internal pressurization. For a set of nonlinear strain-displacement equations, elasticity equations are derived in Section 3.1. Using the same set of nonlinear strain-displacement equations and explicit assumptions for the displacement variation as a function of the thickness coordinate z, shell equations are derived in Section 3.2 which account for through-the-thickness shearing deformations. In Section 3.3 the two-dimensional shell equations are reduced to a one-dimensional set of ordinary differential equations in the circumferential coordinate by assuming that the stress resultants are independent of the axial coordinate. The reduction to a one-dimensional set of equations is appropriate for the response of a panel which is long in the axial direction. Closed form solutions to the nonlinear ordinary differential equations are obtained which include transverse shear deformation effects and twist-curvature coupling of laminated composite panels. The one-dimensional solution provides details of the bending gradient response near the straight edge of the panel. In Section 3.4 through-the-thickness shear and normal stresses are obtained in this bending boundary layer that contains the bending gradient. These stresses are determined by substituting the in-plane stresses and radial deflection from the one-dimensional shell solution into the

Chapter 3

ANALYSIS

In this chapter the energy method is used to derive two sets of
geometrically nonlinear equilibrium equations for the response of
cylindrical panels to internal pressurization. For a set of nonlinear
strain-displacement equations, elasticity equations are derived in
Section 3.1. Using the same set of nonlinear strain-displacement equa-
tions and explicit assumptions for the displacement variation as a
function of the thickness coordinate z, shell equations are derived in
Section 3.2 which account for through-the-thickness shearing deforma-
tions. In Section 3.3 the two-dimensional shell equations are reduced
to a one-dimensional set of ordinary differential equations in the
circumferential coordinate by assuming that the stress resultants are
independent of the axial coordinate. The reduction to a one-dimensional
set of equations is appropriate for the response of a panel which is
long in the axial direction. Closed form solutions to the nonlinear
ordinary differential equations are obtained which include transverse
shear deformation effects and twist-curvature coupling of laminated
composite panels. The one-dimensional solution provides details of the
bending gradient response near the straight edge of the panel. In
Section 3.4 through-the-thickness shear and normal stresses are obtained
in this bending boundary layer that contains the bending gradient.
These stresses are determined by substituting the in-plane stresses and
radial deflection from the one-dimensional shell solution into the

17

elasticity equations derived in Section 3.1. The stresses in the elasticity equations are also assumed independent of the axial coordinate to be consistent with the one-dimensional shell solution. Finally, in Section 3.5 a strength of materials solution is presented for the nonlinear response of an internally pressurized cylindrical membrane which is long in the axial direction.

3.1 Three-Dimensional Elasticity Equations

Elasticity equilibrium equations will be used to determine the transverse stresses in Section 3.4 after the shell solution is obtained in Section 3.3. However, these equations are developed before the shell equations since an elasticity formulation has fewer assumptions, and hence, is less restrictive than a shell formulation.

Figure 5 shows the middle surface or reference surface of the circular cylindrical panel. The shell coordinates shown are the axial coordinate x, circumferential coordinate θ, and the thickness coordinate z. The origin is at the center of the middle surface such that $-L < X < L$, $-\alpha < \theta < \alpha$, and $-t/2 < z < t/2$, where 2L is the length of the panel, α is the semi-opening angle, and t is the thickness. The radius of the circular arc on the middle surface is designated by a.

Let u, v, and w designate displacements in the axial, circumferential, and thickness directions, respectively, of a material point in the panel. The normal strains are denoted by ε_{xx}, $\varepsilon_{\theta\theta}$, and ε_{zz}, and the engineering shear strains are denoted by $\gamma_{\theta z}$, γ_{xz}, and $\gamma_{x\theta}$.

19
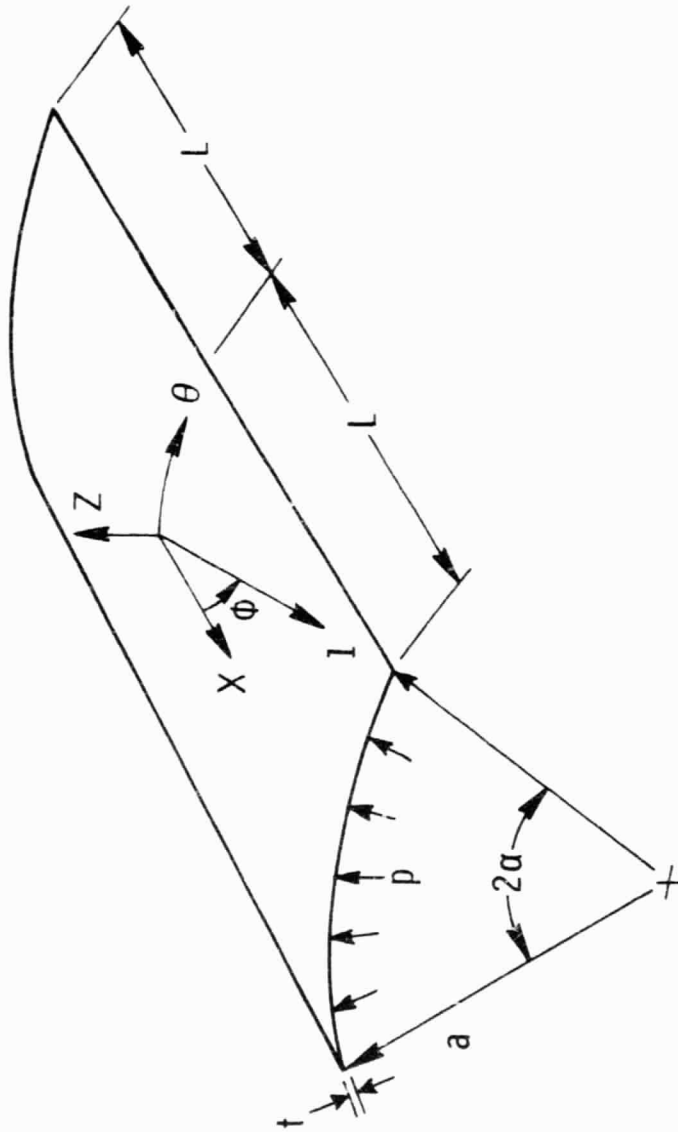
Figure 5.- Shell geometry, dimensions and coordinate system.

The strains are assumed to be small, and the rotations are assumed to be moderately small. On a surface parallel to the middle surface, the rotations of the axial and circumferential line elements out of the tangent plane are assumed to be larger than the rotations about the normal, such that rotations about the normal are neglected. Since the panel is shallow, the contribution of the circumferential displacement to the rotation of the circumferential line element out of the tangent plane is neglected (Donnell-Mushtari-Vlasov approximation). Sanders (Ref. 11) presents kinematic relations for the surface strains in general curvilinear coordinates under these assumptions. Specialized to cylindrical coordinates Sanders kinematic relations are

$$\epsilon_{xx} = \frac{\partial u}{\partial x} + \frac{1}{2}\left(\frac{\partial w}{\partial x}\right)^2$$

$$\epsilon_{\theta\theta} = \frac{1}{r}\frac{\partial v}{\partial \theta} + \frac{w}{r} + \frac{1}{2}\left(\frac{1}{r}\frac{\partial w}{\partial \theta}\right)^2 \tag{3.1}$$

$$\gamma_{x\theta} = \frac{\partial v}{\partial x} + \frac{1}{r}\frac{\partial u}{\partial \theta} + \frac{\partial w}{\partial x}\frac{1}{r}\frac{\partial w}{\partial \theta},$$

where $r = a + z$ is the radius of a surface parallel to the middle surface. The transverse kinematic relations are assumed to be given by

$$\gamma_{\theta z} = \frac{\partial v}{\partial z} + \frac{1}{r} \frac{\partial w}{\partial \theta}$$

$$\gamma_{xz} = \frac{\partial w}{\partial x} + \frac{\partial u}{\partial z} \tag{3.2}$$

$$\varepsilon_{zz} = \frac{\partial w}{\partial z}.$$

The panel is thin, such that $a \gg t > |z|$. Thus in equations (3.1) and (3.2) the radius r is replaced by the radius a of the middle surface.

The potential energy for the panel is

$$V = U - W, \tag{3.3}$$

where U is the strain energy and W is the work of the prescribed surface tractions. Body forces are neglected. Let σ_{xx}, $\sigma_{\theta\theta}$, and σ_{zz} denote the normal stress components in the panel, and let $\tau_{\theta z}$, τ_{xz}, and $\tau_{x\theta}$ denote the shear stress components. The strain energy for a linear elastic thin shell is

$$U = \frac{1}{2} \int_{-t/2}^{t/2} \int_{-\alpha}^{\alpha} \int_{-L}^{L} [\varepsilon_{xx} \, \sigma_{xx} + \varepsilon_{\theta\theta} \, \sigma_{\theta\theta} + \varepsilon_{zz} \, \sigma_{zz}$$

$$+ \gamma_{\theta z} \, \tau_{\theta z} + \gamma_{xz} \, \tau_{xz} + \gamma_{x\theta} \, \tau_{x\theta}] \, dx \, ad\theta \, dz \tag{3.4}$$

The prescribed surface traction components at $x = \pm L$ are denoted $\bar{\sigma}_{xx}$, $\bar{\tau}_{x\theta}$, and $\bar{\tau}_{xz}$. The overbar notation is also used for the prescribed surface traction components at $\theta = \pm\alpha$ and $z = \pm t/2$. The prescribed tractions are treated as dead loads in the energy formulation.

Although hydrostatic pressure is not a dead load, it is conservative, and may be approximated by a dead load potential (Ref. 12) for a shallow panel. Thus, the work done by the prescribed tractions is

$$
W = \int_{-L}^{L} \int_{-\alpha}^{\alpha} \left(\bar{\tau}_{xz} \, u + \bar{\tau}_{\theta z} \, v + \bar{\sigma}_{zz} \, w \right) \Bigg|_{z=-t/2}^{z=t/2} a \, d\theta \, dx
$$

$$
+ \int_{-t/2}^{t/2} \int_{-L}^{L} \left(\bar{\tau}_{x\theta} \, u + \bar{\sigma}_{\theta\theta} \, v + \bar{\tau}_{\theta z} \, w \right) \Bigg|_{\theta=-\alpha}^{\theta=\alpha} dx \, dz
$$

$$
+ \int_{-t/2}^{t/2} \int_{-\alpha}^{\alpha} \left(\bar{\sigma}_{xx} \, u + \bar{\tau}_{x\theta} \, v + \bar{\tau}_{xz} \, w \right) \Bigg|_{x=-L}^{x=L} a \, d\theta \, dz \qquad (3.5)
$$

where the internal hydrostatic pressure p is equal to $-\bar{\sigma}_{zz}$ at $z = t/2$.

Equilibrium equations and boundary conditions for the thin shallow cylindrical panel are obtained from stationarity of the potential energy, i.e., $\delta V = 0$. Combining equations (3.3), (3.4), and (3.5) with the approximate kinematic relations (3.1) and (3.2), the first variation in the potential energy, after integrating by parts, is

$$\delta V = \frac{1}{2} \int_{-t/2}^{t/2} \int_{-L}^{L} \int_{-\alpha}^{\alpha} \left\{ \left[-\frac{\partial \sigma_{xx}}{\partial x} - \frac{1}{a} \frac{\partial \tau_{x\theta}}{\partial \theta} - \frac{\partial \tau_{xz}}{\partial z} \right] \delta u \right.$$

$$+ \left[-\frac{\partial \tau_{x\theta}}{\partial x} - \frac{1}{a} \frac{\partial \sigma_{\theta\theta}}{\partial \theta} - \frac{\partial \tau_{\theta z}}{\partial z} \right] \delta v + \left[-\frac{\partial \tau_{xz}}{\partial x} - \frac{1}{a} \frac{\partial \tau_{\theta z}}{\partial \theta} \right.$$

$$- \frac{\partial \sigma_{zz}}{\partial z} + \frac{1}{a} \sigma_{\theta\theta} - \frac{\partial}{\partial x} \left(\sigma_{xx} \frac{\partial w}{\partial x} \right) - \frac{1}{a} \frac{\partial}{\partial \theta} \left(\frac{\sigma_{\theta\theta}}{a} \frac{\partial w}{\partial \theta} \right)$$

$$\left. \left. - \frac{\partial}{\partial x} \left(\tau_{x\theta} \frac{1}{a} \frac{\partial w}{\partial \theta} \right) - \frac{1}{a} \frac{\partial}{\partial \theta} \left(\tau_{x\theta} \frac{\partial w}{\partial x} \right) \right] \delta w \right\} a d\theta \, dx dz$$

$$+ \int_{-t/2}^{t/2} \int_{-\alpha}^{\alpha} \left[\left(\sigma_{xx} - \bar{\sigma}_{xx} \right) \delta u + \left(\tau_{x\theta} - \bar{\tau}_{x\theta} \right) \delta v \right.$$

$$+ \left. \left(\tau_{xz} + \sigma_{xx} \frac{\partial w}{\partial x} + \tau_{x\theta} \frac{1}{a} \frac{\partial w}{\partial \theta} - \bar{\tau}_{xz} \right) \delta w \right] \Bigg|_{x=-L}^{x=L} a d\theta \, dz$$

$$+ \int_{-t/2}^{t/2} \int_{-L}^{L} \left[\left(\tau_{x\theta} - \bar{\tau}_{x\theta} \right) \delta u + \left(\sigma_{\theta\theta} - \bar{\sigma}_{\theta\theta} \right) \delta v \right.$$

$$+ \left. \left(\tau_{\theta z} + \sigma_{\theta\theta} \frac{1}{a} \frac{\partial w}{\partial \theta} + \tau_{x\theta} \frac{\partial w}{\partial x} - \bar{\tau}_{\theta z} \right) \delta w \right] \Bigg|_{\theta=-\alpha}^{\theta=\alpha} dx dz$$

$$+ \int_{-L}^{L} \int_{-\alpha}^{\alpha} \left[\left(\tau_{xz} - \bar{\tau}_{xz} \right) \delta u + \left(\tau_{\theta z} - \bar{\tau}_{\theta z} \right) \delta v \right.$$

$$+ \left. \left(\sigma_{zz} - \bar{\sigma}_{zz} \right) \delta w \right] \Bigg|_{z=-t/2}^{z=t/2} a d\theta \, dx = 0 \qquad (3.6)$$

Since the variations δu, δv, and δw are completely arbitrary, equation (3.6) can vanish only if the coefficients of each variation vanish individually. From this reasoning the three equations of elasticity for equilibrium in the x, θ, and z direction are

$$\frac{\partial \sigma_{xx}}{\partial x} + \frac{1}{a} \frac{\partial \tau_{x\theta}}{\partial \theta} + \frac{\partial \tau_{xz}}{\partial z} = 0$$

$$\frac{\partial \tau_{x\theta}}{\partial x} + \frac{1}{a} \frac{\partial \sigma_{\theta\theta}}{\partial \theta} + \frac{\partial \tau_{\theta z}}{\partial z} = 0 \tag{3.7}$$

$$\frac{\partial \tau_{xz}}{\partial x} + \frac{1}{a} \frac{\partial \tau_{\theta z}}{\partial \theta} + \frac{\partial \sigma_{zz}}{\partial z} - \frac{1}{a} \sigma_{\theta\theta} + \frac{\partial}{\partial x} \left(\sigma_{xx} \frac{\partial w}{\partial x} \right)$$

$$+ \frac{1}{a} \frac{\partial}{\partial \theta} \left(\frac{\sigma_{\theta\theta}}{a} \frac{\partial w}{\partial \theta} \right) + \frac{\partial}{\partial x} \left(\frac{\tau_{x\theta}}{a} \frac{\partial w}{\partial \theta} \right) + \frac{1}{a} \frac{\partial}{\partial \theta} \left(\tau_{x\theta} \frac{\partial w}{\partial x} \right) = 0$$

The nonlinearities appear in the z-direction equilibrium equation only, which is the third equation in (3.7).

The vanishing of the first variation also leads to boundary conditions on the surfaces of the panel. Since the equilibrium equations are used to estimate the transverse stress components, only the conditions on the upper and lower surfaces are needed. Thus, conditions on the surfaces at $x = \pm L$ and $\theta = \pm \alpha$ are omitted. At $z = \pm t/2$ the following are prescribed

$$\tau_{xz} \quad \text{or} \quad u,$$

$$\tau_{\theta z} \quad \text{or} \quad v, \tag{3.8}$$

$$\sigma_{zz} \quad \text{or} \quad w.$$

3.2 Two-Dimensional Shell Equations

3.2.1 Kinematic Relations

The assumptions of geometric shallowness, small strains, and moderate rotations were used in the derivation of the elasticity equations. In this section a shell theory will be derived from the variational principle (3.6) by assuming the z-direction dependence of the displacements. Normals to the reference surface before deformation are assumed to remain straight and unchanged in length but not necessarily normal to the deformed reference surface. This assumption allows through-the-thickness shear deformation of the Mindlin type (Ref. 14) to occur which is important for composite materials where the ratio of shearing deformation modulus to in-plane extensional modulus is low (1/20-1/30). This assumption implies that the in-plane displacements u and v vary linearly through the thickness. Let u^{o} and v^{o} represent the displacements u and v on the middle surface ($z = 0$), and let Ψ_x and Ψ_θ designate the rotations of the middle surface normal about the θ-axis and x-axis, respectively. Then the displacement field for the shell theory has the form

$$u(x, \theta, z) = u^{o}(x, \theta) + z \, \Psi_x(x, \theta)$$

$$v(x, \theta, z) = v^{o}(x, \theta) + z \, \Psi_\theta(x, \theta) \tag{3.9}$$

$$w(x, \theta, z) = w^{o}(x, \theta)$$

Substituting the displacements (3.9) into the strain-displacement
relations (3.1) and (3.2) results in the following expressions

$$\epsilon_{xx} = \epsilon_{xx}^c + z\ \Gamma_{xx}$$

$$\epsilon_{\theta\theta} = \epsilon_{\theta\theta}^o + z\ \Gamma_{\theta\theta}$$

$$\gamma_{x\theta} = \gamma_{x\theta}^o + z\ \Gamma_{x\theta}$$

$$\gamma_{\theta z} = \gamma_{\theta z}^o$$ (3.10)

$$\gamma_{xz} = \gamma_{xz}^o$$

$$\epsilon_{zz} = \epsilon_{zz}^o = 0,$$

in which the middle surface strain-displacement relations are

$$\epsilon_{xx}^o = \frac{\partial u^o}{\partial x} + \frac{1}{2}\left(\frac{\partial w^o}{\partial x}\right)^2$$

$$\epsilon_{\theta\theta}^o = \frac{1}{a}\frac{\partial v^o}{\partial\theta} + \frac{w^o}{a} + \frac{1}{2}\left(\frac{1}{a}\frac{\partial w^o}{\partial\theta}\right)^2$$ (3.11)

$$\gamma_{x\theta}^o = \frac{\partial v^o}{\partial x} + \frac{1}{a}\frac{\partial u^o}{\partial\theta} + \frac{\partial w^c}{\partial x}\frac{1}{a}\frac{\partial w^o}{\partial\theta},$$

and where the transverse strains and rotation gradients are

$$\gamma^o_{\theta_z} = \Psi_\theta + \frac{1}{a}\frac{\partial w^o}{\partial \theta}$$

$$\gamma^o_{xz} = \frac{\partial w^o}{\partial x} + \Psi_x$$

$$\Gamma_{xx} = \frac{\partial \Psi_x}{\partial x} \hspace{5cm} (3.12)$$

$$\Gamma_{\theta\theta} = \frac{1}{a}\frac{\partial \Psi_\theta}{\partial \theta}$$

$$\Gamma_{x\theta} = \frac{\partial \Psi_\theta}{\partial x} + \frac{1}{a}\frac{\partial \Psi_x}{\partial \theta}.$$

3.2.2 Shell Equilibrium Equations

The assumptions for the displacements (3.9) are substituted into the first variation of the potential energy (3.6) and explicit integration in the thickness coordinate z from $-t/2$ to $+t/2$ is carried out. In this process weighted integrals of the stresses in z occur. These integrals are interpreted as stress resultants and stress couples in shell theory. The stress resultants and couples, defined per unit arc length on the reference surface, are

$$(N_x, N_\theta, N_{x\theta}) = \int_{-t/2}^{t/2} (\sigma_x, \sigma_\theta, \tau_{x\theta}) \, dz$$

$$(Q_x, Q_\theta) = \int_{-t/2}^{t/2} (\tau_{xz}, \tau_{\theta z}) \, dz \tag{3.13}$$

$$(M_x, M_\theta, M_{x\theta}) = \int_{-t/2}^{t/2} (\sigma_x, \sigma_\theta, \tau_{x\theta}) \, z \, dz.$$

After performing the integration through the thickness, and using the stress resultant definitions (3.13), the vanishing of the first varia-tion of the potential energy leads to the equilibrium equations

$$\frac{\partial N_x}{\partial x} + \frac{1}{a} \frac{\partial N_{x\theta}}{\partial x} + [\tau_{xz}(+t/2) - \tau_{xz}(-t/2)] = 0$$

$$\frac{1}{a} \frac{\partial N_\theta}{\partial \theta} + \frac{\partial N_{x\theta}}{\partial x} + [\tau_{\theta z}(+t/2) - \tau_{\theta z}(-t/2)] = 0$$

$$\frac{\partial}{\partial x}\left(N_x \frac{\partial w}{\partial x}\right) - \frac{N_\theta}{a} + \frac{1}{a} \frac{\partial}{\partial \theta}\left(\frac{N_\theta}{a} \frac{\partial w}{\partial \theta}\right) + \frac{1}{a} \frac{\partial Q_\theta}{\partial \theta} \qquad (3.14)$$

$$+ \frac{\partial Q_x}{\partial x} + \frac{1}{a} \frac{\partial}{\partial \theta}\left(N_{x\theta} \frac{\partial w}{\partial x}\right) + \frac{\partial}{\partial x}\left(\frac{N_{x\theta}}{a} \frac{\partial w}{\partial \theta}\right)$$

$$+ [\sigma_{zz}(+t/2) - \sigma_{zz}(-t/2)] = 0$$

$$\frac{\partial M_x}{\partial \theta} + \frac{1}{a} \frac{\partial M_{x\theta}}{\partial \theta} - Q_x + \frac{t}{2}[\tau_{xz}(t/2) + \tau_{xz}(-t/2)] = 0$$

$$\frac{1}{a} \frac{\partial M_\theta}{\partial \theta} + \frac{\partial M_{x\theta}}{\partial x} - Q_\theta + \frac{t}{2}[\tau_{\theta z}(t/2) + \tau_{\theta z}(-t/2)] = 0.$$

The shell boundary conditions, which result from the integrated form of the first variation of the potential energy, consist of five conditions along each edge. At $x = \pm L$ the following are prescribed

$$N_x = \bar{N}_x \quad \text{or} \quad u^o = \bar{u}^o,$$

$$M_x = \bar{M}_x \quad \text{or} \quad \Psi_x = \bar{\Psi}_x,$$

$$N_{x\theta} = \bar{N}_{x\theta} \quad \text{or} \quad v^o = \bar{v}^o, \tag{3.15}$$

$$M_{x\theta} = \bar{M}_{x\theta} \quad \text{or} \quad \Psi_\theta = \bar{\Psi}_\theta,$$

$$Q_x + N_x \frac{\partial w}{\partial x} + \frac{N_{x\theta}}{a} \frac{\partial w}{\partial \theta} = \bar{Q}_x \quad \text{or} \quad w^o = \bar{w}^o.$$

at $\theta = \pm\alpha$ the following are prescribed

$$N_{x\theta} = \bar{N}_{x\theta} \quad \text{or} \quad u^o = \bar{u}^o,$$

$$M_{x\theta} = \bar{M}_{x\theta} \quad \text{or} \quad \Psi_x = \bar{\Psi}_x,$$

$$N_\theta = \bar{N}_\theta \quad \text{or} \quad v^o = \bar{v}^o, \tag{3.16}$$

$$M_\theta = \bar{M}_\theta \quad \text{or} \quad \Psi_\theta = \bar{\Psi}_\theta,$$

$$Q_\theta + \frac{N_\theta}{a} \frac{\partial w}{\partial \theta} + N_{x\theta} \frac{\partial w}{\partial x} = \bar{Q}_\theta \quad \text{or} \quad w^o = \bar{w}^o.$$

The shell equilibrium equations (3.14) can be obtained from the elasticity equilibrium equations (3.7) by integrating the latter equations through the thickness. For example, if the last equation in

equations (3.7) is first integrated in z from $-t/2$ to $t/2$, and secondly it is multiplied by z and integrated from $-t/2$ to $t/2$, then the first and fourth equations in equations (3.14) are obtained when the resultant definition in equations (3.13) are used. This fact is significant for the estimations of the through-the-thickness stress components τ_{xz}, $\tau_{\theta z}$, and σ_z from equations (3.7) when stress components σ_x, σ_θ, $\tau_{\theta x}$, and deflection w are assumed to be given by the shell theory.

3.2.3 Shell Constitutive Equations

The panels in this study are fabricated by laminating plies of a unidirectional fiber-reinforced composite material. It is assumed each ply is homogeneous, linear elastic, and orthotropic with respect to the fiber (1), transverse (2), and through-the-thickness (3) directions. The fiber direction with respect to the positive x-axis in each lamina is given by the angle ϕ shown in Figure 5. Thus, in the shell coordinates x, θ, and z, the material appears to be monoclinic with a plane of symmetry perpendicular to the z-axis. In addition it is assumed that the through-the-thickness stress σ_z is negligible with respect to the in-plane stresses σ_x, σ_θ, and $\tau_{x\theta}$, such that σ_z is set to zero in the constitutive equations. Since the strain ϵ_z also vanishes (see equations (3.10)), the constitutive equation for the z-direction normal stress and strain is neglected. For the in-plane stresses and strains, the lamina constitutive equations are

$$\begin{Bmatrix} \sigma_x \\ \sigma_\theta \\ \tau_{x\theta} \end{Bmatrix} = \begin{bmatrix} \bar{Q}_{11} & \bar{Q}_{12} & \bar{Q}_{16} \\ & \bar{Q}_{22} & \bar{Q}_{26} \\ \text{symm.} & & \bar{Q}_{66} \end{bmatrix} \begin{Bmatrix} \varepsilon_x \\ \varepsilon_\theta \\ \gamma_{x\theta} \end{Bmatrix} , \tag{3.17}$$

in which the elements $\bar{Q}_{11}, \ldots, \bar{Q}_{66}$ are the transformed reduced stiffnesses determined by the elastic moduli E_1, E_2, ν_{12}, and G_{12}, and the angle ϕ. (See Ref. 13, pp. 46-51.) The lamina constitutive equations for the through-the-thickness shear stresses and strains are

$$\begin{Bmatrix} \tau_{\theta z} \\ \tau_{xz} \end{Bmatrix} = \begin{bmatrix} \bar{C}_{44} & \bar{C}_{45} \\ \bar{C}_{45} & \bar{C}_{55} \end{bmatrix} \begin{Bmatrix} \gamma_{\theta z} \\ \gamma_{xz} \end{Bmatrix} , \tag{3.18}$$

where

$$\bar{C}_{44} = \cos^2 \phi \; G_{23} + \sin^2 \phi \; G_{13}$$

$$\bar{C}_{45} = \sin \phi \cos \phi \; (G_{23} - G_{13}) \tag{3.19}$$

$$\bar{C}_{55} = \sin^2 \phi \; G_{23} + \cos^2 \phi \; G_{13},$$

and G_{13} and G_{23} are the shear moduli in the 1-3 and 2-3 planes, respectively.

The shell constitutive equations are obtained by substituting the strains (3.10) into equations (3.17) and (3.18), and then substituting these results into the definitions for the stress resultants (3.13).

Since the panels tested are balanced and symmetric laminates, the shell

constitutive equations for this important class of laminates are

$$
\begin{Bmatrix} N_x \\ N_\theta \\ N_{x\theta} \\ M_x \\ M_\theta \\ M_{x\theta} \end{Bmatrix} = \begin{bmatrix} A_{11} & A_{12} & 0 & 0 & 0 & 0 \\ A_{12} & A_{22} & 0 & 0 & 0 & 0 \\ 0 & 0 & A_{66} & 0 & 0 & 0 \\ 0 & 0 & 0 & D_{11} & D_{12} & D_{16} \\ 0 & 0 & 0 & D_{12} & D_{22} & D_{26} \\ 0 & 0 & 0 & D_{16} & D_{26} & D_{66} \end{bmatrix} \begin{Bmatrix} \varepsilon^o_{xx} \\ \varepsilon^o_{\theta\theta} \\ \gamma^o_{x\theta} \\ \Gamma_{xx} \\ \Gamma_{\theta\theta} \\ \Gamma_{x\theta} \end{Bmatrix} \qquad (3.20)
$$

and

$$
\begin{Bmatrix} Q_\theta \\ Q_x \end{Bmatrix} = \begin{bmatrix} k_1^2 A_{44} & 0 \\ 0 & k_2^2 A_{55} \end{bmatrix} \begin{Bmatrix} \gamma^o_{\theta z} \\ \gamma^o_{xz} \end{Bmatrix} \qquad (3.21)
$$

where the laminate extensional stiffness (A_{ij}) and the laminate bending

stiffness (D_{ij}) are determined from the individual lamina stiffness and

the stacking configuration

$$
(A_{ij}, D_{ij}) = \int_{-h/2}^{h/2} \bar{Q}_{ij}(1, z^2) dz \qquad (i, j = 1, 2, 6)
$$

$$
A_{ij} = \int_{-h/2}^{h/2} \bar{C}_{ij} \, dz \qquad (i, j = 4, 5)
$$

In equation (3.21) k_1^2 and k_2^2 are shear correction factors, which are introduced to account for the nonuniformity of the through-the-thickness shearing stress distribution.

Formulas for the shear correction factors are given by Whitney (Refs. 15 and 16) for laminated anisotropic plates under static loading. For homogeneous isotropic plates various values of the shear correction factors have been used (e.g., 5/6, $\pi^2/12$, and 2/3; see Ref. 17). The shear correction factor serves to change the effective value of the laminate shearing deformation modulus. It is assumed that the shear correction factors are unity in this analysis, since the values of shearing deformation moduli are difficult to measure and are not well known.

3.3 One-Dimensional Shell Equations

The solution of the two-dimensional shell equations is very diffi-cult and requires the use of a numerical computer code. In transport aircraft design the axial lengths of fuselage panels are usually greater than the circumferential arc lengths or widths. A simpler analysis is possible for the central section in long panels if it is assumed that the static response to internal pressure is independent of x. Thus stresses and strains depend only on θ. The solution to the shell equations based on this assumption is developed in this section.

As reported in Reference 1, W. D. Douglas in 1918 argued that the end effects associated with the curved-end boundaries for internally pressurized fabric panels are confined to approximately a half panel

width in the axial direction from each curved edge. On this basis an
analysis which is independent of the axial coordinate x is applicable
for $|x| < L - a\alpha$. The axial length of the central region where a one-
dimensional analysis is applicable is examined in more detail in
Section 4.1.

3.3.1 Shell Equations

Assuming the stress resultants and couples are independent of the
x-coordinate the shell equilibrium equations (3.14) simplify to

$$\frac{1}{a} \frac{dN_{x\theta}}{d\theta} + [\tau_{xz}(t/2) - \tau_{xz}(-t/2)] = 0$$

$$\frac{1}{a} \frac{dN_{\theta}}{d\theta} + [\tau_{\theta z}(t/2) - \tau_{\theta z}(-t/2)] = 0$$

$$N_x \frac{\partial^2 w}{\partial x^2} - \frac{N_\theta}{a} + \frac{1}{a} \frac{\partial}{\partial\theta}\left(\frac{N_\theta}{a} \frac{\partial w}{\partial\theta}\right) + \frac{1}{a} \frac{dQ_\theta}{d\theta}$$

$$+ \frac{1}{a} \frac{\partial}{\partial\theta}\left(N_{x\theta} \frac{\partial w}{\partial x}\right) + \frac{N_{x\theta}}{a} \frac{\partial^2 w}{\partial x \partial\theta} \qquad (3.22)$$

$$+ [\sigma_{zz}(t/2) - \sigma_{zz}(-t/2)] = 0$$

$$\frac{1}{a} \frac{dM_{x\theta}}{d\theta} - Q_x + \frac{t}{2}[\tau_{xz}(t/2) - \tau_{xz}(-t/2)] = 0$$

$$\frac{1}{a} \frac{dM_{\theta}}{d\theta} - Q_\theta + \frac{t}{2}[\tau_{\theta z}(t/2) - \tau_{\theta z}(-t/2)] = 0$$

3.3.2 General Displacement Field

The assumption that the stress resultants and couples are indepen-
dent of the x-coordinate implies the strains and rotation gradients are
independent of the x-coordinate as well, since the two sets of variables
are linearly related by the constitutive equations (3.20) and (3.21).
For this general case, however, the displacements and rotations are not
independent of the x-coordinate. To determine the explicit dependence
of the displacements and rotations on x, the strain-displacement
equations (3.11) and (3.12) are integrated with respect to x under the
restriction that the strains are functions of θ only. Integrating
equations (3.12) gives

$$w^o(x,\theta) = f_3(\theta) - \frac{1}{2} C_1 x^2 + C_2 x\theta + C_3 x$$

$$\Psi_x(x,\theta) = f_4(\theta) + C_1 x \qquad\qquad (3.23)$$

$$\Psi_\theta(x,\theta) = f_5(\theta) - \frac{1}{a} C_2 x,$$

in which C_1, C_2, and C_3 are arbitrary constants, and f_3, f_4, and
f_5 are arbitrary functions of θ. Using the functional form of
$w^o(x,\theta)$ in the first of equations (3.23) in the process of integrating
equations (3.11) gives

$$u^o(x,\theta) = f_1(\theta) + C_1 f_3(\theta)\, x - \frac{1}{6} C_1^2 x^3 + \frac{1}{2} C_1 C_2 x^2 \theta$$

$$- \frac{1}{2} aC_1 \theta^2 x + \frac{1}{2} C_1 C_3 x^2 + (C_4 - C_2 C_3)\, x\theta + \left(C_5 - \frac{1}{2} C_3^2\right) x$$

$$(3.24)$$

$$v^o(x,\theta) = f_2(\theta) - \frac{1}{a} C_2 f_3(\theta)\, x + \frac{1}{6a} C_1 C_2 x^3$$

$$+ \frac{1}{2}\left(C_1 - \frac{1}{a} C_2^2\right) x^2 \theta - \frac{1}{2} C_2 x\theta^2 - \frac{1}{2a} C_4 x^2 - C_3 x\theta + C_6 x,$$

where C_4, C_5, and C_6 are arbitrary constants, and f_1 and f_2 are arbitrary functions of θ.

Using linear elasticity equations Lekhnitskii (Ref. 18) develops general displacement equations for an anisotropic cylindrical body in which stresses are independent of the axial coordinate x. Equivalent u^o and v^o displacements are linear and quadratic in the x-coordinate, respectively. Lekhnitskii's equivalent w^o displacement is quadratic in the x-coordinate. The difference between the displacements derived here and Lekhnitskii's results is due to the use of nonlinear strain-displacement relations and the assumption of a linear displacement variation in the z-coordinate.

3.3.3 Application of Special Boundary Conditions

Special boundary conditions were applied to the general displacement relations (3.23) and (3.24). These conditions were selected because they are needed to model accurately the experimental boundary conditions. They are applied along the circumferential edges of the

panel ($\theta = \alpha$ and $\theta = -\alpha$) and place further restrictions on the displacement functional form. The boundary conditions are

$$u^o(x, \pm\alpha) = \bar{\varepsilon}x$$

$$v^o(x, \pm\alpha) = \mp\bar{v}$$

$$w^o(x, \pm\alpha) = 0 \qquad\qquad (3.25)$$

$$\Psi_x(x, \pm\alpha) = 0$$

$$\Psi_\theta(x, \pm\alpha) = 0$$

where $\bar{\varepsilon}$ and $\bar{v}$ are prescribed data. Application of these boundary conditions reduces the general displacements (3.23) and (3.24) to

$$u^o(x, \theta) = f_1(\theta) + \bar{\varepsilon}x$$

$$v^o(x, \theta) = f_2(\theta)$$

$$w^o(x, \theta) = f_3(\theta) \qquad\qquad (3.26)$$

$$\Psi_x(x, \theta) = f_4(\theta)$$

$$\Psi_\theta(x, \theta) = f_5(\theta),$$

where

$$f_1(\pm\alpha) = 0$$

$$f_2(\pm\alpha) = \mp\bar{v}$$

$$f_3(\pm\alpha) = 0 \qquad\qquad (3.27)$$

$$f_4(\pm\alpha) = 0$$

$$f_5(\pm\alpha) = 0.$$

3.3.4 Reduction of the Field Equations

The one-dimensional shell equations are simplified further for the particular problem of interest. In addition to the boundary conditions (3.25), the applied loading in the experiment is an internal pressure with no surface shear tractions applied to the panel. Hence, for this loading the equilibrium equations (3.22) become

$$\frac{1}{a}\frac{dN_{x\theta}}{d\theta} = 0$$

$$\frac{1}{a}\frac{dN_\theta}{d\theta} = 0$$

$$-\frac{1}{a}N_\theta + \frac{1}{a}\frac{d}{d\theta}\left(N_\theta\frac{1}{a}\frac{dw}{d\theta}\right) + \frac{1}{a}\frac{dQ_\theta}{d\theta} + p = 0 \qquad (3.28)$$

$$\frac{1}{a}\frac{dM_{x\theta}}{d\theta} - Q_x = 0$$

$$\frac{1}{a}\frac{dM_\theta}{d\theta} - Q_\theta = 0.$$

Considering the functional form of the displacements in equations (3.26) the strain-displacement relations in equations (3.11) and (3.12) reduce to

$$\varepsilon^o_{xx} = \bar{\varepsilon}$$

$$\varepsilon^o_{\theta\theta} = \frac{1}{a} \frac{dv^o}{d\theta} + \frac{w^o}{a} + \frac{1}{2} \left(\frac{1}{a} \frac{dw^o}{d\theta} \right)^2$$

$$\gamma^o_{x\theta} = \frac{1}{a} \frac{df_1}{d\theta}$$

$$\gamma^o_{\theta z} = \Psi_\theta + \frac{1}{a} \frac{dw^o}{d\theta}$$

$$\gamma^o_{xz} = \Psi_x \tag{3.29}$$

$$\Gamma_{xx} = 0$$

$$\Gamma_{\theta\theta} = \frac{1}{a} \frac{d\Psi_\theta}{d\theta}$$

$$\Gamma_{x\theta} = \frac{1}{a} \frac{d\Psi_x}{d\theta}$$

From the first equilibrium equation in equations (3.28) $N_{x\theta}$ is spatially constant. The constitutive equation for $N_{x\theta}$ in equations (3.20) then implies the middle surface shear strain $\gamma^o_{x\theta}$ is spatially constant. For a spatially constant middle surface shear

strain, the third equation in (3.29) combined with the boundary conditions on function $f_1(\theta)$ in equations (3.27) requires $f_1(\theta)$ to vanish for all θ. Thus $N_{x\theta} = \gamma_{x\theta}^o = 0$ for all θ. Equations (3.29), with the addition of f_1 equal to zero, imply the constitutive equations (3.20) reduce to

$$N_x = A_{11}\bar{\epsilon} + A_{12}\epsilon_\theta^o$$

$$N_\theta = A_{12}\bar{\epsilon} + A_{22}\epsilon_\theta^o$$

$$M_x = D_{12}\Gamma_{\theta\theta} + D_{16}\Gamma_{x\theta} \qquad (3.30)$$

$$M_\theta = D_{22}\Gamma_{\theta\theta} + D_{26}\Gamma_{x\theta}$$

$$M_{x\theta} = D_{26}\Gamma_{\theta\theta} + D_{66}\Gamma_{x\theta}.$$

The constitutive equations (3.21) for the shearing deformation resultants remain unchanged, and are repeated below for convenience with shear correction factors k_1^2 and k_2^2 assumed to be unity.

$$Q_\theta = A_{44}\gamma_{\theta z}^o$$

$$\qquad (3.31)$$

$$Q_x = A_{55}\gamma_{xz}^o$$

Using the equilibrium equations (3.28), with $N_{x\theta} = 0$ for all θ, in combination with the strain-displacement equations (3.29) and

constitutive equations (3.30) and (3.31), the mathematical formulation reduces to

$$\frac{dN_\theta}{d\theta} = 0 \tag{3.32}$$

$$\frac{N_\theta}{a^2} \frac{d^2 w^o}{d\theta^2} + \frac{A_{44}}{a} \frac{d}{d\theta} \left(\Psi_\theta + \frac{1}{a} \frac{dw^o}{d\theta} \right) = -p + \frac{N_\theta}{a} \tag{3.33}$$

$$\frac{D_{22}}{a^2} \frac{d^2 \Psi_\theta}{d\theta^2} + \frac{D_{26}}{a^2} \frac{d^2 \Psi_x}{d\theta^2} - A_{44} \left(\Psi_\theta + \frac{1}{a} \frac{dw^o}{d\theta} \right) = 0 \tag{3.34}$$

$$\frac{D_{26}}{a^2} \frac{d^2 \Psi_\theta}{d\theta^2} + \frac{D_{66}}{a^2} \frac{d^2 \Psi_x}{d\theta^2} - A_{55} \Psi_x = 0 \tag{3.35}$$

$$N_\theta = A_{12} \bar{\epsilon} + A_{22} \left[\frac{1}{a} \frac{dv^o}{d\theta} + \frac{w^o}{a} + \frac{1}{2} \left(\frac{1}{a} \frac{dw^o}{d\theta} \right)^2 \right] . \tag{3.36}$$

Equations (3.32) to (3.36) constitute an eighth order system of ordinary differential equations for the dependent variables N_θ, w^o, Ψ_θ, Ψ_x, and v^o, with p and $\bar{\epsilon}$ as prescribed loads. They are to be solved subject to the eight boundary conditions

$$v^o(\pm\alpha) = \mp\bar{v} \tag{3.37}$$

$$w^o(\pm\alpha) = 0 \tag{3.38}$$

$$\Psi_\theta(\pm\alpha) = 0 \tag{3.39}$$

$$\Psi_x(\pm a) = 0, \tag{3.40}$$

which are obtained from equations (3.26) and (3.27) where $\bar{v}$ is a prescribed displacement.

3.3.5 Method of Solution

Equations (3.32) to (3.36), subject to boundary conditions (3.37) to (3.40), are a nonlinear two-point boundary value problem. The circumferential stress resultant N_θ is spatially constant as the equilibrium equation (3.32) indicates. Since N_θ is spatially constant, equations (3.33) to (3.35) appear to be linear in w^0, Ψ_θ, and Ψ_x. However, N_θ depends nonlinearly on w^0 as shown in equation (3.36). This structure of the boundary value problem permits the following solution procedure. Using the methods of solution for linear ordinary differential equations with constant coefficients, equations (3.33) to (3.35) are solved for $w^0(\theta)$, $\Psi_\theta(\theta)$, and $\Psi_x(\theta)$, subject to boundary conditions (3.38) to (3.40). These solutions will depend on the "coefficient" N_θ. The solution for $w^0(\theta)$ is then substituted into equation (3.36) and indefinite integration on θ is performed using the fact that N_θ is spatially constant. The unknown constant of integration and the unknown value of N_θ are determined by boundary conditions on v^0 in equation (3.37).

By neglecting the bending terms (these have coefficients D_{22}, D_{66}, and D_{26}) equations (3.32) through (3.36) obtained apply to the

corresponding membrane shell. Subject to boundary conditions (3.38), the membrane solution is

$$w_p^o(\theta) = \frac{a}{2} \left(\frac{pa - N_\theta}{N_\theta} \right) \left(\alpha^2 - \theta^2 \right) \tag{3.41}$$

$$\Psi_{\theta p}(\theta) = - \left(\frac{pa - N_\theta}{N_\theta} \right) \theta \tag{3.42}$$

$$\Psi_{xp}(\theta) = 0. \tag{3.43}$$

Notice that in the nonlinear membrane theory it is possible to satisfy boundary conditions on the deflection $w^o(\theta)$. In linear membrane shell theory the boundary conditions on the deflection cannot be satisfied in general. The fact that nonlinear membrane theory can satisfy physically reasonable boundary conditions whereas linear membrane theory cannot, was pointed out by Bromberg and Stoker (Ref. 19).

A homogeneous solution of equations (3.33) through (3.35) has the form

$$\begin{Bmatrix} w^o \\ \Psi_\theta \\ \Psi_x \end{Bmatrix}_h = \begin{Bmatrix} X \\ Y \\ Z \end{Bmatrix} e^{\lambda\theta} , \tag{3.44}$$

which, when substituted into equations (3.33) through (3.35), leads to

$$
\begin{bmatrix}
(N_\theta + A_{44})\bar{\lambda}^2 & A_{44}\,\bar{\lambda} & 0 \\
-A_{44}\,\bar{\lambda} & D_{22}\,\bar{\lambda}^2 - A_{44} & D_{26}\,\bar{\lambda}^2 \\
0 & D_{26}\,\bar{\lambda}^2 & D_{66}\,\bar{\lambda}^2 - A_{55}
\end{bmatrix}
\begin{Bmatrix} X \\ Y \\ Z \end{Bmatrix} e^{\lambda\theta} =
\begin{Bmatrix} 0 \\ 0 \\ 0 \end{Bmatrix}
\tag{3.45}
$$

where $\bar{\lambda} = \dfrac{\lambda}{a}$. Nontrivial solutions of equation (3.45) require the determinant of coefficients to vanish, which results in the character-istic equation

$$
\bar{\lambda}^2 \left[(1 - \epsilon^2)\,\bar{\lambda}^4 - (b^2 + c^2)\,\bar{\lambda}^2 + c^2 b^2 \right] = 0,
\tag{3.46}
$$

where by definition

$$
\epsilon^2 = \frac{D_{26}^2}{(D_{22} D_{66})}
$$

$$
b^2 = \frac{N_\theta}{D_{22}} \frac{A_{44}}{A_{44} + N_\theta}
\tag{3.47}
$$

$$
c^2 = \frac{A_{55}}{D_{66}}.
$$

The roots of the characteristic equation are 0, 0, $\pm\bar{\lambda}_1$, and $\pm\bar{\lambda}_2$, where

$$\bar{\lambda}_{1,2}^2 = \frac{b^2 + c^2 \pm \sqrt{\left(b^2 - c^2\right)^2 + 4\epsilon^2 b^2 c^2}}{2(1 - \epsilon^2)}. \tag{3.48}$$

The four nonzero roots given by equation (3.48) are associated with bending boundary layers at $\theta = \pm\alpha$, which decay exponentially from the edges towards the center of the panel. Approximate expressions for the roots may be obtained by performing an asymptotic expansion in the small parameter ϵ which is less than unity for the materials examined. These approximate expressions reveal more about the nature of the roots and are given as follows

$$\begin{aligned}
\bar{\lambda}_1^2 &= b^2 + \epsilon^2 \left(b^2 + \frac{c^2}{b^2 - c^2} \right) + O(\epsilon^4) \\[2ex]
\bar{\lambda}_2^2 &= c^2 + \epsilon^2 \left(c^2 - \frac{c^2}{b^2 - c^2} \right) + O(\epsilon^4)
\end{aligned} \tag{3.49}$$

The parameter ϵ is zero for specially orthotropic laminates ($D_{26} = 0$) and the roots $\bar{\lambda}_1$ and $\bar{\lambda}_2$ uncouple. For small ϵ the root $\bar{\lambda}_1$ is associated with the rotation Ψ_θ (circumferential shear and bending), and the root $\bar{\lambda}_2$ is associated with the rotation Ψ_x (axial shear and the twisting moment). For the laminates and pressures considered here the root $\bar{\lambda}_2$ is an order of magnitude larger than the root $\bar{\lambda}_1$. Thus, the twist-curvature bending boundary layer effects decay at a much faster rate from the clamped edges than the circumferential bending boundary layer effects.

The complete homogeneous solution is

$$
\left\{ \begin{matrix} w^o \\ \Psi_\theta \\ \Psi_x \end{matrix} \right\}_h = \left\{ \begin{matrix} c_1 \\ -c_2/a \\ 0 \end{matrix} \right\} + c_2 \left\{ \begin{matrix} 1 \\ 0 \\ 0 \end{matrix} \right\} \theta + c_3 \left\{ \begin{matrix} 1 \\ \xi_{21} \\ \xi_{31} \end{matrix} \right\} e^{\lambda_1 \theta} + c_4 \left\{ \begin{matrix} 1 \\ -\xi_{21} \\ -\xi_{31} \end{matrix} \right\} e^{-\lambda_1 \theta}
$$

$$
+ c_5 \left\{ \begin{matrix} 1 \\ \xi_{22} \\ \xi_{32} \end{matrix} \right\} e^{\lambda_2 \theta} + c_6 \left\{ \begin{matrix} 1 \\ -\xi_{22} \\ -\xi_{32} \end{matrix} \right\} e^{-\lambda_2 \theta}, \tag{3.50}
$$

where c_1, c_2, ..., c_6 are arbitrary constants, and the eigenvectors are the solution of

$$
\begin{bmatrix} D_{22}\bar{\lambda}_i^2 - A_{44} & D_{26}\bar{\lambda}_i^2 \\ D_{26}\bar{\lambda}_i^2 & D_{66}\bar{\lambda}_i^2 - A_{55} \end{bmatrix} \left\{ \begin{matrix} \xi_{2i} \\ \xi_{3i} \end{matrix} \right\} = \left\{ \begin{matrix} A_{44}\bar{\lambda}_i \\ 0 \end{matrix} \right\} \quad i = 1,2. \tag{3.51}
$$

The principle of superposition does not hold for equations (3.32) to (3.36) because the equations are nonlinear. However the total solution for w^o, Ψ_θ, and Ψ_x may be obtained by adding the membrane solution (3.41-3.43) and the homogeneous solution (3.50) where the constant N_θ which occurs in both solutions has not been specified yet. The solution is exact once N_θ and v^o are determined from equations (3.36) and (3.37). The six constants for the total solution are determined from the six boundary conditions given by equations (3.38) to (3.40). Writing the exponential functions in terms of hyperbolic functions, the solution subject to the boundary condition is

$$w^o(\theta) = \left(\frac{pa - N_\theta}{N_\theta}\right)\left(\frac{\bar{\lambda}_1^{-2}\ \bar{\lambda}_2^{-2}}{\bar{\lambda}_1^{-2} - \bar{\lambda}_2^{-2}}\right)\alpha\left(\frac{D_{26}^2 - D_{22}D_{66}}{A_{44}\ A_{55}}\ \bar{\lambda}_1 + \frac{D_{22}A_{55} + D_{66}A_{44}}{A_{44}A_{55}}\ \frac{1}{\bar{\lambda}_1}\right.$$

$$\left.- \frac{1}{\bar{\lambda}_1^{3}}\right)\frac{\cosh \lambda_1\theta - \cosh \lambda_1\alpha}{\sinh \lambda_1\alpha} \tag{3.52}$$

$$- \left(\frac{pa - N_\theta}{N_\theta}\right)\left(\frac{\bar{\lambda}_1^{-2}\ \bar{\lambda}_2^{-2}}{\bar{\lambda}_1^{-2} - \bar{\lambda}_2^{-2}}\right)\alpha\left(\frac{D_{26}^2 - D_{22}D_{66}}{A_{44}A_{55}}\ \bar{\lambda}_2 + \frac{D_{22}A_{55} + D_{66}A_{44}}{A_{44}A_{55}}\ \frac{1}{\bar{\lambda}_2}\right.$$

$$\left.- \frac{1}{\bar{\lambda}_2^{3}}\right)\frac{\cosh \lambda_2\theta - \cosh \lambda_2\alpha}{\sinh \lambda_2\alpha} - a\left(\frac{pa - N_\theta}{N_\theta}\right)\left(\frac{\theta^2}{2} - \frac{\alpha^2}{2}\right)$$

$$\Psi_\theta(\theta) = \left(\frac{pa - N_\theta}{N_\theta}\right)\left(\frac{\bar{\lambda}_1^{-2}\ \bar{\lambda}_2^{-2}}{\bar{\lambda}_1^{-2} - \bar{\lambda}_2^{-2}}\right)\alpha\ \frac{D_{66}}{A_{55}}\left[\frac{\left(\frac{A_{55}}{D_{66}} - \bar{\lambda}_1^{2}\right)}{\bar{\lambda}_1^{2}}\ \frac{\sinh \lambda_1\theta}{\sinh \lambda_1\alpha}\right.$$

$$\left.- \frac{\left(\frac{A_{55}}{D_{66}} - \bar{\lambda}_2^{2}\right)}{\bar{\lambda}_2^{2}}\ \frac{\sinh \lambda_2\theta}{\sinh \lambda_2\alpha}\right] + \left(\frac{pa - N_\theta}{N_\theta}\right)\theta \tag{3.53}$$

$$\Psi_x(\theta) = \left(\frac{pa - N_\theta}{N_\theta}\right)\left(\frac{\bar{\lambda}_1^{-2}\ \bar{\lambda}_2^{-2}}{\bar{\lambda}_1^{-2} - \bar{\lambda}_2^{-2}}\right)\alpha\ \frac{D_{26}}{A_{55}}\left[\frac{\sinh \lambda_1\theta}{\sinh \lambda_1\alpha} - \frac{\sinh \lambda_2\theta}{\sinh \lambda_2\alpha}\right] \tag{3.54}$$

The dependent variables w^o, Ψ_θ, and Ψ_x were not evaluated numerically using the functional forms shown in equations (3.52) to (3.54). For large values of λ_1 and λ_2 the hyperbolic functions exceeded the maximum magnitudes permitted on CDC 170 series machines at NASA Langley. Since the hyperbolic functions occur in the numerator and

denominator of the terms in equations (3.52) to (3.54), it is possible to rewrite the devision of two large numbers in a more numerically efficient manner. To accomplish this, the hyperbolic functions are written in exponential form and then manipulated to make the denominator approximately equal to one. A typical example of this procedure is shown below.

$$\frac{\cosh \lambda_1 \theta}{\sinh \lambda_1 \alpha} = \frac{e^{\lambda_1 \theta} + e^{-\lambda_1 \theta}}{e^{\lambda_1 \alpha} - e^{-\lambda_1 \alpha}} \cdot \frac{e^{-\lambda_1 \alpha}}{e^{-\lambda_1 \alpha}} = \frac{e^{\lambda_1(\theta-\alpha)} + e^{-\lambda_1(\theta+\alpha)}}{1 - e^{-2\lambda_1 \alpha}}$$

(3.55)

$$\frac{\cosh \lambda_1 \theta}{\sinh \lambda_1 \alpha} \approx e^{\lambda_1(\theta-\alpha)} + e^{-\lambda_1(\theta+\alpha)}$$

Near the edge $\theta = \alpha$ the second term in equation (3.55) is negligible with respect to the first such that

$$\frac{\cosh \lambda_1 \theta}{\sinh \lambda_1 \alpha} \approx e^{\lambda_1(\theta-\alpha)},$$

(3.56)

and near the edge $\theta = -\alpha$ the first term is negligible with respect to the second term such that

$$\frac{\cosh \lambda_1 \theta}{\sinh \lambda_1 \alpha} \approx e^{-\lambda_1(\theta+\alpha)}.$$

(3.57)

Let $\phi = \theta + \alpha$ so that at the edge $\theta = -\alpha$, $\phi = 0$, and ϕ increases toward the center of the shell. In terms of the coordinate ϕ, equations (3.52) to (3.54) are approximated by

$$w^o(\phi) \approx \left(\frac{pa - N_\theta}{N_\theta}\right)\left(\frac{\bar\lambda_1^2 \bar\lambda_2^2}{\bar\lambda_1^2 - \bar\lambda_2^2}\right)\alpha\left[\frac{D_{26}^2 - D_{22}D_{66}}{A_{44}A_{55}}\bar\lambda_1 + \frac{D_{22}A_{55} + D_{66}A_{44}}{A_{44}A_{55}}\frac{1}{\bar\lambda_1}\right.$$

$$\left. - \frac{1}{\bar\lambda_1^3}\right]\left(e^{-\lambda_1\phi} - 1\right) - \left(\frac{pa - N_\theta}{N_\theta}\right)\left(\frac{\bar\lambda_1^2 \bar\lambda_2^2}{\bar\lambda_1^2 - \bar\lambda_2^2}\right)\alpha\left[\frac{D_{26}^2 - D_{22}D_{66}}{A_{44}A_{55}}\bar\lambda_2\right.$$

$$\left. + \frac{D_{22}A_{55} + D_{66}A_{44}}{A_{44}A_{55}}\frac{1}{\bar\lambda_2} - \frac{1}{\bar\lambda_2^3}\right]\left(e^{-\lambda_1\phi} - 1\right) - a\left(\frac{pa - N_\theta}{N_\theta}\right)\left(\frac{\phi^2}{2} - \phi\alpha\right)$$

$$(3.58)$$

$$\Psi_\theta(\phi) \approx \left(\frac{pa - N_\theta}{N_\theta}\right)\left(\frac{\bar\lambda_1^2 \bar\lambda_2^2}{\bar\lambda_1^2 - \bar\lambda_2^2}\right)\alpha\frac{D_{66}}{A_{55}}\left[\frac{\left(\frac{A_{55}}{D_{66}} - \bar\lambda_2^2\right)}{\bar\lambda_2^2}e^{-\lambda_2\phi} - \frac{\left(\frac{A_{55}}{D_{66}} - \bar\lambda_1^2\right)}{\bar\lambda_1^2}e^{-\lambda_1\phi}\right]$$

$$+ \left(\frac{pa - N_\theta}{N_\theta}\right)(\phi - \alpha) \qquad (3.59)$$

$$\Psi_x(\phi) \approx \left(\frac{pa - N_\theta}{N_\theta}\right)\left(\frac{\bar\lambda_1^2 \bar\lambda_2^2}{\bar\lambda_1^2 - \bar\lambda_2^2}\right)\alpha\frac{D_{26}}{A_{55}}\left[e^{-\lambda_2\phi} - e^{-\lambda_1\phi}\right] \qquad (3.60)$$

The circumferential resultant N_θ is an unknown constant at this point. The value of it and the circumferential displacement $v^o(\theta)$ are determined by substituting $w^o(\theta)$ given by equation (3.52) into equation (3.36), integrating on θ, and applying the two boundary conditions

given by equation (3.37). The result of this procedure for N_θ as a function of the internal pressure parameter R is the equation

$$A(N_\theta) \, R^2 + B(N_\theta) \, R + C(N_\theta) = 0 \tag{3.61}$$

in which

$$R = \frac{pa - N_\theta}{N_\theta} \tag{3.62}$$

$$A = -\frac{\bar{K}_1^2}{4} \left(\frac{1}{\lambda_1 \tanh \lambda_1 \alpha} - \frac{\alpha}{\sinh^2 \lambda_1 \alpha} \right)$$

$$- \frac{\bar{K}_2^2}{4} \left(\frac{1}{\lambda_2 \tanh \lambda_2 \alpha} - \frac{\alpha}{\sinh^2 \lambda_2 \alpha} \right)$$

$$- \frac{\bar{K}_1 \, \bar{K}_2}{\lambda_1^2 - \lambda_2^2} \left(\frac{\lambda_1}{\tanh \lambda_1 \alpha} - \frac{\lambda_2}{\tanh \lambda_2 \alpha} \right)$$

$$+ \frac{\bar{K}_1}{\lambda_1^2} \left(\frac{\lambda_1 \alpha}{\tanh \lambda_1 \alpha} - 1 \right) + \frac{\bar{K}_2}{\lambda_2^2} \left(\frac{\lambda_2 \alpha}{\tanh \lambda_2 \alpha} - 1 \right) - \frac{\alpha^3}{6} \tag{3.63}$$

$$B = \frac{\bar{K}_1}{\lambda_1} \left(\frac{\alpha}{\tanh \lambda_1 \alpha} - \frac{1}{\lambda_1} \right) + \frac{\bar{K}_2}{\lambda_2} \left(\frac{\alpha}{\tanh \lambda_2 \alpha} - \frac{1}{\lambda_2} \right) - \frac{\alpha^3}{3} \tag{3.64}$$

$$C = \frac{\left(N_\theta - A_{12} \bar{\epsilon} \right) \alpha}{A_{22}} + \frac{\bar{v}}{a} \tag{3.65}$$

and

$$\bar{K}_1 = \left(\frac{\bar{\lambda}_1^{-2} \bar{\lambda}_2^{-2}}{\bar{\lambda}_1^2 - \bar{\lambda}_2^2}\right)\left(\frac{D_{26}^2 - D_{22}D_{66}}{A_{44}A_{55}} \bar{\lambda}_1^{-2} + \frac{A_{55}D_{22} + A_{44}D_{66}}{A_{44}A_{55}} - \frac{1}{\bar{\lambda}_1^2}\right)\alpha \qquad (3.66)$$

$$\bar{K}_2 = -\left(\frac{\bar{\lambda}_1^2 \bar{\lambda}_2^2}{\bar{\lambda}_1^2 - \bar{\lambda}_2^2}\right)\left(\frac{D_{26}^2 - D_{22}D_{66}}{A_{44}A_{55}} \bar{\lambda}_2^{-2} + \frac{A_{55}D_{22} + A_{44}D_{66}}{A_{44}A_{55}} - \frac{1}{\bar{\lambda}_2^2}\right)\alpha \qquad (3.67)$$

Solutions to equation (3.61) are readily obtained by assuming a value of N_θ and solving for R, and hence p, as the roots of the resulting quadratic equation. In the cases examined in this study the pressure associated with one root of equation (3.61) was positive and the pressure associated with the second root was negative. The negative pressure solution to equation (3.61) was disregarded since it is not consistent with an internally pressurized shell. These solutions relating the pressure p to the circumferential stress resultant N_θ are then used to determine the other unknowns of this nonlinear shell response problem.

The exponential terms in equations (3.58) to (3.60) decay away from the boundary ($\phi = 0$) because of their negative exponents. A boundary decay length may be defined as the distance from the boundary for an exponential term to decay to a small value ϵ. After selecting a value for ϵ a boundary decay length (ξ) may be determined

$$e^{-\bar{\lambda}a\phi} = \epsilon$$

or

$$\xi = a\phi = \frac{1}{\bar{\lambda}} \ln\left(\frac{1}{\epsilon}\right) \qquad (3.68)$$

where

$$\bar{\lambda} = \frac{\lambda}{a}.$$

A typical value for ϵ might be 0.01 and two values of λ are given by equation (3.48). Therefore, two boundary decay lengths are evident in the dependent variables given by equations (3.58) to (3.60). One decay length is associated with twist-curvature effects (λ_1) and the other with circumferential bending effects (λ_2).

3.3.6 Kirchhoff-Love Approximation

In this section additional kinematic restrictions will be placed on the panel displacement fields. Normals to the undeformed surface will be assumed to remain normal to the deformed surface. This assumption means the shearing deformation strains $\gamma_{\theta z}^{o}$ and γ_{xz}^{o} vanish, which imply the rotations in equation (3.12) become

$$\Psi_x = -\frac{dw^o}{dx} \qquad (3.69)$$

$$\Psi_\theta = -\frac{1}{a}\frac{dw^o}{d\theta}. \qquad (3.70)$$

Thus the displacement fields in equation (3.9) have the following form
for the one-dimensional analysis

$$u(x,\theta,z) = \bar{\varepsilon}x \qquad (3.71)$$

$$v(x,\theta,z) = v^o(\theta) - z\,\frac{1}{a}\,\frac{dw^o}{d\theta}(\theta) \qquad (3.72)$$

$$w(x,\theta,z) = w^o(\theta) \qquad (3.73)$$

With the above restrictions a mathematical formulation equivalent to
equations (3.32) to (3.36) becomes

$$\frac{dN_\theta}{d\theta} = 0 \qquad (3.74)$$

$$\frac{D_{22}}{a^4}\,\frac{d^4w^o}{d\theta^4} - \frac{N_\theta}{a^2}\,\frac{d^2w^o}{d\theta^2} = p - \frac{N_\theta}{a} \qquad (3.75)$$

$$N_\theta = A_{12}\bar{\varepsilon} + A_{22}\left[\frac{1}{a}\,\frac{dv^o}{d\theta} + \frac{w^o}{a} + \frac{1}{2}\left(\frac{1}{a}\,\frac{dw^o}{d\theta}\right)^2\right] \qquad (3.76)$$

Equations (3.74) to (3.76) constitute a sixth order system of ordinary
differential equations for the dependent variables N_θ, w^o, and v^o,
with p and $\bar{\varepsilon}$ as prescribed loads. They are solved subject to the
six boundary conditions

$$v^o(\pm\alpha) = \mp\bar{v} \qquad (3.77)$$

$$w^o(\pm\alpha) = 0 \qquad (3.78)$$

$$\frac{1}{a} \frac{dw^o}{d\theta} (\pm \alpha) = 0 \qquad (3.79)$$

Equations (3.74) to (3.76), subject to boundary conditions (3.77) to (3.79), are solved by the same method of solution described in Section 3.3.5. The results of the solution are

$$w^o(\theta) = \frac{a}{2} \left(\frac{pa - N_\theta}{N_\theta} \right) (\alpha^2 - \theta^2) + \left(\frac{pa - N_\theta}{N_\theta} \right) \frac{a\alpha}{\lambda} \frac{(\cosh \lambda\theta - \cosh \lambda\alpha)}{\sinh \lambda\theta} \qquad (3.80)$$

where

$$\lambda = a \sqrt{N_\theta / D_{22}}, \qquad (3.81)$$

and N_θ and the pressure are related by

$$A(N_\theta) R^2 + B(N_\theta) R + C(N_\theta) = 0 \qquad (3.82)$$

in which

$$R = \frac{pa - N_\theta}{N_\theta}$$

$$A = \frac{\alpha^3}{6} + \frac{\alpha}{\lambda^2} \left(1 - \frac{\lambda\alpha}{\tanh \lambda\alpha} \right) + \frac{1}{4} \frac{\alpha^2}{\tanh \lambda\alpha} - \frac{1}{4} \frac{\alpha^3}{\sinh^2 \lambda\alpha}$$

$$(3.83)$$

$$B = - \frac{\alpha^3}{3} + \frac{\alpha}{\lambda^2} \left(1 - \frac{\lambda\alpha}{\tanh \lambda\alpha} \right)$$

$$C = \frac{\left(N_\theta - A_{12} \bar{\epsilon} \right)}{A_{22}} + \frac{\bar{v}}{a}$$

The parameter λ in equation (3.81) is the magnitude of the nonzero roots ($\pm\lambda$) of the characteristic equation for the homogeneous solution to $w^o(\theta)$, and represents the rate of exponential decay of the bending boundary layer. The root λ of equation (3.81) is equivalent to the root λ_1 of equation (3.48) which is associated with circumferential shear and bending in the shear deformation theory. For the Kirchhoff-Love approximation there is no root equivalent to $\bar{\lambda}_2$ of equation (3.48). A boundary decay length associated with circumferential bending may be calculated by substituting λ from equation (3.81) into the definition given by equation (3.68).

For geometrically linear strain-displacement relations equations (3.74) to (3.76) of the Kirchhoff-Love theory become

$$\frac{dN_\theta}{d\theta} = 0 \tag{3.84}$$

$$\frac{D_{22}}{a^4} \frac{d^4 w^o}{d\theta^4} = p - \frac{N_\theta}{a} \tag{3.85}$$

$$N_\theta = A_{12}\bar{\epsilon} + A_{22}\left[\frac{1}{a} \frac{dv^o}{d\theta} + \frac{w^o}{a}\right] \tag{3.86}$$

These linear equations are a sixth order system of ordinary differential equations and are solved subject to the six boundary conditions given by equations (3.77) to (3.79). Equation (3.85) may be easily integrated and the solution derived is equivalent to that determined from beam

theory when the right hand side of equation (3.85) is equated to an
effective pressure p_1

$$p_1 = p - \frac{N_\theta}{a} \tag{3.87}$$

After integration of equation (3.85) and application of boundary condi-
tions in equations (3.78) and (3.79), the solution for w^0 is

$$w^0(\theta) = \frac{a^4}{24D_{22}} \, p_1 \left(\theta^2 - \alpha^2\right)^2 \tag{3.88}$$

The circumferential stress resultant N_θ is still an unknown in equa-
tion (3.88). The resultant N_θ may be found by integrating equa-
tion (3.86) subject to boundary conditions in equation (3.77) and using
the fact that N_θ is a constant from equation (3.84). The result of
this operation is the following expression for N_θ

$$N_\theta = \frac{A_{12}\bar{\epsilon} - A_{22}\left(\dfrac{\bar{v}}{a\alpha}\right) + \dfrac{A_{22}}{45D_{22}} a^2 \alpha^4 pa}{1 + \dfrac{A_{22}}{45D_{22}} a^2 \alpha^4} \tag{3.89}$$

The linear Kirchhoff-Love solution for w^0 in equation (3.88) does not
exhibit a bending boundary layer as does the nonlinear Kirchhoff-Love
solution given by equation (3.80) and the nonlinear shearing deformation
solution given by equations (3.58) to (3.60). The linear and nonlinear
Kirchhoff-Love approximations are compared in Section 4.3.

3.4 Through-The-Thickness Stresses

The transverse stresses $(\tau_{\theta z}, \tau_{xz}, \sigma_{zz})$ are calculated from the elasticity equilibrium equations (3.7) with the assumptions, consistent with the one-dimensional shell analysis, that all stresses are assumed to be independent of the x-coordinate and the displacement w is independent of x as given by equations (3.26). With these assumptions equations (3.7) reduce to

$$\frac{1}{a} \frac{\partial \tau_{x\theta}}{\partial \theta} + \frac{\partial \tau_{xz}}{\partial z} = 0 \tag{3.90}$$

$$\frac{1}{a} \frac{\partial \sigma_{\theta\theta}}{\partial \theta} + \frac{\partial \tau_{\theta z}}{\partial z} = 0 \tag{3.91}$$

$$\frac{1}{a} \frac{\partial \tau_{\theta z}}{\partial \theta} + \frac{\partial \sigma_{zz}}{\partial z} - \frac{\sigma_{\theta\theta}}{a} + \frac{1}{a} \frac{\partial}{\partial \theta}\left(\frac{\sigma_{\theta\theta}}{a} \frac{\partial w}{\partial \theta}\right) = 0. \tag{3.92}$$

Explicit expressions for the stress components σ_x, σ_θ, and $\tau_{x\theta}$ in the thickness coordinate follow from equations (3.10), (3.17), and (3.29), combined with $\gamma^0_{x\theta} = 0$. Although σ_x is not needed to determine the transverse stresses in the elasticity equilibrium equations, it is given below since it is needed in subsequent failure analyses. The inplane stress components within a typical lamina are

$$\sigma_x = \bar{Q}_{11}\bar{\epsilon} + \bar{Q}_{12}\epsilon^o_\theta + z\left[\bar{Q}_{12}\Gamma_{\theta\theta} + \bar{Q}_{16}\Gamma_{x\theta}\right] \tag{3.93}$$

$$\sigma_\theta = \bar{Q}_{12}\bar{\epsilon} + \bar{Q}_{22}\epsilon^o_\theta + z\left[\bar{Q}_{22}\Gamma_{\theta\theta} + \bar{Q}_{26}\Gamma_{x\theta}\right] \tag{3.94}$$

$$\tau_{x\theta} = \bar{Q}_{16}\bar{\varepsilon} + \bar{Q}_{26}\varepsilon_{\theta}^{o} + z\left[\bar{Q}_{26}\Gamma_{\theta\theta} + \bar{Q}_{66}\Gamma_{x\theta}\right]. \tag{3.95}$$

The transverse shear stress τ_{xz} is determined by substituting $\tau_{x\theta}$ from equation (3.95) into the equilibrium equation (3.90) and integrating in the z-direction. Similarly the transverse shear stress $\tau_{\theta z}$ is obtained by substituting σ_{θ} from equation (3.94) into the second equilibrium equation (3.91) and integrating on z. The constants of integration resulting from these indefinite integrations are determined by requiring the transverse shear stresses to vanish at $z = -t/2$ which is consistent with boundary conditions (3.8). Finally, the expressions for the transverse shear stress $\tau_{\theta z}$, the circumferential stress σ_{θ} in equation (3.94), and the deflection $w^{o}(\theta)$ in equation (3.52) are substituted into the third equilibrium equation (3.92) and indefinite integration on z is performed to determine σ_z. The constant of integration is determined by setting $\sigma_z = -p$ at $z = -t/2$. In the integration processes described it is important to recognize that the transformed reduced stiffnesses are piecewise constant functions of z. The results of this lengthy process are

$$\tau_{zx}^{(k)}(\theta,z) = -\frac{1}{a}\frac{d\Gamma_{\theta}}{d\theta}(\theta)\, q_{226}(z) - \frac{1}{a}\frac{d\Gamma_{x\theta}}{d\theta}(\theta)\, q_{266}(z) \tag{3.96}$$

$$\tau_{z\theta}^{(k)}(\theta,z) = -\frac{1}{a}\frac{d\Gamma_{\theta}}{d\theta}(\theta)\, q_{222}(z) - \frac{1}{a}\frac{d\Gamma_{x\theta}}{d\theta}(\theta)\, q_{226}(z) \tag{3.97}$$

$$\sigma_z^{(k)}(\theta, z) = -p + \frac{\bar{\varepsilon}}{a}\left(1 - \frac{1}{a}\frac{d^2 w(\theta)}{d\theta^2}\right) q_{112}(z) + \frac{\varepsilon_\theta^o}{a}\left(1 - \frac{1}{a}\frac{d^2 w(\theta)}{d\theta^2}\right) q_{122}(z)$$

$$+ \left[\frac{\Gamma_\theta(\theta)}{a}\left(1 - \frac{1}{a}\frac{d^2 w(\theta)}{d\theta^2}\right) - \frac{1}{a^2}\frac{d\Gamma_\theta(\theta)}{d\theta}\frac{dw(\theta)}{d\theta}\right] q_{222}(z)$$

$$+ \left[\frac{\Gamma_{x\theta}(\theta)}{a}\left(1 - \frac{1}{a}\frac{d^2 w(\theta)}{d\theta^2}\right) - \frac{1}{a^2}\frac{d\Gamma_{x\theta}(\theta)}{d\theta}\frac{dw(\theta)}{d\theta}\right] q_{226}(z)$$

$$+ \frac{1}{a^2}\frac{d^2\Gamma_\theta(\theta)}{d\theta^2} q_{322}(z) + \frac{1}{a^2}\frac{d^2\Gamma_{x\theta}}{d\theta^2}(\theta) \, q_{326}(z), \qquad (3.98)$$

where

$$q_{1mn}(z) = \sum_{i=1}^{k-1} \bar{Q}_{mn}^{(i)}(z_i - z_{i-1}) + \bar{Q}_{mn}^{(k)}(z - z_{k-1}) \qquad (3.99)$$

$$q_{2mn}(z) = \sum_{i=1}^{k-1} \bar{Q}_{mn}^{(i)} \frac{\left(z_i^2 - z_{i-1}^2\right)}{2} + \bar{Q}_{mn}^{(k)} \frac{\left(z^2 - z_{k-1}^2\right)}{2} \qquad (3.100)$$

$$q_{3mn}(z) = \sum_{i=1}^{k-1} \frac{\bar{Q}_{mn}^{(i)}}{2}\left[\frac{z_i^3 - z_{i-1}^3}{3} - z_{i-1}^2(z_i - z_{i-1}) + (z_i^2 - z_{i-1}^2)(z - z_i)\right]$$

$$+ \frac{\bar{Q}_{mn}^{(k)}}{2}\left[\frac{z^3 - z_{k-1}^3}{3} - z_{k-1}^2(z - z_{k-1})\right] \qquad (3.101)$$

In equations (3.99) to (3.101), z_i designates the thickness coordinate
to the top of the ith layer in the laminate; i.e., $z_i = (i - N/2)\, h$,

$i = 1, 2, \ldots, N$, where h is the layer thickness, and N is the number of layers in the laminate ($t = Nh$). If z is set equal to $t/2$ in equations (3.99) to (3.101), then $q_{1mn}(t/2) = A_{mn}$, $q_{2mn}(t/2) = B_{mn} = 0$, and $q_{3mn}(t/2) = D_{mn}$, in which A_{mn}, B_{mn}, and D_{mn} are the extension, coupling, and bending stiffnesses, respectively, of classical lamination theory. The stresses τ_{xz}, $\tau_{\theta z}$, and σ_z given by equations (3.96) to (3.98) vanish at the upper surface, as they should, because the shell equilibrium equations are integrated versions of the elasticity equilibrium equations.

3.5 Strength of Materials Solution

A simple strength of materials approach was used to perform a non-linear membrane analysis of long cylindrical panels under internal pressure. The strength of materials analysis gives good approximations for center deflections and circumferential membrane strains for sufficiently thin panels. The circumferential membrane stress resultant can serve as an initial approximation for the shell stress resultant in the bending theory discussed in Section 3.3.5. Local effects such as the edge bending strain are not predicted from this analysis. An equivalent analysis for a curved plate is described in Reference 1.

The basic assumption of this analysis is that the initially circular panel remains circular when internally pressurized. Under an internal pressure p the panel with initial radius a deforms to an arc of a circle with a radius R. This deformation process is shown in Figure 6. Vertical equilibrium relates the circumferential stress
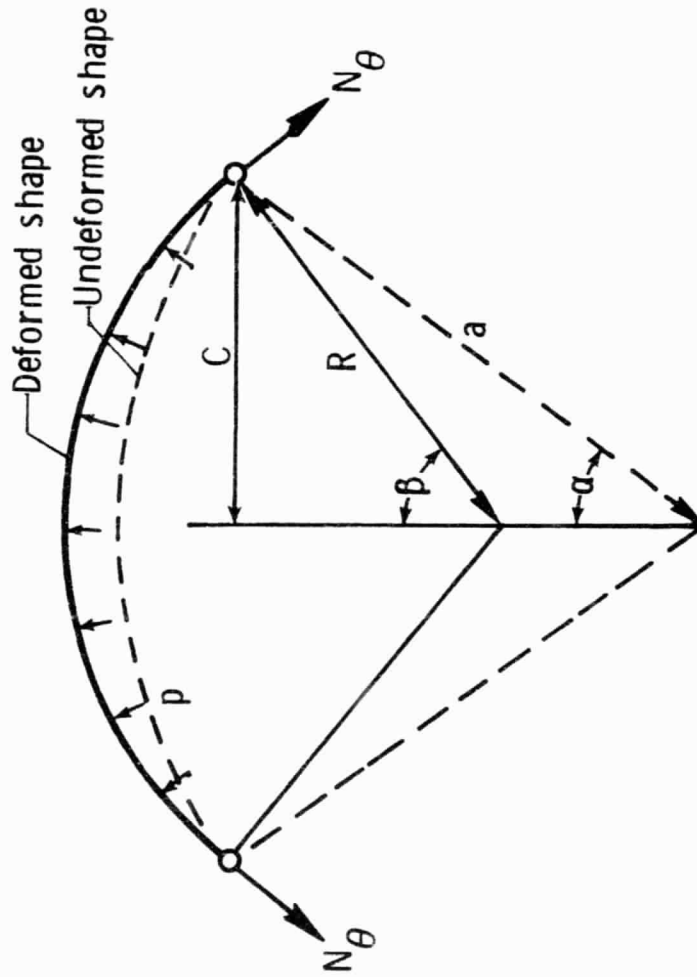
Figure 6.– Deformation response of a circular cylindrical membrane due to internal pressurization.

resultant N_θ to the pressure p and deformed radius R by the relation

$$N_\theta = pR \tag{3.102}$$

The constitutive relationship depends on the assumed axial strain state as follows:

$$\text{For} \quad \varepsilon_x^o = 0 \qquad N_\theta = A_{22}\varepsilon_\theta^o$$

$$\text{For} \quad N_x = 0 \qquad N_\theta = \left(A_{22} - \frac{A_{12}^2}{A_{11}}\right)\varepsilon_\theta^o \tag{3.103}$$

$$\text{For} \quad \varepsilon_x^o = \bar{\varepsilon}_x^o \qquad N_\theta - A_{12}\bar{\varepsilon}_x^o = A_{22}\varepsilon_\theta^o$$

These axial strain states are examined in Chapter 4. The geometric expression relating strain to deformation (change in radius) is

$$\varepsilon_\theta^o = \frac{\beta R - a\alpha}{a\alpha} \tag{3.104}$$

where the angles α and β are the semi-opening angles of the panel before and after deformation. Geometric compatibility requires

$$R \sin \beta = a \sin \alpha = C \tag{3.105}$$

where C denotes the half chord length shown in Figure 6. The equilibrium equation (3.102) is combined with an appropriate constitutive equations (3.103), the strain-displacement relation (3.104), and

geometric compatibility (3.105) to give an equation relating pressure to deformed radius. Using the constitutive relationship for the axial strain equal to zero, the equation is

$$p = \frac{R \sin^{-1} \frac{C}{R}}{a \sin^{-1} \frac{C}{a}} - 1 \ .$$

The solution may be obtained by solving this equation for the radius of the deformed panel R given the pressure p. Since this equation is transcendentally nonlinear in the unknown radius R, but linear in the pressure p, it is more expedient to solve the problem by choosing a value of R and calculating the corresponding pressure p. By successive approximation the radius can be determined for any given pressure. With the radius determined, other quantities such as center deflection and edge rotation may be calculated from simple geometric considerations. The center deflection (w_c) and edge rotation $(\gamma_e = \beta - \alpha)$ are

$$w_c = R[1 - \cos(\sin^{-1}(C/R))] - a[1 - \cos(\alpha)] \qquad (3.106)$$

$$\gamma_e = \sin^{-1}(C/R) - \sin^{-1}(C/a) \qquad (3.107)$$

Chapter 4

ANALYTICAL RESULTS

In this chapter analytical results for the different analyses described in Chapter 3 are presented. In Section 4.1 two-dimensional finite element results are used to validate the one-dimensional approximation solved analytically in Chapter 3. In Section 4.2 the geometrically nonlinear nature of the response of shallow cylindrical panels is illustrated by plotting center deflection and middle surface strain as a function of pressure for panels of differing stiffnesses. The circumferential surface strain distributions are given in Section 4.3 to illustrate the severity of the bending gradients at the edge, and to show the boundary layer decay lengths for the range of panels tested. In Section 4.4 the effects of a prescribed axial strain are discussed, and in Section 4.5 different boundary conditions are examined. The parametric studies in Sections 4.4 and 4.5 are useful for interpreting the experimental results, since ideal clamped boundary conditions were not achieved in the test fixture design. In Section 4.6 Kirchhoff-Love and shear deformation theories are compared to illustrate the importance of through-the-thickness shearing deformations in the bending boundary layer of the shell. Also the shear deformation theory for the one-dimensional analysis is used to assess the effect of the twist-curvature coupling ($D_{26} \neq 0$) of laminated composite shells.

65

4.1   Two-Dimensional Finite Element Results

Geometrically nonlinear computer analyses with the finite element
code STAGS (STructural Analysis of General Shells) (Ref. 18) were per-
formed on two panels representative of those tested.   The purposes of
the STAGS analyses were to identify regions of the panels where a one-
dimensional infinitely long cylindrical panel analysis was applicable,
and to validate the one-dimensional analytical solution.   A 5-ply ortho-
tropic panel and a 16-ply quasi-isotropic panel were chosen for the
STAGS analyses because these panels represent extremes in thickness and
lay-up of the test articles.   Thus, they were expected to exhibit
different response characteristics to the pressure loading.   Both panels
had a 60-inch radius, an 8-inch circumference, and were 20 inches long.
Clamped boundary conditions were applied to all four edges.   Since the
STAGS computer code does not have shearing deformation capability, the
clamped boundary conditions were modeled by constraining the three dis-
placements along the edge and the slope normal to the edge to be zero.

The 5-ply laminate had a layup of $[\pm45/90/\mp45]_T$ where the sign con-
vention for the fiber angle ϕ given in Figure 5 is used.   A contour
plot of the radial deflection is shown in Figure 7, and this figure re-
veals that the deflection is spatially uniform in the x-direction over a
center axial length of approximately 10 inches at a pressure of 1.3 psi.
This central area is the region in which a one-dimensional analysis is
appropriate.   The length of 10 inches for this central region of axial
uniformity is slightly less than the 12-inch estimate for this geometry
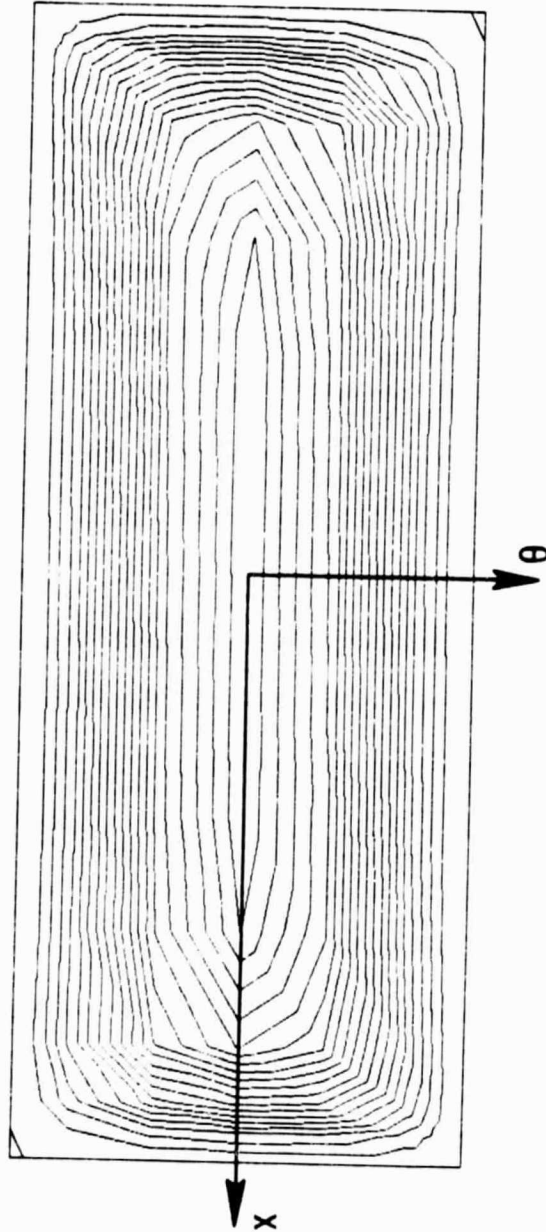following the argument given by Douglas as reported in Reference 1.

Figure 7.- Radial deflection contours of a 5-ply [±45/90̄]s panel from a STAGS analysis with 1.3 psi internal pressure.

In Figure 8 the center deflection from the STAGS analysis is compared
with center deflection from the one-dimensional shallow panel analysis
as a function of pressure. There is excellent correlation between the
two-dimensional and one-dimensional analyses.

The circumferential surface strain distributions for the two-
dimensional and one-dimensional analyses are shown in Figure 9 for the
5-ply panel. Besides showing that excellent agreement is obtained for
strains, Figure 9 illustrates an important advantage of the one-
dimensional analysis. Strains may be determined at any circumferential
point including the edge of the panel with the analytical solution. The
strains in the STAGS analysis are determined at the location of the cen-
troid of the finite element. Thus, interpolation is required to estimate
strains at other circumferential locations in the finite element method.
In particular, the strain gradient at the edge of the panel, which is
important for failure analysis and in estimating through-the-thickness
strains, may not be represented very accurately in the finite element
solution since to compute it would require even higher derivatives of
the basic displacement data. Since the majority of panels failed at the
straight edge, the one-dimensional analysis allows more insight into a
critical aspect of the problem than the finite element solutions.

Excellent agreement between the two-dimensional and one-dimensional
analyses was also obtained for the strains and displacements for a
16-ply laminate. Because of the increased stiffness of this panel over
the 5-ply panel, the portion of the axial length in which the one-
dimensional analysis is valid is decreased substantially. This distance
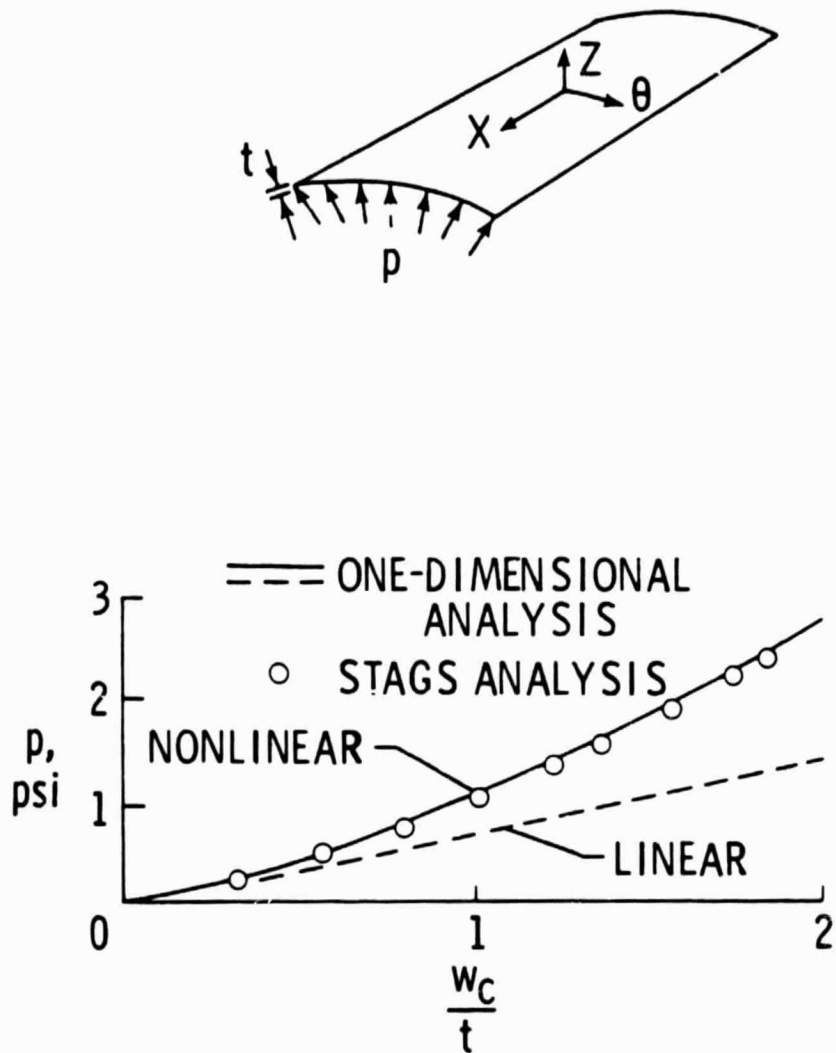
Figure 8.- Normalized center deflection of a 5-ply $[\pm 45/\overline{90}]_s$ panel from a two-dimensional nonlinear STAGS analysis and a one-dimensional nonlinear shallow panel analysis.
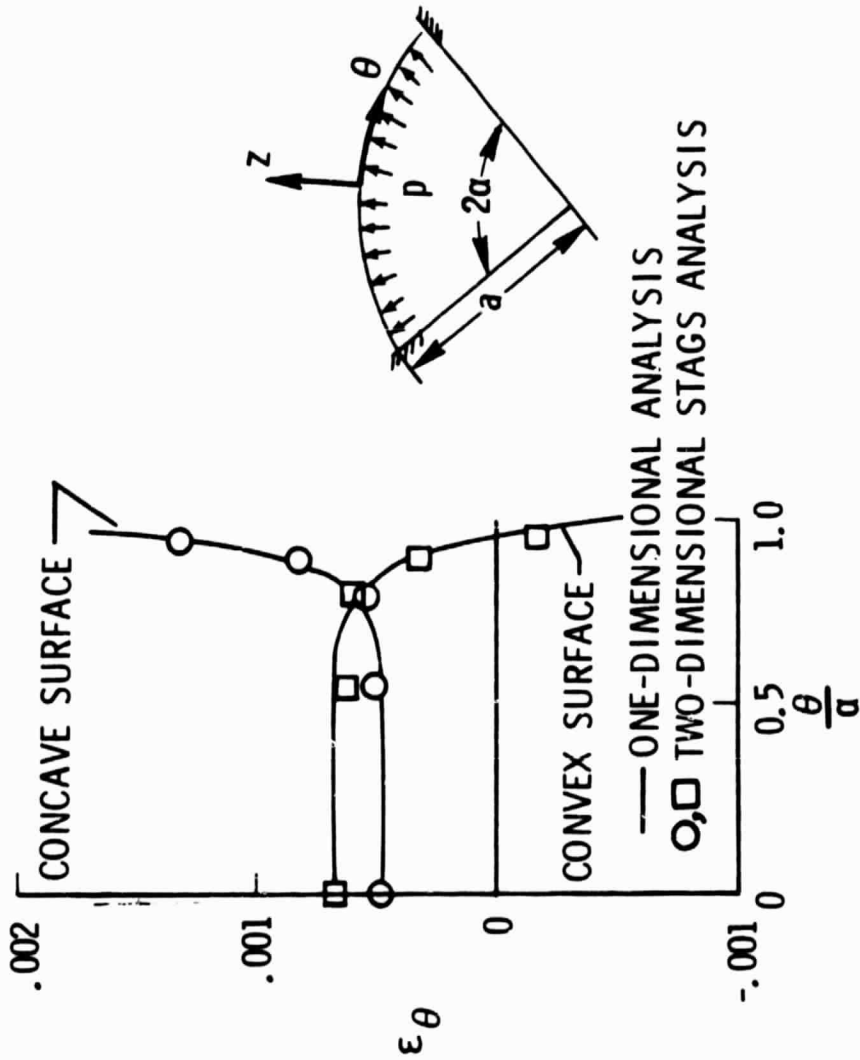
Figure 9.- STAGS and one-dimensional nonlinear shallow panel analysis results showing circumferential surface strain distribution along the circumferential center line (x=0.) of a 5-ply [±45/$\overline{90}$]$_s$ panel with 2.3 psi internal pressure.

is illustrated in Figure 10. The distribution of axial surface strains indicates bending occurs for a distance of .6 to .7 X/L away from the curved edges. The axial strain is equal to zero in the center of the panel as was true for the 5-ply laminate. This axial membrane strain state resulted from requiring that the axial displacement along the straight edge of the panels be zero in the STAGS model. The axial membrane strain was treated as a parameter in the one-dimensional analysis for infinitely long cylindrical panels.

4.2 The Importance of Geometric Nonlinearity

The stiffening effect caused by the geometric nonlinearity on the panel response with increasing pressure is shown in Figures 11 and 12. In Figure 11 the pressure is plotted as a function of center deflection normalized by the shell thickness for a 5-ply $[+45/ \overline{90}]_s$ laminate having an initial radius of 60 inches and an 8-inch arc length. The results from two nonlinear analyses are shown; the strength of materials membrane solution of Section 3.5, and the Kirchhoff-Love shell theory (which includes bending) given by equations (3.80) to (3.83). In addition the linear Kirchhoff-Love solutions given by equations (3.88) and (3.89) are also shown in Figure 11. As illustrated in this figure, there is little difference between the two nonlinear analyses which suggests that bending does not significantly affect the center deflection. However, there are significant differences between the linear and nonlinear solutions shown in Figure 11. The nonlinear solution is considerably stiffer than the linear solution even at low pressures.

72
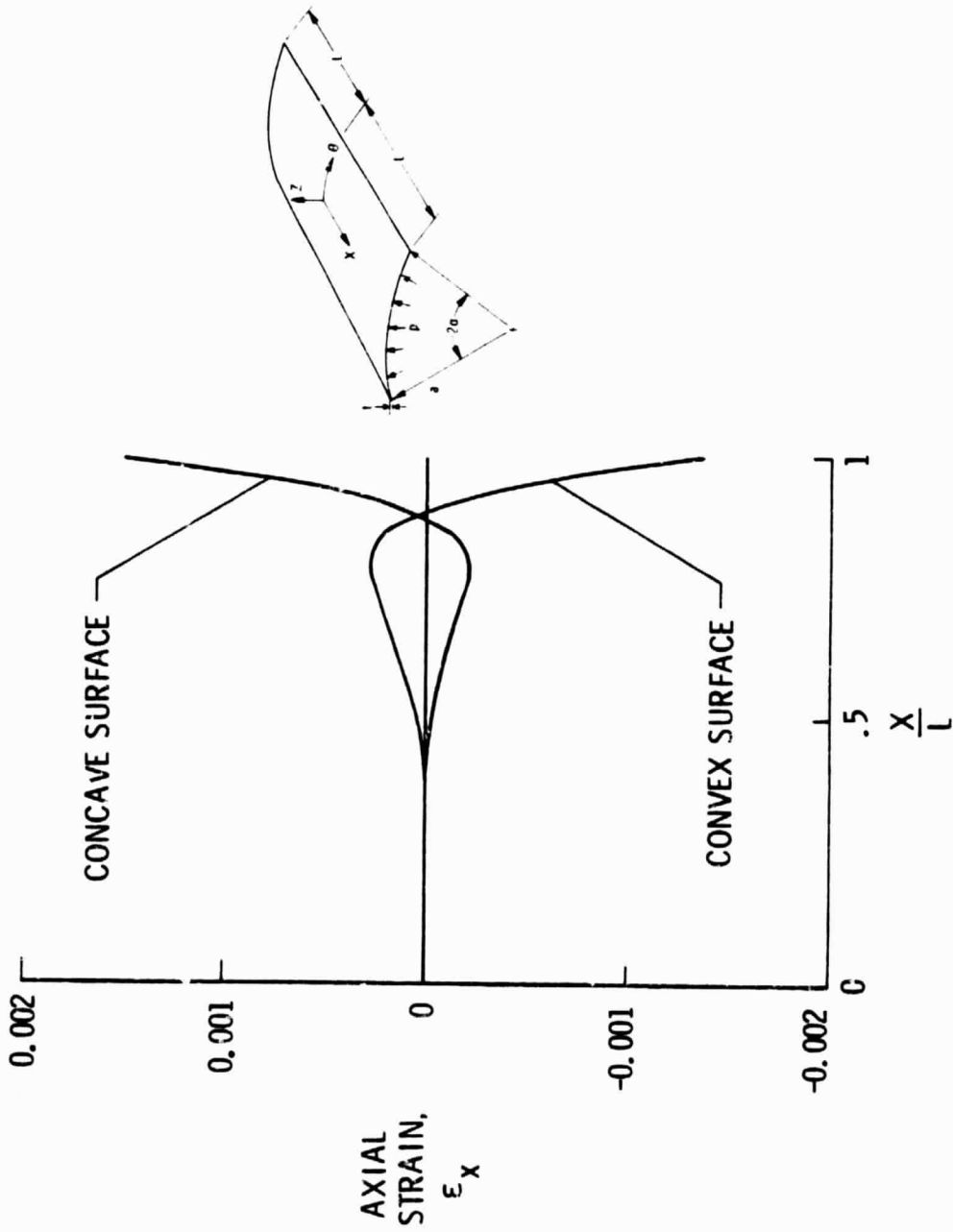
Figure 10.— STAGS results showing axial surface strain distribution along the axial center line ($\theta = 0.$) of a 16-ply $[\pm 45/\pm 45/90_2/0_2]_s$ panel with 8 psi internal pressure.
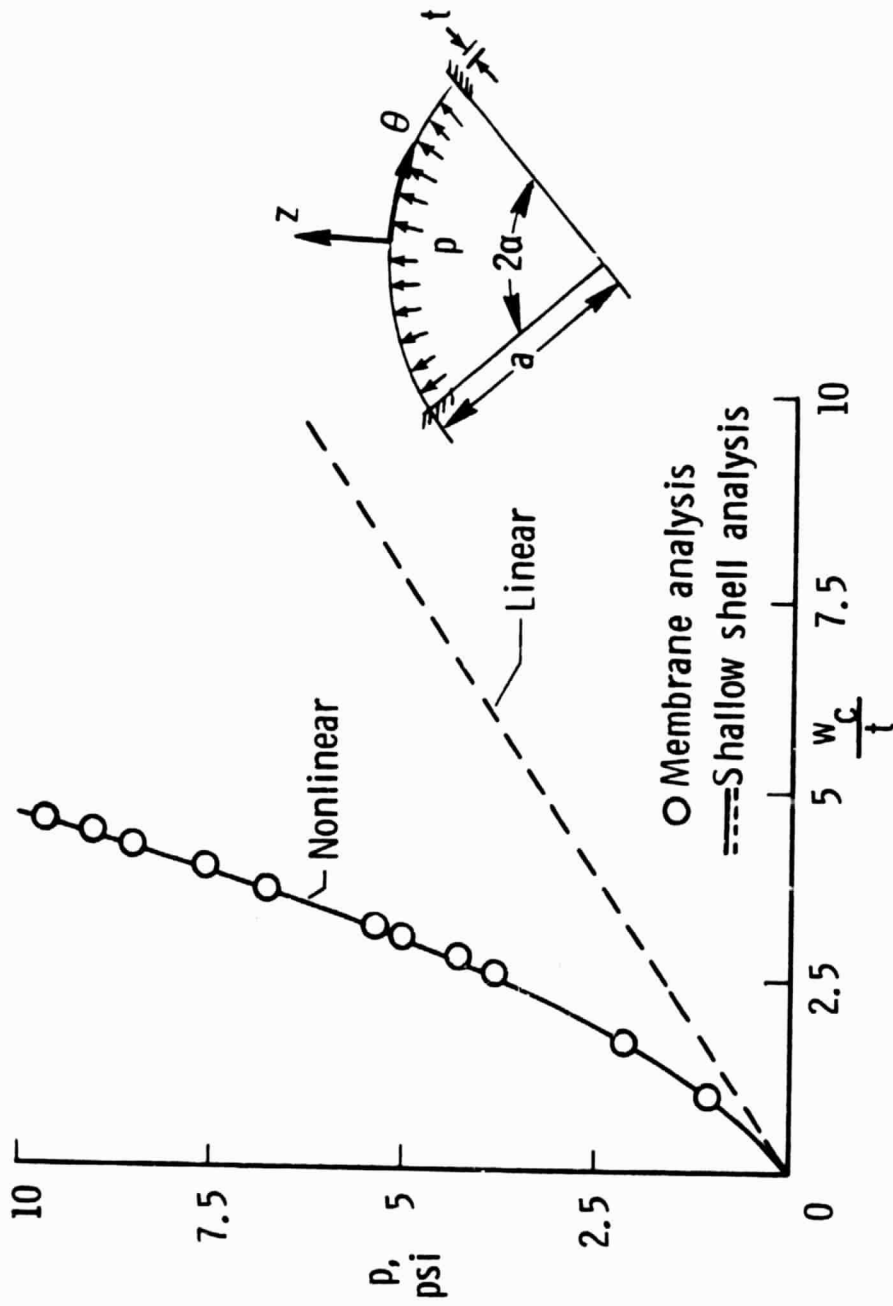
Figure 11.- A comparison of normalized center deflection response of a 5-ply $[\pm45/\overline{90}]_s$ predicted by three different theories.
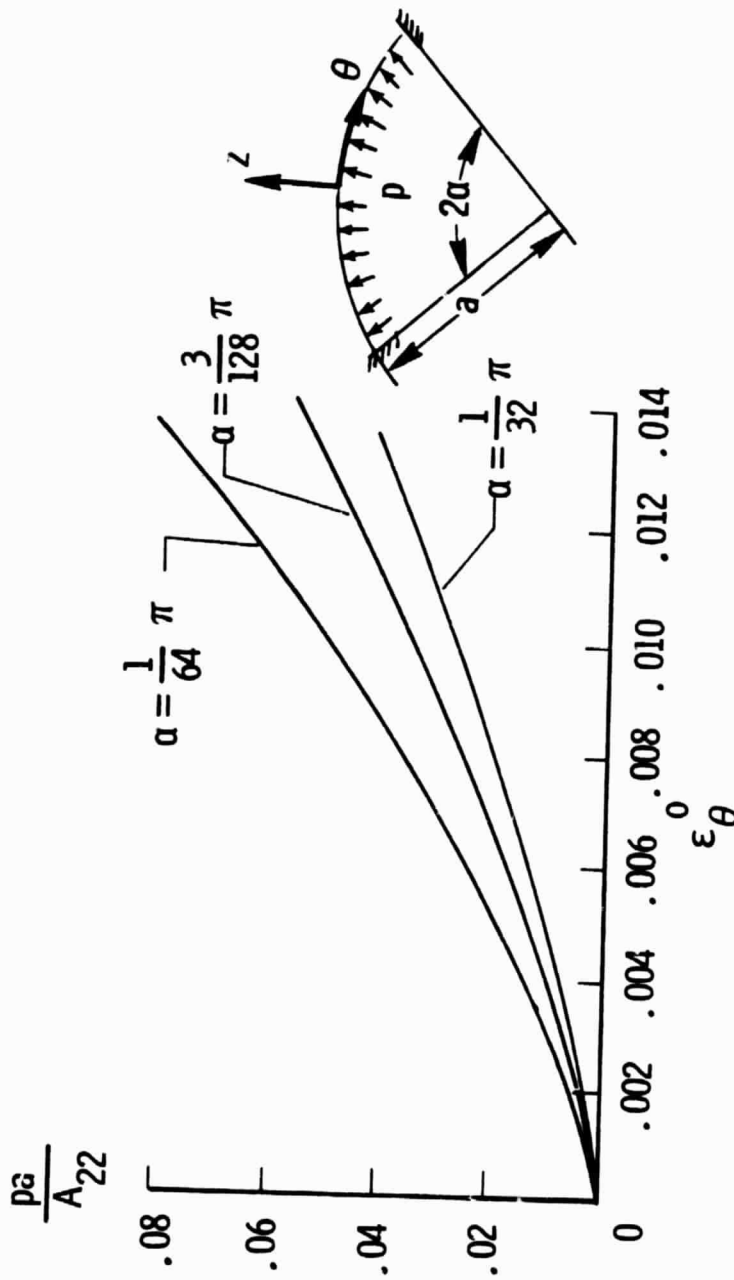
Figure 12.- Nonlinear membrane theory results showing circumferential membrane strain response to nondimensionalized pressure for three semi-opening angles (α).

For example, at a pressure of approximately 0.6 psi the linear theory predicts a center deflection equal to the panel thickness. The linear theory deflection is approximately 50 percent greater than the nonlinear theory deflection at 0.6 psi.

Figure 12 also shows the stiffening effect of the geometric non-linearity on a plot of normalized pressure pa/A_{22} versus circumferential membrane strain ε_θ^o for three different values of the semi-opening angle α. These results were obtained from the nonlinear membrane analysis presented in Section 3.5 (bending is neglected). Shallow panels are completely characterized by the semi-opening angle α; smaller values of α imply shallower panels. Figure 12 illustrates that for a fixed value of the pressure a shallower panel has a smaller membrane strain. In addition, the curves in Figure 11 provide a good estimate of the middle surface circumferential strain at a given value of the pressure for the more complex nonlinear panel analyses, which include both bending and membrane actions, presented in Chapter 3. Consequently, the elementary membrane solution closely predicts the center deflection and circumferential strain, but by definition ignores the bending at the panel boundaries.

The reason geometric nonlinearity is significant for a shallow internally pressurized panel can be found from the elementary membrane analysis in Section 3.5. For an increment in the arc length ds the following kinematic formulas can be derived from the equations in Section 3.5 for shallow panels:

$$\frac{dR}{ds} \approx -\frac{3}{2}\frac{1}{\alpha^3}$$

$$\frac{d\theta}{ds} \approx \frac{3}{4a}\frac{1}{\alpha^2}$$

$$\frac{dw_c}{ds} \approx \frac{3}{4}\frac{1}{\alpha} \, ,$$

in which R is the radius, θ is the rotation of the panel at its support, and w_c is the center deflection. The above formulas are obtained with the chord length fixed. The initial radius and semi-opening angle are denoted by a and α, respectively. These formulas show the decrease in radius, increase in edge rotation, and increase in center deflection are very sensitive to an increase in arc length for shallow panels. The increase in arc length may be a result of strain, or perhaps a slip at the edges in a test fixture. Thus there are significant changes in geometry in shallow panels for small changes in circumferential strain. Figure 13 shows the dramatic decrease in panel radius as the arc length increases for a panel with an initial radius a = 60 inches and initial arc length $2a\alpha$ = 8 inches. Finally, since equilibrium of the circular membrane requires N_θ = pR, it is clear that the decrease in radius at a constant pressure in the nonlinear analysis results in a smaller circumferential stress resultant than obtained from a linear analysis.

For laminates with considerable bending stiffness the nonlinear membrane effects becomes less important and bending resistance must be
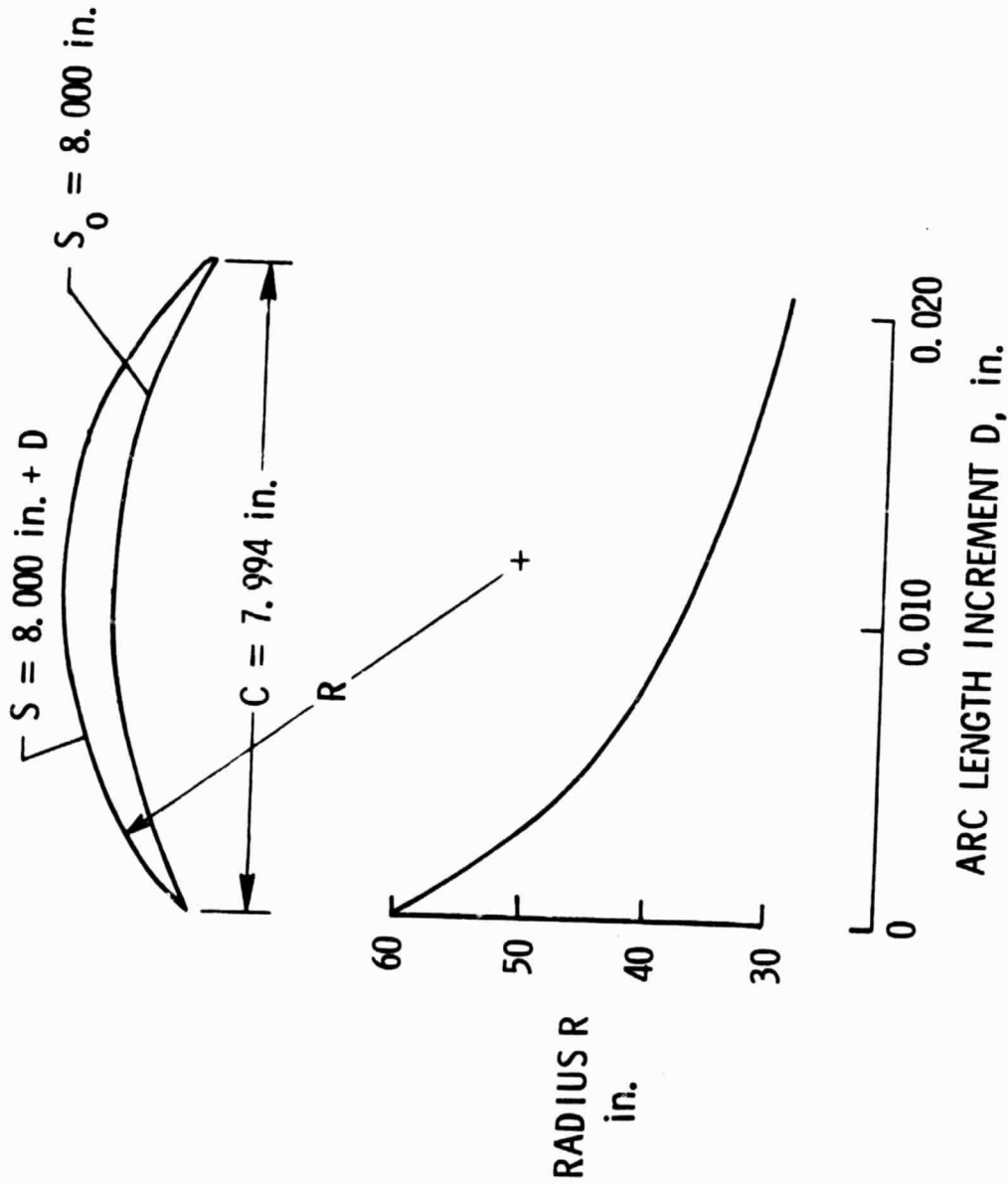
Figure 13.– Radius of an arc with a fixed chord as a function of the change in arc length.

taken into consideration. A solution to the linear shallow panel theory
which allows bending and extension was examined. This solution was
described in Section 3.3.6 (equations (3.87) to (3.89)). A nondimen-
sional plot of membrane strain and center deflection as a function of
nondimensional pressure is given in Figure 14 for values of the
parameter λ defined in the figure. The 4- to 16-ply panels examined
in this investigation have values of the λ parameter which fall
between values of 0 and 1. The lines representing an 8-ply and a 16-ply
panel are shown in the figure. The 4-ply laminate would be represented
by a line very close to the line $\lambda = 0$. The results given in Figure 14
are accurate for cases where the center deflection of a panel are less
than its wall thickness. For the 16-ply panel, the center deflection is
greater than the wall thickness for pressures less than 10 psi. There-
fore, linear results cannot provide accurate predictions for thin panels
at pressures above 10 psi.

The effect of panel thickness on the response is shown in
Figures 15 and 16. Each panel has a common initial radius of 60 inches
and a common middle surface arc length of 8 inches. The thicknesses of
the 4-ply, 8-ply, and 16-ply panels are 0.0208, 0.0416, and
0.0832 inch, respectively. The pressure versus center deflection in
Figure 15 and the pressure versus membrane strain in Figure 16, are
obtained from the nonlinear panel analysis of Section 3.3. These
results show that the response is nonlinear even at moderate pressures
for the thicker 16-ply panel. As would be anticipated, the thinner
panels are more compliant.
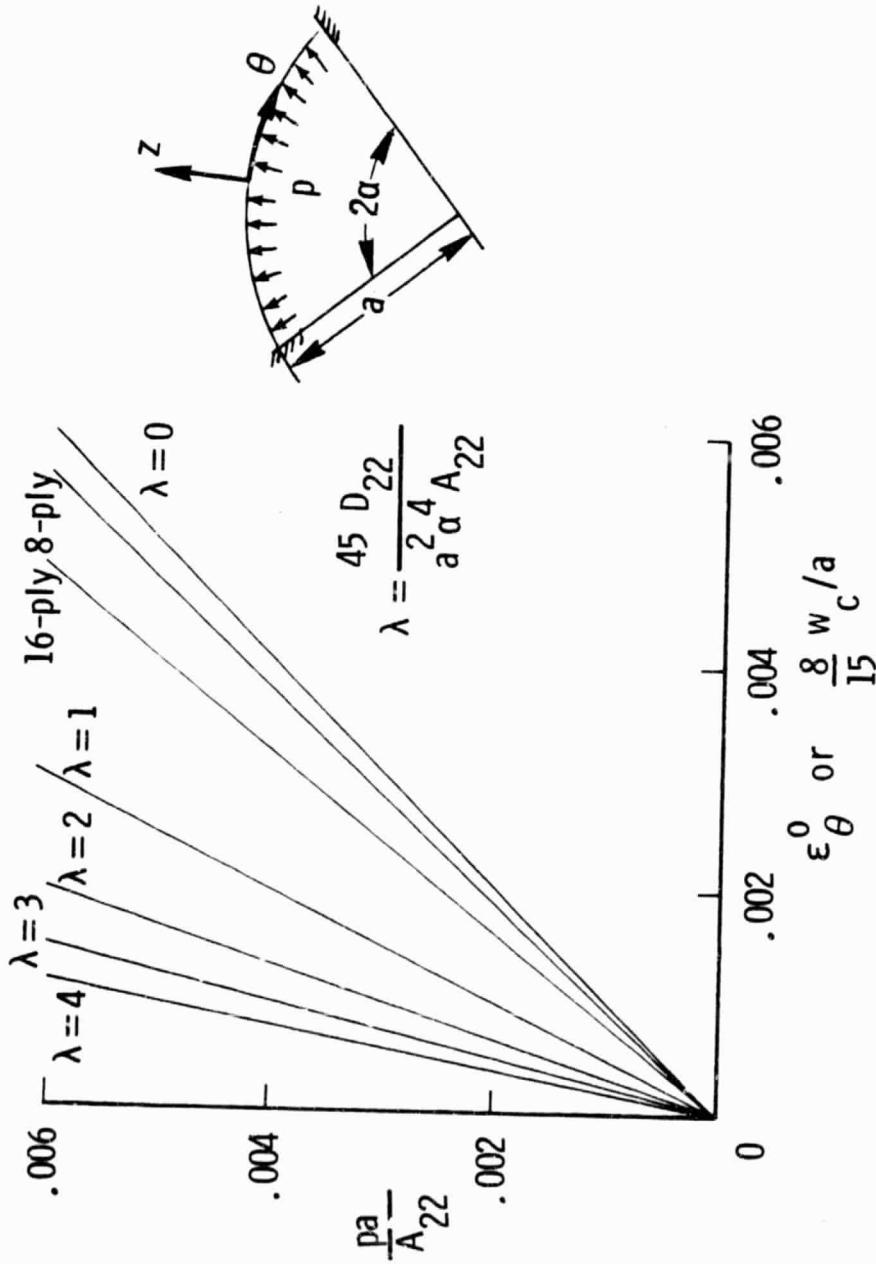
Figure 14.- Linear shallow panel theory results showing circumferential middle surface strain and nondimensional center deflection response to nondimensionalized pressure for various values of the elastic-geometric parameter λ.

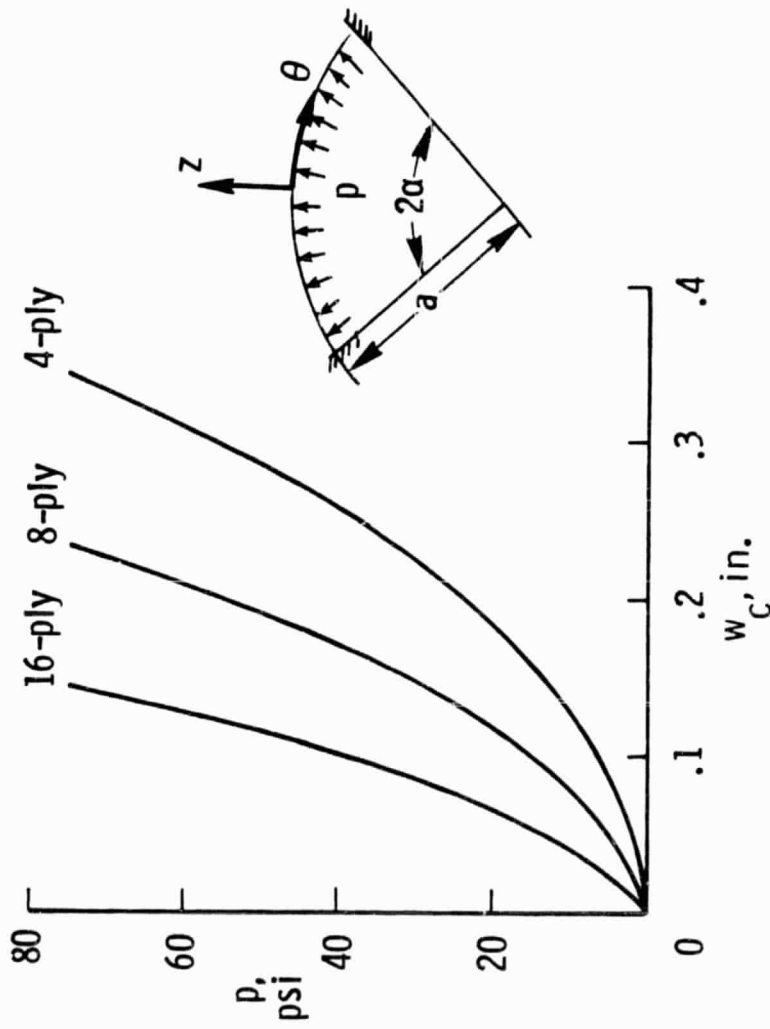Figure 15.- Nonlinear shallow panel theory results showing center deflection response to pressure for a 4-, 8-, and 16-ply panel.
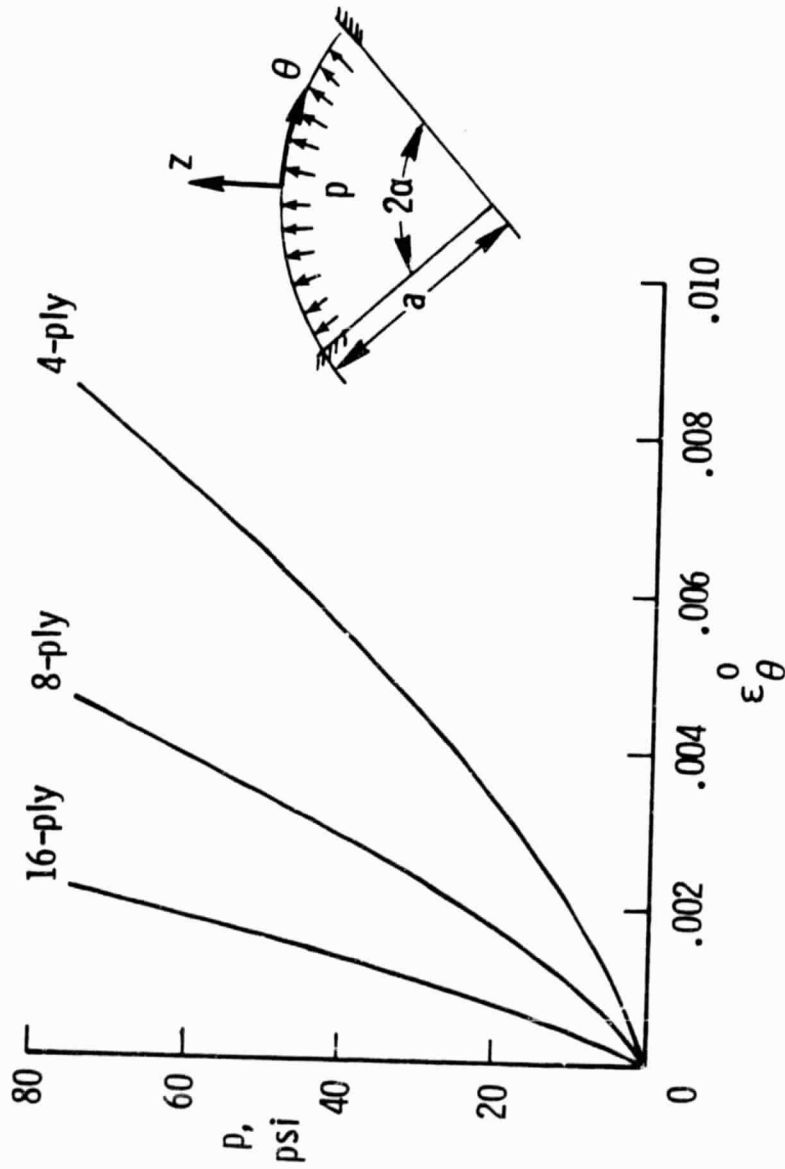
Figure 16.— Nonlinear shallow panel theory results showing circumferential middle surface strain response to pressure for a 4-, 8-, and 16-ply panel.

4.3 Circumferential Strain Distributions

The circumferential surface strain distributions of an 8-ply laminate are shown in Figure 17 for the nonlinear membrane analysis (Sec. 3.5), and the linear and nonlinear shallow shell analyses (Sec. 3.3.6) with the Kirchhoff-Love assumption. A great deal of variation exists between these analyses. The nonlinear shallow cylindrical panel analysis exhibits an edge bending boundary layer visible in Figure 17 and represented mathematically by the exponential terms in the homogeneous solution given in equation (3.80). A boundary layer is not distinct for the linear solution given in Figure 17. The linear solution given in equation (3.88) does not exhibit a bending boundary layer; i.e., the homogeneous solution does not have exponential functions in the solution. The strains predicted by the nonlinear shallow shell analysis are uniform away from the clamped edge. The bending strains increase substantially in a narrow region near the edge, which is referred to as the edge bending boundary layer. The nonlinear membrane analysis approximates the center bending strain, but cannot predict any local edge bending. (The bending strains for the nonlinear membrane analysis were calculated from the change in curvature of the deformed and undeformed radii of the circular arcs shown in Figure 6.) Although the linear analysis overpredicts the maximum value of the tensile strain in this 8-ply example, it cannot in general be used for conservative design. In a 5-ply example, the edge surface strains determined from nonlinear analysis exceeded those predicted from the linear analysis on
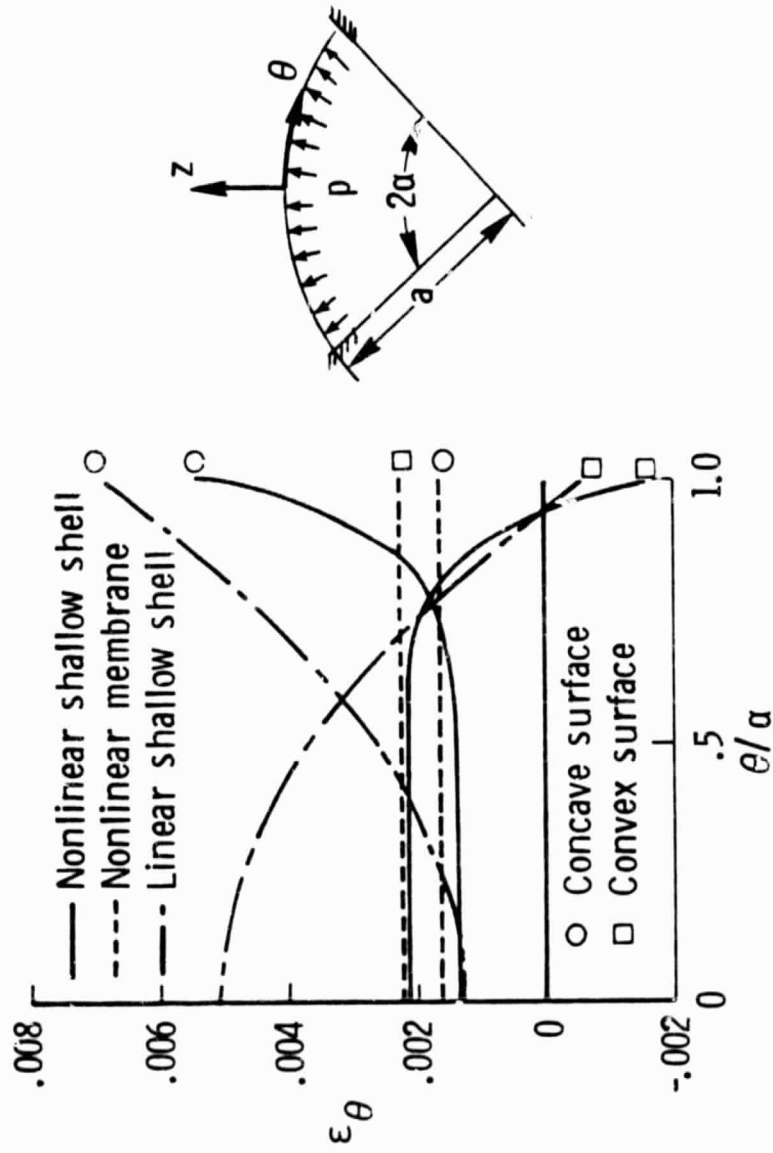
83

Figure 17.- Comparison between circumferential surface strain distributions generated by nonlinear membrane theory, and linear and nonlinear Kirchhoff-Love shallow shell theories.

both the concave and convex surfaces. The nonlinear and linear analyses agree more closely for thicker panels.

Laminate bending stiffness plays an important role in the character of the local bending boundary layer exhibited in the nonlinear shallow cylindrical panel analysis. The character of this boundary layer is represented in Figure 18 where normalized bending strain distributions are given for 4-, 8-, and 16-ply laminates at 20 psi pressure. The inside surface strains were normalized to allow comparisons between the panels of three different thicknesses. The middle surface membrane strain was subtracted from the concave surface strain of each panel. The membrane strain is a spatial constant so the above subtraction yields the bending strain distribution. The distributions were normalized to go to the value of -1 at the center by dividing the bending strain distribution by the value of center bending strain. Figure 18 shows the bending is uniform over most of the circumference for the 4-ply laminate with a boundary layer width of 0.75 inches. The boundary layer width may be easily determined in the bottom portion of the figure where the vertical scale has been greatly magnified. From this enlargement it rav be seen that bending varies over the entire circumference of the 16-ply laminate. The edge bending strain normalization factor is largest for the thinnest panel. The bending strain distribution for the convex surface would be identical in shape but inverted with respect to the abscissa.

The boundary decay length of the Kirchoff-Love shallow shell theory is expressed mathematically by equation (3.68) where the value of λ is
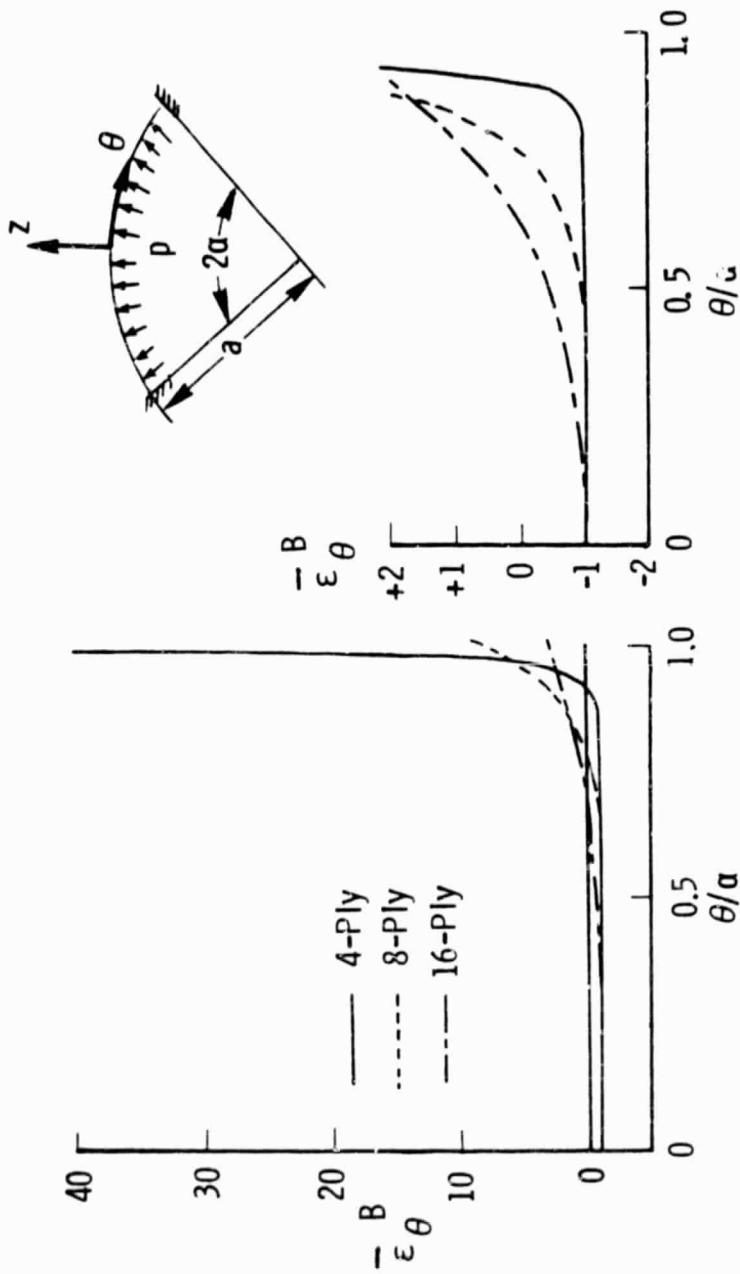
Figure 18.- Nonlinear shallow panel theory results showing normalized circumferential bending strain distribution on the concave surface of 4-, 8-, and 16-ply panels.

given by equation (3.81). The boundary decay length is plotted in Figure 19 for 4-, 8- and 16-ply laminates as a function of pressure with $\varepsilon = 0.01$ in equation (3.68). The boundary decay length is inversely proportional to the square root of the circumferential stress resultant and therefore decreases with pressure for all the laminates. Since the decay lengths are short and edge bending strains larger for the thinner panels, bending gradients are more severe for these panels than the thicker panels.

4.4 Effect of an Applied Axial Strain

The results of the previous sections are based on analyses which assume that the axial strain is zero. Tensile axial middle surface strains were measured experimentally and for this reason it is important to understand this effect. In this section the nonlinear membrane and bending analyses are used to examine three axial strain states. In the first case the axial stress resultant is set to zero. This state occurs when free axial contraction is allowed due to the Poisson affect and is the correct state for an arch as opposed to a long cylindrical shell. A negative axial strain results from the Poisson contraction. In the second case the axial strain is set to zero. This state is the one pre- dicted by the STAGS analysis in the central panel section away from the curved edges and is the correct state for a long cylindrical shell with axial displacements along the straight edge constrained. A tensile membrane stress resultant is present for the second case. In the third case a tensile membrane strain is applied. For purposes of this
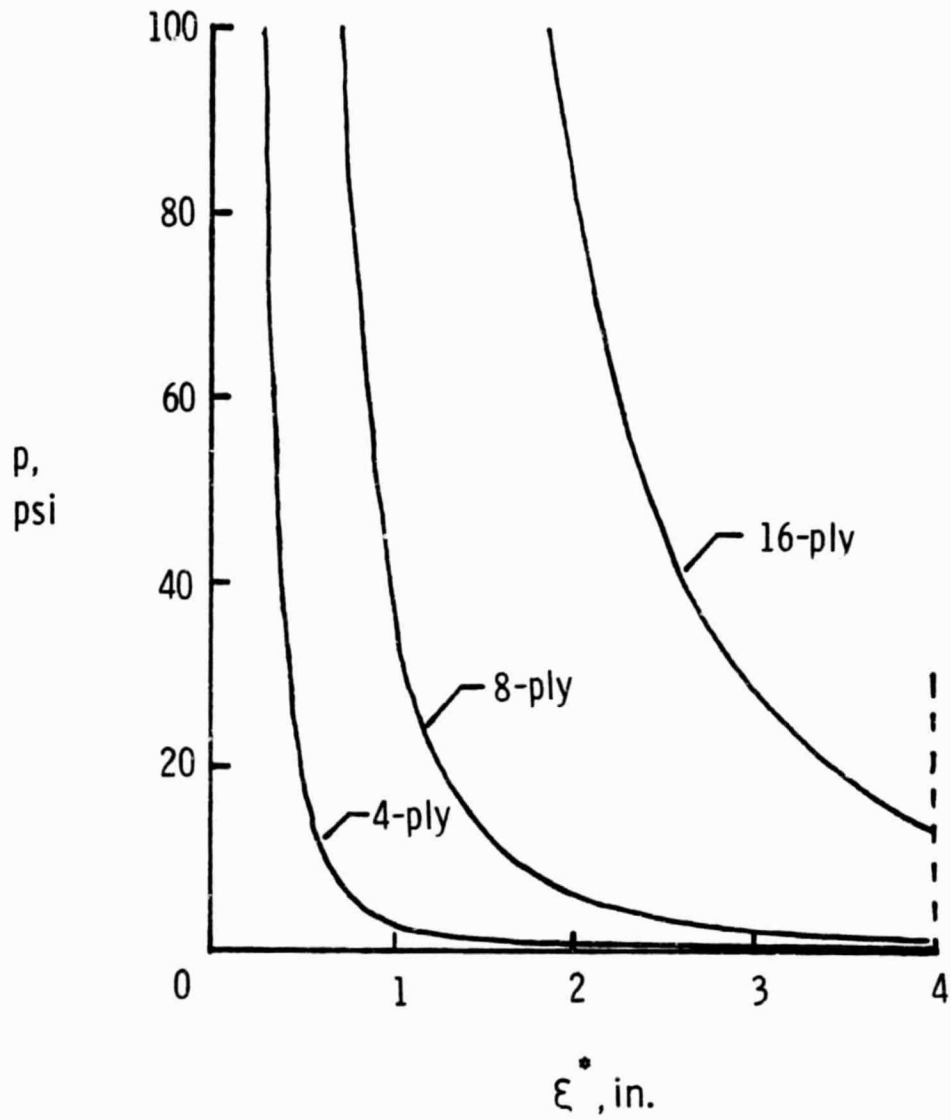
C - 2

Figure 19.- Boundary decay length as a function of internal pressure for 4-,
8-, and 16-ply.

comparison the value of this strain was chosen to be equal to the magnitude of the negative strain which results from lateral contraction in the first case where the axial stress resultant is zero. Prescribed axial strains ($\bar{\epsilon}$) and stress resultants (N_x) were applied to an 8-ply quasi-isotropic $[\pm 45/90/0]_s$ laminate with a 60-inch initial radius and 8-inch arc length at a pressure of 20 psi. Numerical results are presented in Table 2 for the membrane and bending solutions. Circumferential membrane strain, circumferential stress resultant, and center deflection are given for the membrane solution in the table. The same physical quantities along with the edge bending strain and the middle surface interlaminar shear stress ($\tau_{\theta z}$) at the edge are given for the bending solution in the table. Both the circumferential membrane strain and the center deflection decrease as the axial strain increases for both the bending and membrane solution. Conversely, the circumferential stress resultant increases due to the Poisson effect. Comparing the membrane and bending theories the circumferential membrane strain and center deflection are approximately 9 percent and 2 percent larger, respectively, when calculated from membrane theory. For the bending theory the edge bending strain and shearing stress decrease as the axial strain increases.

4.5 Circumferential Boundary Conditions

Boundary conditions were examined to study their influence on both the panel center and edge responses. Also, the results were used to model closely the actual conditions on the panels as tested. This

Table 2. Effect of Axial Strain on Stress and Deflection Results
Calculated with Membrane and Bending Theory (8- ply
Specimen, p = 20 psi)

Membrane Theory

$\bar{\varepsilon}$	N_x, $\dfrac{lb}{in.}$	ε_θ°	N_θ, $\dfrac{lb}{in.}$	$\dfrac{w_c}{t}$	R, in.
-.000623	0.	.00196	630.	2.81	31.5
0.0	206.	.00181	648.	2.64	32.4
.000623	412.	.00167	667.	2.48	33.4

Bending Theory

$\bar{\varepsilon}$	N_x, $\dfrac{lb}{in.}$	ε_θ°	N_θ, $\dfrac{lb}{in.}$	$\dfrac{w_c}{t}$	ε_θ^b	$\dfrac{\tau_{\theta z}^\circ}{p}$
-.000623	0.	.00181	587.	2.76	.00477	-79.4
0.0	206.	.00167	606.	2.59	.00455	-76.9
.000623	412.	.00152	627.	2.42	.00432	-74.1

modeling of actual conditions was accomplished by measurement of boundary displacements. An additional reason for examination of boundary conditions is that the examination allows representation of actual fuselage conditions which are very difficult to simulate experimentally. Edge displacements, v^o and w^o, and edge rotation, $\frac{1}{a}\frac{dw^o}{d\theta}$, boundary conditions were examined and are discussed in individual sections. These three conditions $\left(v^o, \quad w^o, \text{ and } \frac{1}{a}\frac{dw^o}{d\theta}\right)$ are given by equations (3.77) – (3.79). The axial condition was satisfied by the assumptions that $u^o = 0$ along the edge of the panel.

4.5.1 Circumferential Displacement Condition

The effect of circumferential displacements or slip is shown in Figure 20 for a 16-ply panel at 20 psi. In this figure the concave and convex edge strains are plotted as the circumferential slip is allowed to increase from 0 to 0.020 inches. The membrane strain is also plotted and goes through zero as the slip increases and becomes compressive for higher values of slip. The bending strains represented by one-half the difference between the concave and convex strains increased substantially in the process. These results are very informative in explaining events which occurred when the test panels slipped circumferentially in the clamped edge supports under internal pressurization. This circumferential slipping will be discussed further in Section 5.1.

4.5.2 Radial Spring Boundary Condition

In an actual fuselage the skin may deform radially at the stiffener. This deformation is difficult to duplicate experimentally without
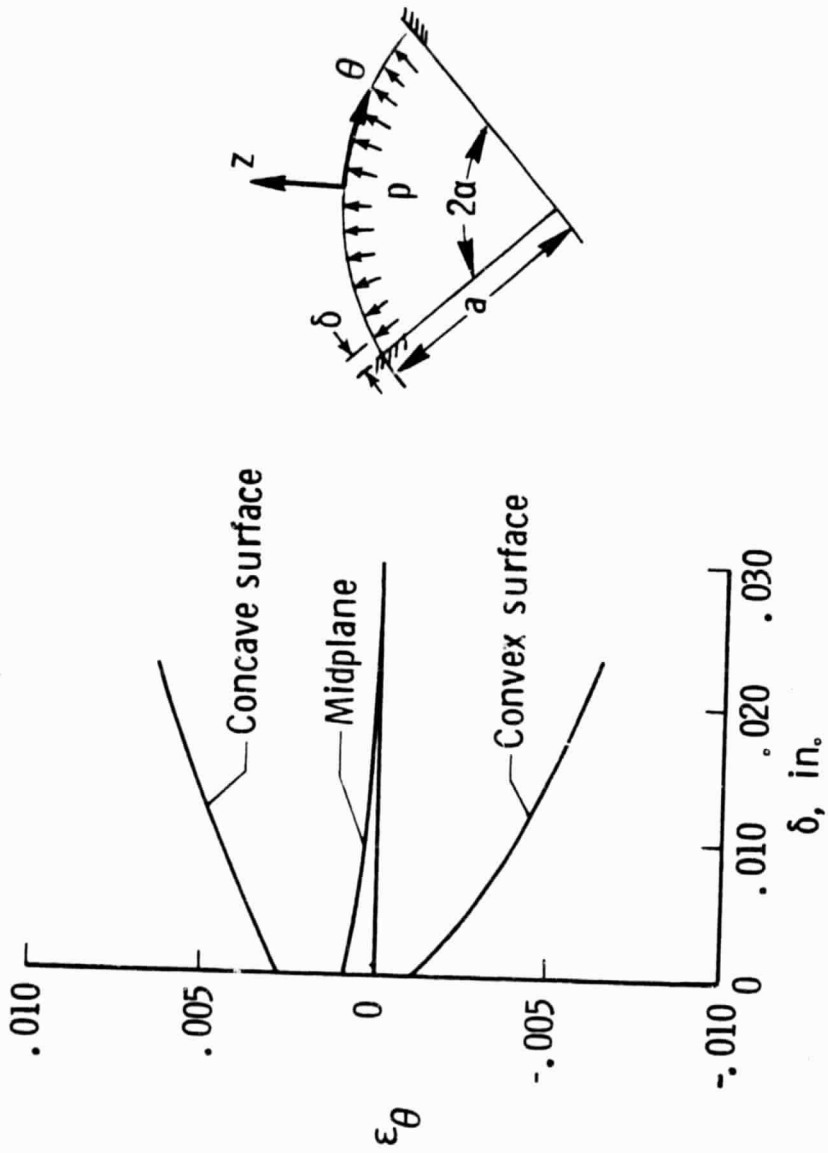
Figure 20.- Effect of circumferential boundary slip on circumferential edge strain for a 16-ply $[90_2/0_2/\pm45/\pm45]_s$ panel with 20 psi internal pressure.

testing a complete stiffened cylinder. However, it can be examined analytically by allowing the skin support to deform radially through the use of an extensional spring. To address the problem a special analysis was conducted in which the boundary condition on w^o (see equation (3.78)) was replaced by the more general condition of a radial spring support with stiffness K. Shearing deformations were not included in this analysis. The solution procedure was similar to the procedure described in Section 3.3.5. The effect of radial spring stiffness on the membrane stress resultant for a 4- and 16-ply laminate is shown in Figure 21. As the radial spring stiffness K goes to zero the membrane stress resultant approaches the complete cylinder hoop tension solution (hoop tension equals pressure times original radius). The deviation between the linear and nonlinear solution is larger for the 4-ply panel than the 16-ply panel. The 16-ply panel carries a large portion of the load through bending, whereas the 4-ply panel stretches more with the resulting decreased radius and carries the pressure through the nonlinear membrane action. For low radial spring stiffness these results indicate that geometrically nonlinear effects are less important.

Circumferential surface strain distributions are shown in Figure 22 at 30 psi pressure for one panel which has a radial spring stiffness K of 100 lb/in. and for one radially constrained panel. Results for these otherwise identical panels were obtained with the nonlinear shallow panel analysis. The difference in the membrane circumferential strain
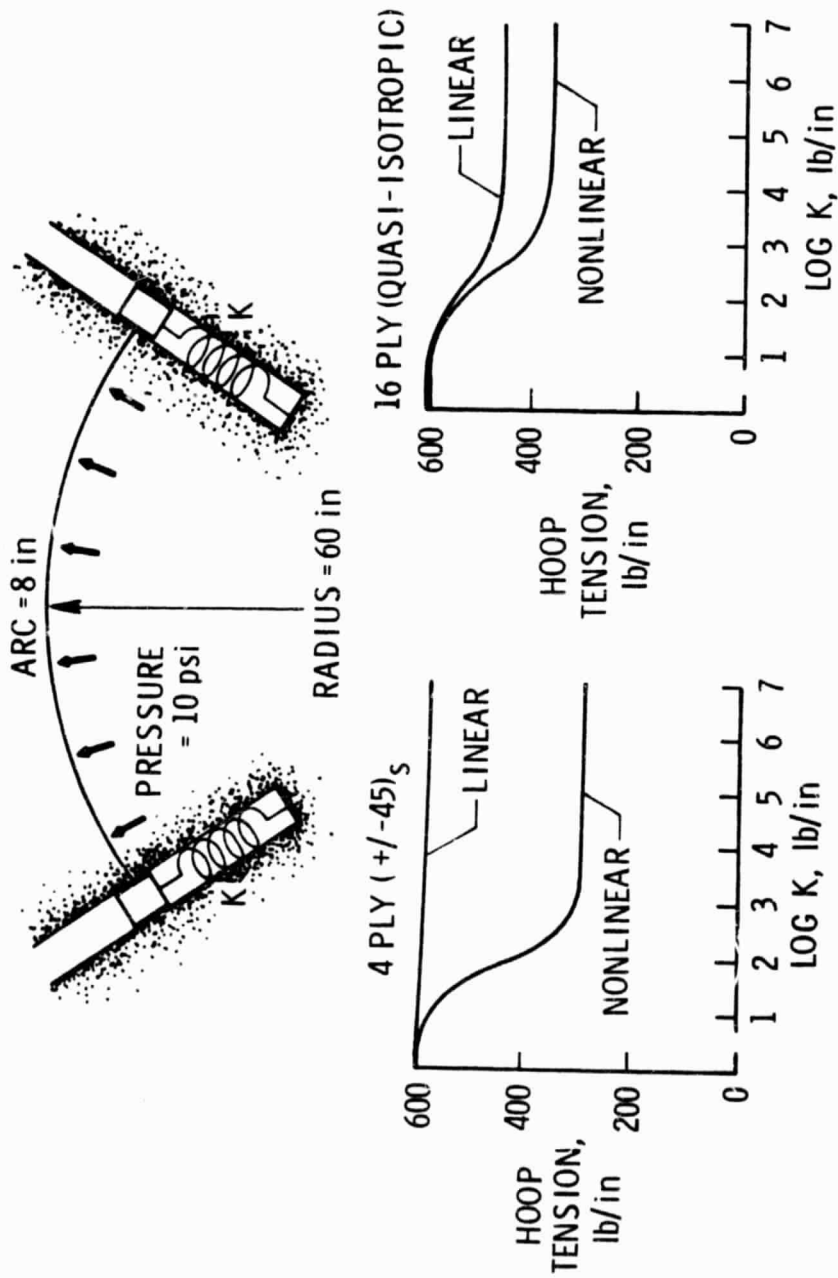
Figure 21.- Effect of radial spring stiffness on the circumferential stress resultant.
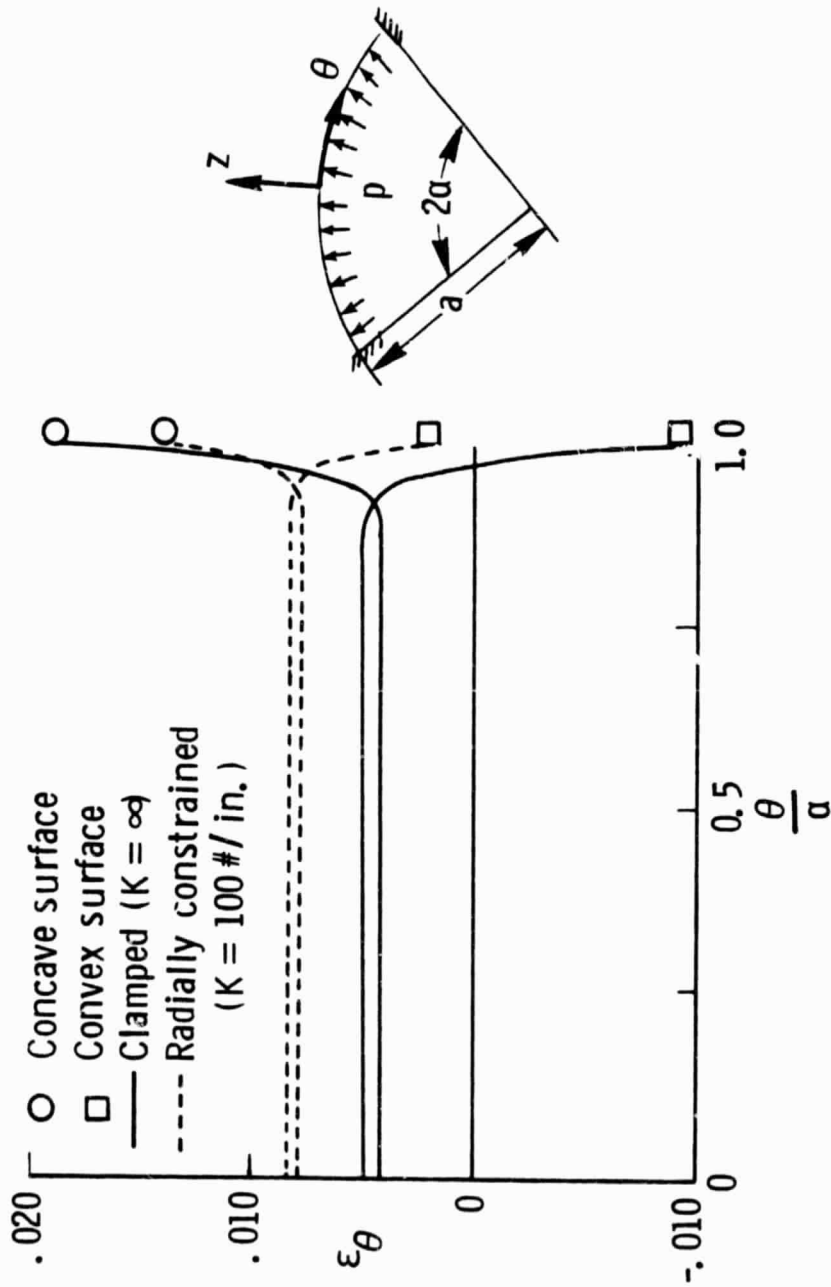
Figure 22.- Circumferential surface strain distributions for 4-ply [±45]$_s$ panels which are rigidly and elastically restrained in the radial direction.

agrees with results shown earlier in Figure 21. The additional informa-
tion determined from this plot is that severe bending gradients at the
edge still exists for the finite radial spring stiffness. The largest
strains still occur at the edge, but the bending strains are decreased.

4.5.3 Rotational Boundary Condition

The effects of edge circumferential rotation $\left(\psi_\theta = -\frac{1}{a}\frac{dw^o}{d\theta}\right)$ are
bound by considering clamped ($\psi_\theta = 0$) and simply supported ($M_\theta = 0$)
boundary conditions with shearing deformations suppressed. The solution
for clamped boundary conditions is given by equation (3.80) and a solu-
tion for simply supported boundary conditions is derived similarly.
Radial, circumferential, and axial displacements (w^o, v^o, and u^o) at
the edge were set to zero to avoid the unnecessary introduction of addi-
tional variables.

The membrane strain response of an 8-ply laminate is shown in
Figure 23 for clamped and simply supported boundary conditions. The
membrane strain is slightly higher for the simply supported condition.
Although not shown, there is little difference between the center
deflections for clamped and simply supported boundary conditions. The
deflection for simply supported conditions are slightly greater than for
the clamped condition. The difference between the membrane strain and
central deflection for simply supported and clamped boundary conditions
increases with bending stiffness. However, for the 4- to 16-ply panels
tested, the rotational constraint did not have a large influence on the
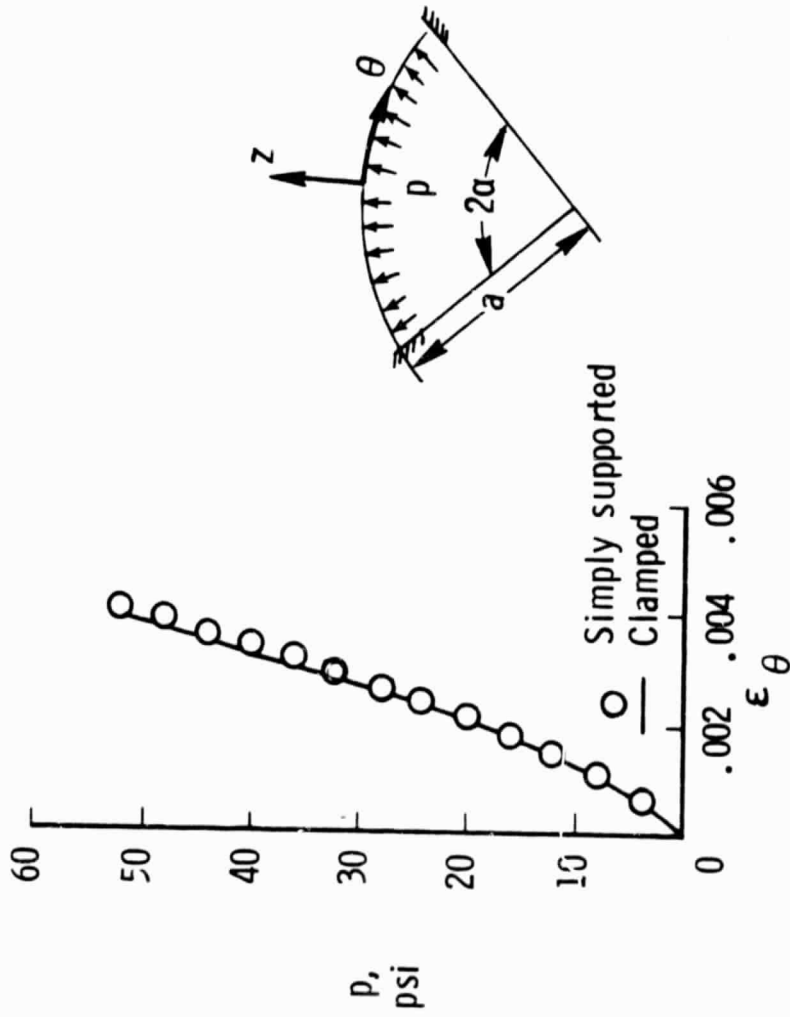center deflection and circumferential middle surface strain.

Figure 23.– Circumferential membrane strain response to internal pressure of a 8-ply [±45]$_s$ panel with clamped and simply supported edges.

The edge bending strains were significantly influenced by the rotational edge support. Circumferential surface strain distributions are shown in Figure 24 for an 8-ply quasi-isotropic panel with simply supported and clamped boundary conditions. The bending strain is a maximum at the edge for the clamped condition and is zero for the simply supported condition. The predicted failure location for the clamped panel is at the edge and away from the edge for the simply supported panel. The rotation constraint therefore has a major effect on the response at the edges but only a minor effect on the response at the center of the panel.

4.6 Influence of Through-the-Thickness Shear Deformation

Shear deformation is important for metal structures with a span-to-thickness ratio less than about 10. For materials which have a high E_{11}/G_{12} ratio, such as graphite-epoxy, shear deformation effects may be important for higher span-to-thickness ratios. The panels tested have span-to-thickness ratios greater than 80 but their graphite-epoxy material construction and the rapid variation of bending moment at the edge, make consideration of shear deformation important. The effects of through-the-thickness shearing deformations are approximated by allowing the normal to the middle surface to rotate independently of the circumferential and axial line elements in the deformed middle surface. Thus, the right angle between the normal and circumferential line elements is not preserved during deformation, i.e., shear strain $\gamma_{z\theta}^{o} \neq 0$.
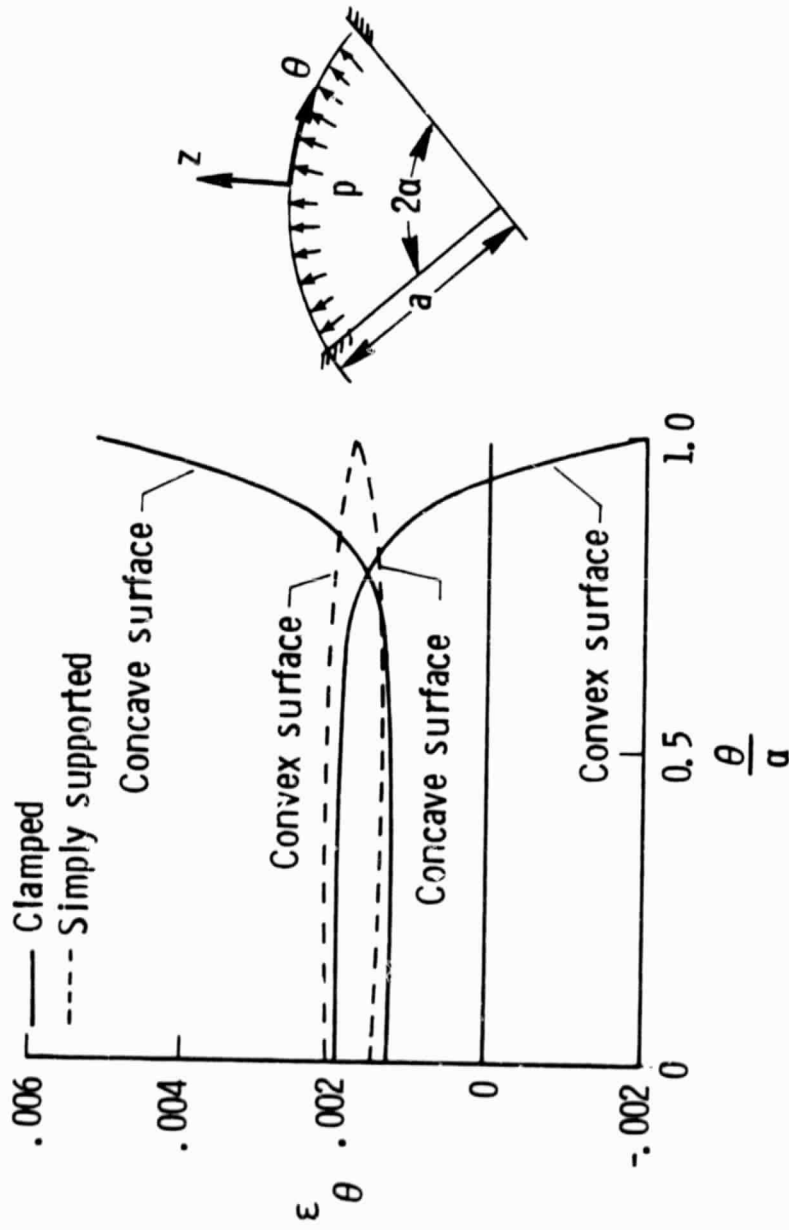
Figure 24.- Circumferential surface strain distributions for 8-ply [90/0/±45]$_s$ panel with simply supported and clamped boundary conditions.

Similarly, the right angle between the normal and the axial line elements is not preserved during deformation, i.e., shear strain $\gamma_{zx}^o \neq 0$. For the long panel analysis developed in Section 3.3, the shear strain γ_{zx}^o may also be nonzero since the normal can rotate through an angle ψ_x out of the $z-\theta$ plane even though the axial line element is restricted not to rotate. Hence $\gamma_{zx}^o = \psi_x$. However, $\gamma_{zx}^o \neq 0$ occurs in the long panel analysis only if the twist coupling coefficient $D_{26} \neq 0$. In lamination theory $D_{26} \neq 0$ reflects the material coupling between circumferential normal stress and the shear strain $\gamma_{x\theta}$ on a parallel surface. The inplane shear strain $\gamma_{x\theta}$ on a parallel surface is determined, in part, by the change in the rotation of the normal out of the $\theta-z$ plane along the circumferential arc length, or mathematically by $\frac{1}{a}\frac{\partial \psi_x}{\partial \theta}$. If $D_{26} \neq 0$, as it is for the laminates in this study, circumferential bending is accompanied by a nonzero rotation gradient $\frac{1}{a}\frac{\partial \psi_x}{\partial \theta}$, which implies $\psi_x \neq 0$, and hence a nonzero shear strain γ_{xz} results.

The distribution of the through-the-thickness shear strain γ_{xz}^o predicted by the shear deformation solution of Section 3.3.5 is shown in Figure 25 for a 4-ply $[\pm 45]_s$ laminate at 100 psi. The shear strain γ_{zx}^o is zero over most of the circumferential arc length in Figure 25 except for a narrow region near the edge. In this edge region γ_{zx}^o changes very rapidly, attains a peak value very close to the edge, and then returns to zero at the edge. Since ψ_x is prescribed to vanish at the clamped edge, and $\gamma_{zx}^o = \psi_x$, γ_{zx}^o must vanish at the edge also. As discussed in the previous paragraph, if $D_{26} = 0$, then the shear strain
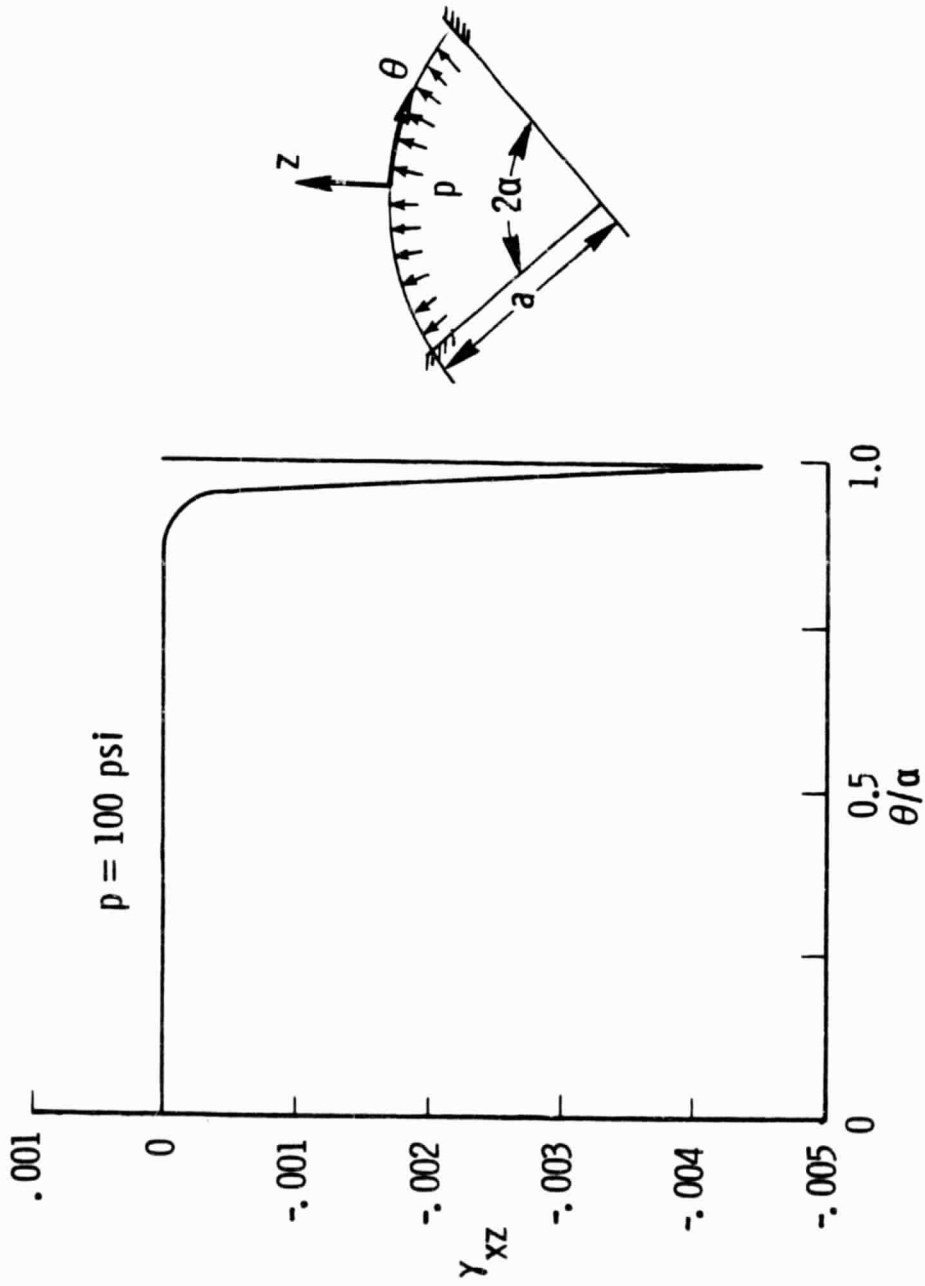
Figure 25.- Circumferential distribution of axial transverse shear strain for a 4-ply [±45]$_s$ panel.

γ_{zx} would vanish over the entire arc length. Also the Kirchhoff-Love shell theory presented in Section 3.3.6 would predict $\gamma_{zx}^{o} = 0$ over the entire arc length. The shear strain γ_{zx}^{o} is zero because the rotation ψ_x must vanish over the entire arc length to satisfy the hypotheses of the Kirchhoff-Love theory for this problem, and not because $D_{26} = 0$.

It is interesting to compare the predictions of the shear deformation theory, designated SDT_1, with the Kirchhoff-Love theory, designated KLT. This is done in Table 3 where various response measures are computed from the two theories at pressures of 10 psi and 100 psi for 4-, 8-, and 16-ply laminates. The table also presents results from a second shear deformation theory, designated SDT_2, which was obtained from SDT_1 by setting $D_{26} = 0$. Although setting $D_{26} = 0$ appears arbitrary, and is unnecessary in this analysis, setting $D_{26} = 0$ must be done in more complicated two-dimensional laminated plate and shell analyses to make mathematical solutions tractable. For example Wang (Ref. 20) has shown the separation of variables technique does not work in solving the linear partial differential equations for laminated plates when D_{16} and D_{26} are nonzero. Separation of variables will work when D_{16} and D_{26} vanish in such problems (specially orthotropic plates, for instance). Since it is a relatively simple matter to set D_{26} equal to zero in SDT_1 to obtain SDT_2, this is done there to see the effect.

Comparing the Kirchhoff-Love theory (KLT) to the first shear deformation theory (SDT_1) for the laminates and pressures presented in Table 3 the following statements may be made: The center deflection w_c

Table 3. Effect of Shearing Deformations on Panel Center and Edge Response Quantities

Laminate and Pressure	Aralysis	w_c, in.	ϵ_θ^0, $\dfrac{\mu in.}{in.}$	$(\Gamma_\theta)_e$	$\dfrac{(\tau_{\theta z}^0)_e}{p}$	$\dfrac{(\tau_{xz}^0)_e}{p}$
$[\pm 45]_s$ $p=10ps\dot{\imath}$	SDT_1	0.1303	2097.	$-.5207$	-165.1	34.69
	SDT_2	.1303	2097.	$-.5001$	-142.2	-46.79
	KLT	.1303	2097.	$-.5049$	-144.8	-47.65
$[\pm 45]_s$ $p=100psi$	SDT_1	.3924	1066.	-3.453	-226.2	47.55
	SDT_2	.3924	1066.	-3.208	-194.8	-64.14
	KLT	.3921	1065.	-3.356	-212.8	-70.04
$[\pm 45]_{2s}$ $p=10psi$	SDT_1	.08722	1197.	$-.1366$	-63.5	5.31
	$S\cap T_2$	.08722	1197.	$-.1356$	-62.0	-10.20
	KLT	.08721	1196.	$-.1364$	-62.7	-10.31
$[\pm 45]_{2s}$ $p=100psi$	SDT_1	.2874	6449.	$-.9653$	-96.5	8.40
	SDT_2	.2874	6449.	$-.9524$	-93.7	-15.43
	KLT	.2871	6443.	$-.9803$	-99.0	-16.30
$[\pm 45]_{4s}$ $p=10psi$	SDT_1	.0532	608.	$-.0385$	-30.7	1.28
	SDT_2	.0532	608.	$-.0385$	-30.5	-2.51
	KLT	.0532	608.	$-.0387$	-30.7	-2.53
$[\pm 45]_{4s}$ $p=100psi$	SDT_1	.2033	3699.	$-.2791$	-45.2	1.88
	SDT_2	.2033	3699.	$-.2\urcorner83$	-44.9	-3.69
	KLT	.2030	3693.	$-.2837$	-46.4	-3.81

for SDT_1 is greater than w_c for KLT. Circumferential middle surface strains ε_θ^o are about the same for each theory. Differences of less than 10 percent occur for the edge rotation gradient Γ_θ between the two theories, but one theory does not consistently predict larger magnitudes for Γ_θ with respect to the other theory. The rotation gradient Γ_θ is directly proportional to the circumferential bending strain. Differences in the shear stress $\tau_{\theta z}^o$ computed on the middle surface at the edge are less than 20 percent for the two theories. Again one theory does not consistently predict a larger magnitude for $\tau_{\theta z}^o$ with respect to the other theory. There are large discrepancies in the values of shear stress τ_{xz}^o computed at the edge of the middle surface. First, there is a sign difference in τ_{xz}^o with KLT predicting negative values, and SDT_1 predicting positive values. Second, the magnitudes of τ_{xz}^o from KLT are greater than the magnitudes of τ_{xz}^o from SDT_1. These large discrepancies in τ_{xz}^o are a consequence of neglecting the rotation ψ_x in Kirchhoff-Love theory. The differences are largest for the thinnest panels.

The effect of neglecting D_{26} can be examined by comparing the two shear deformation theories SDT_1 and SDT_2 in Table 3. Both theories predict essentially the same center deflection w_c and circumferential middle surface strain ε_θ^o. Values of the edge rotation gradient Γ_θ differ between the two theories, SDT_1 predicts larger values than SDT_2. The shear stress $\tau_{\theta z}^o$ on the middle surface at the edge has a consistently smaller magnitude in SDT_2 with respect to SDT_1. However, the shear stress τ_{xz}^o at the edge of the middle surface has a

consistently larger magnitude in SDT_2 with respect to SDT_1. What appears to be more important, though, is that SDT_1 predicts positive values of τ_{xz}^o whereas SDT_2 (like KLT) predicts negative values of τ_{xz}^o.

The comparisons between the three theories given above do not establish the correctness of any one over the others. If an exact non-linear elasticity solution were available to compare to, then a conclusive statement on which theory is best may be made. No exact elasticity solution is available to compare with the three theories, however. Since the first shear deformation theory is less restrictive in its assumptions relative to the other two theories, it is assumed to be the best of the three. In Chapter 5 the theory used to compare to experiment is SDT_1 which will be referred to as the shear deformation theory. In the following section of this chapter further comparisons of the three theories are made to illustrate differences in the predicted distributions of σ_z, $\tau_{\theta z}$, and τ_{xz} through-the-thickness of the laminate.

4.7 Through-the-Thickness Stresses

In this section the through-the-thickness stress components $\tau_{\theta z}$, τ_{xz}, and σ_z are examined in more detail. The interlaminar stresses at the panel middle surface (z=0) and along the circumferential arc from the center to the edge of a panel are shown in Figure 26 for [±45] symmetric laminates of 4 and 16 plies. These stresses are calculated at an applied internal pressure of 100 psi and are normalized by this
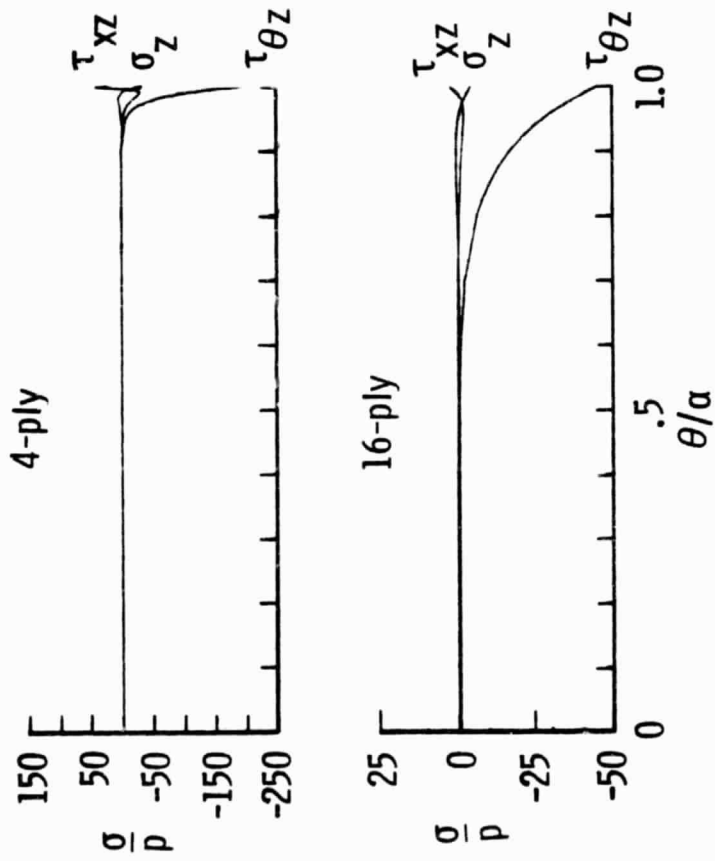
Figure 26.- Circumferential distribution of normalized interlaminar stresses at middle surface of 4- and 16-ply [±45] symmetric panels with 100 psi internal pressure. Results calculated with SDT$_1$ theory.

applied pressure. For the 4-ply panel the interlaminar stresses are nearly zero over most of the arc length except for a small distance near the edge. For the 16-ply panel the interlaminar stresses are uniform for about one-half of the distance to the edge. The shear stresses $\tau_{\theta z}^{o}$ and τ_{xz}^{o} are zero at the center with the shear stress $\tau_{\theta z}^{o}$ increasing monotonically toward the edge. The slope of the τ_{xz}^{o} shear stress distribution changes sign near the edge. The normal stress σ_{z}^{o} is compressive except in a small region a short distance away from the panel's edge where it is tensile. The maximum values of all inter-laminar stresses occur at the edges of the panel, and the maximum values are larger for the thinner panels than for the thicker panels. Also, at the panel edges, the magnitude of the shear stress $\tau_{\theta z}^{o}$ is greater than the shear stress τ_{xz}^{o} which, in turn, is greater than the normal stress σ_{z}^{o}. The severe interlaminar stress gradients shown in Figure 26 occur near the panel edges as a consequence of the severe bending strain gradient shown in Figure 18. The interlaminar stresses are proportional to the bending strain gradient as shown in equations (3.96) to (3.98).

The results shown in Figure 26 are obtained from the first shear deformation theory (SDT$_1$) which includes the effects of the twist coupling coefficient D_{26}. In Figures 27 and 28 these interlaminar stresses are also computed from Kirchhoff-Love theory (KLT) and the second shear deformation theory (SDT$_2$), and plotted for comparison with SDT$_1$. In Figure 27 the results plotted are for a 4-ply [±45] symmetric laminate at 100 psi, and in Figure 28 the results are plotted for a 16-ply [±45] symmetric laminate at 100 psi. The distributions are
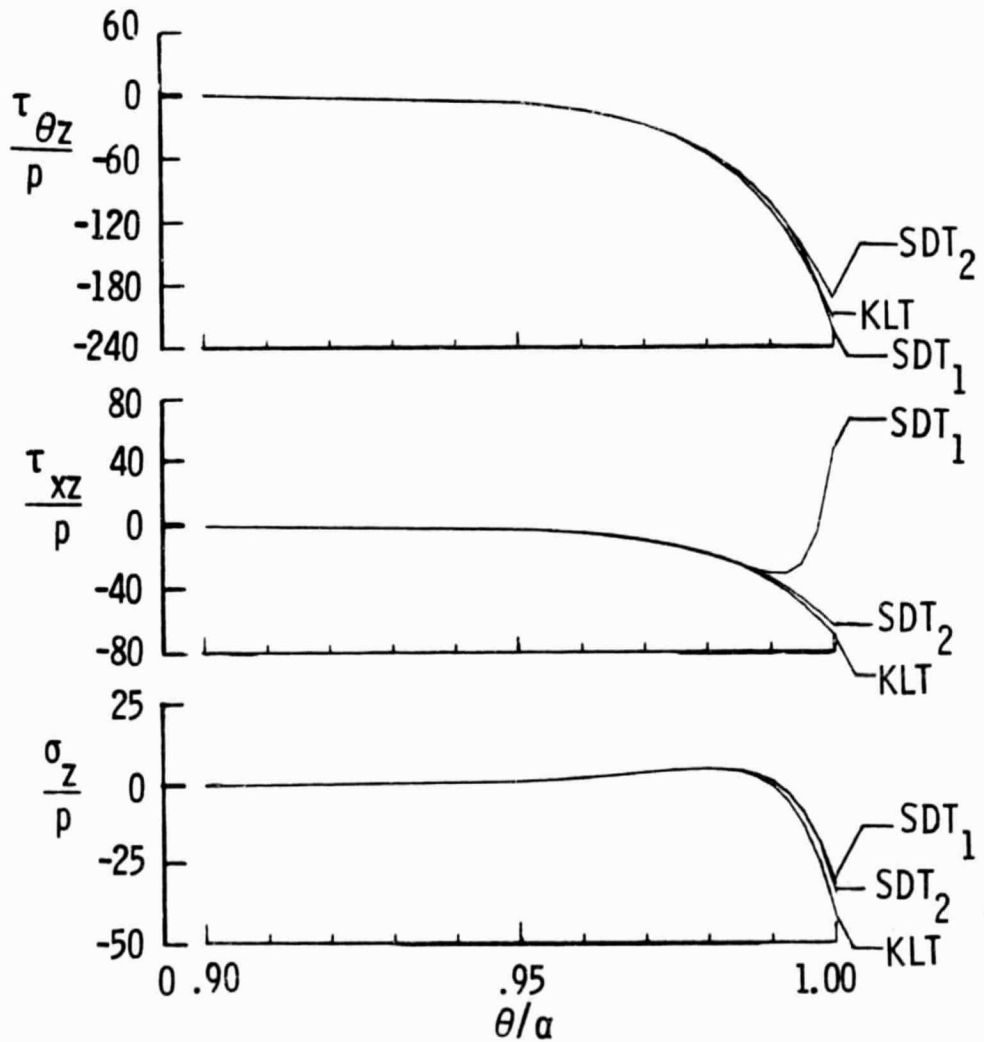
Figure 27.- Circumferential distribution of normalized interlaminar
stresses calculated at the middle surface of a 4-ply [±45]
panel with 100 psi internal pressure. Results calculated
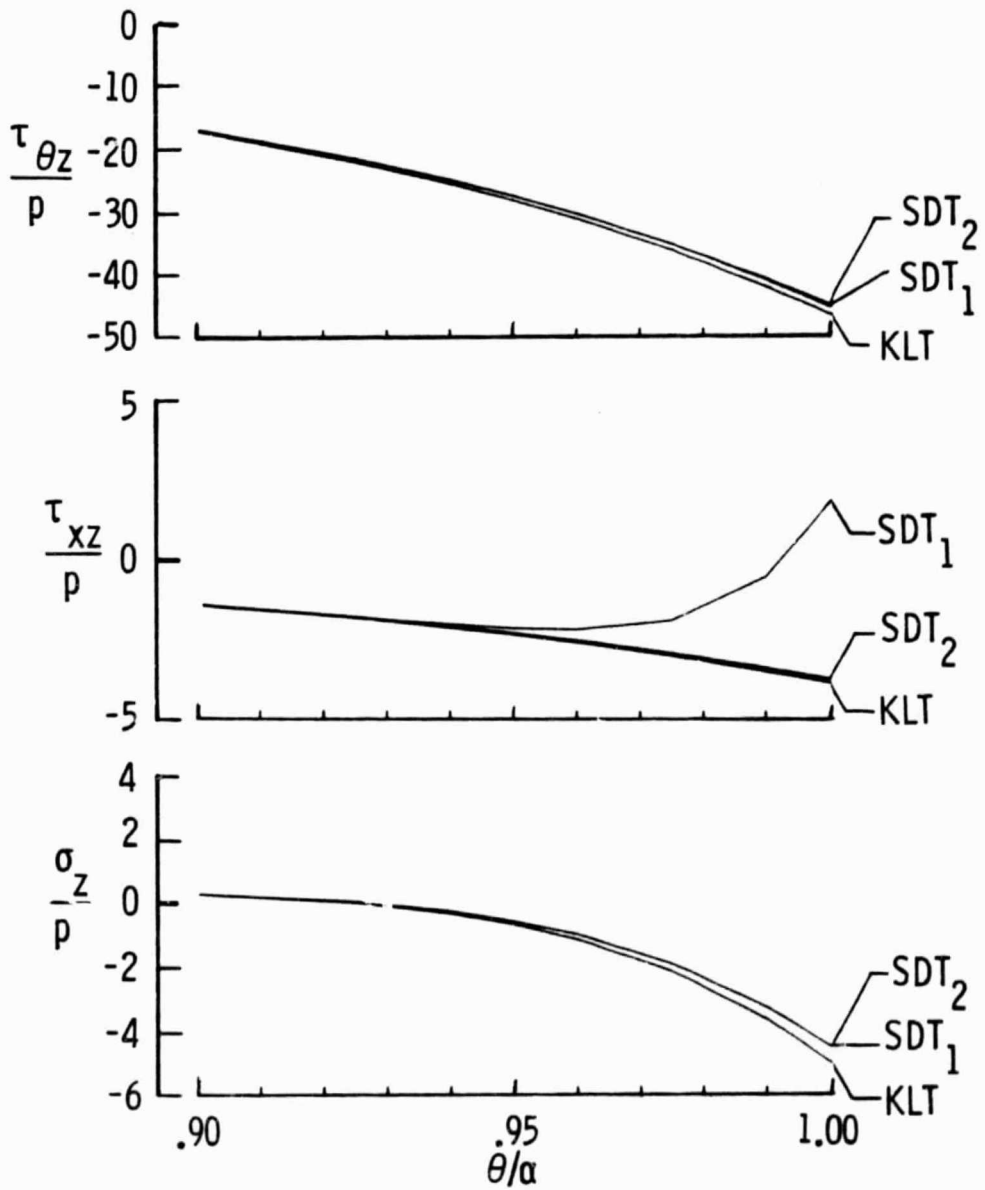with KLT, SDT_1, and SDT_2 theories.

Figure 28.- Circumferential distribution of normalized interlaminar
stresses calculated at the middle surface of a 16-ply
$[\pm 45]_{4s}$ panel with 100 psi internal pressure. Results
calculated with KLT, SDT_1, and SDT_2 theories.

only plotted near the edges ($\theta/\alpha = 0.90-1.0$). For both laminates the largest differences occur at the edge with no differences occurring away from the edge. The most pronounced difference between the three theories occurs for the interlaminar stress τ_{xz}^o. In the mathematical solution the roots $\pm\bar{\lambda}_2$ given by equation (3.48) are responsible for these differences. These roots are associated with the rotation ψ_x and the twist coupling coefficient D_{26}. The differences in the stresses $\tau_{\theta z}^o$ and σ_z^o between the theories are greatest at the edge but small in magnitude. Through-the-thickness shear and twist coupling effects extend over a greater distance from the edge for the 16-ply panel.

The boundary layer decay lengths from shear deformation theory (SDT_1) are associated with roots λ_1 and λ_2 of equation (3.48), and are given in Table 4 for 4-, 8-, and 16-ply [±45] symmetric laminates. These decay lengths are calculated with equation (3.68) after evaluating the roots with equation (3.48). The value of the root λ_2 is an order of magnitude larger than the root λ_1 for the pressures examined. The root λ_1 is numerically close to the root λ (eq. (3.81)) of the Kirchhoff-Love theory and both λ_1 and λ increase with pressure and their corresponding boundary decay length decreases with pressure. For the internal pressures loads which caused small strains in the panels, the boundary decay length associated with λ_2 is much shorter than the decay length of λ_1. In addition, the boundary decay length associated with λ_2 remains approximately constant with pressure. Both boundary decay lengths increase with increases in laminate thickness.

Table 4. Boundary Decay Lengths ξ_1^* and ξ_2^* of 4-, 8- and 16-ply
$[\pm 45°]_{ns}$ Laminates with Internal Pressures of 10 and 100 psi

Laminate	p, psi	ξ_1^*, in.	ξ_2^*, in.
$[\pm 45]_s$	10	0.6223	0.0586
	100	0.2730	0.0582
$[\pm 45]_{2s}$	10	1.638	0.1372
	100	0.722	0.1369
$[\pm 45]_{4s}$	10	4.582	0.2534
	100	1.883	0.2833

The distributions of stress components σ_z, $\tau_{\theta z}$, and τ_{xz} through the thickness are shown in Figure 29 for the [$\pm$45] symmetric laminates of 4 and 16 plies. These results are calculated at the clamped edge using SDT_1. The through-the-thickness shear stresses are symmetric about the middle surface and the normal stress is nonsymmetric. The shear stress $\tau_{\theta z}$ is the largest in magnitude relative to τ_{xz} and σ_z and attains a maximum magnitude at the middle surface. The shear stress $\tau_{\theta z}$ is a maximum at the clamped edge of the middle surface. The maximum values of the stresses τ_{xz} and σ_z occur at locations other than the middle surface.

The influence of the twist coupling coefficient D_{26} on the through-the-thickness distributions of stress σ_z, $\tau_{\theta z}$, and τ_{xz} is shown in Figures 30 and 31 for the same 4-ply and 16-ply [$\pm$45] symmetric laminates. The twist coupling coefficient has the largest influence on the shearing deformation stress τ_{xz}. The shear deformation theory (SDT_1) predicts the largest value of the stress $\tau_{\theta z}$ in Figure 30(a) for the 4-ply panel whereas the Kirchhoff-Love theory predicts the largest value in Figure 31(a) for the 16-ply panel. Therefore, as pointed out previously, the Kirchhoff-Love theory does not, in general, give conservative solutions.

In this paragraph through-the-thickness stresses of two quasi-isotropic 8-ply symmetric laminates and one [$\pm$45] 8-ply symmetric laminate are compared. The through-the thickness distribution of σ_z, $\tau_{\theta z}$, and τ_{xz} for three 8-ply laminates of different laminate stacking sequences are shown in Figure 32. These distributions are
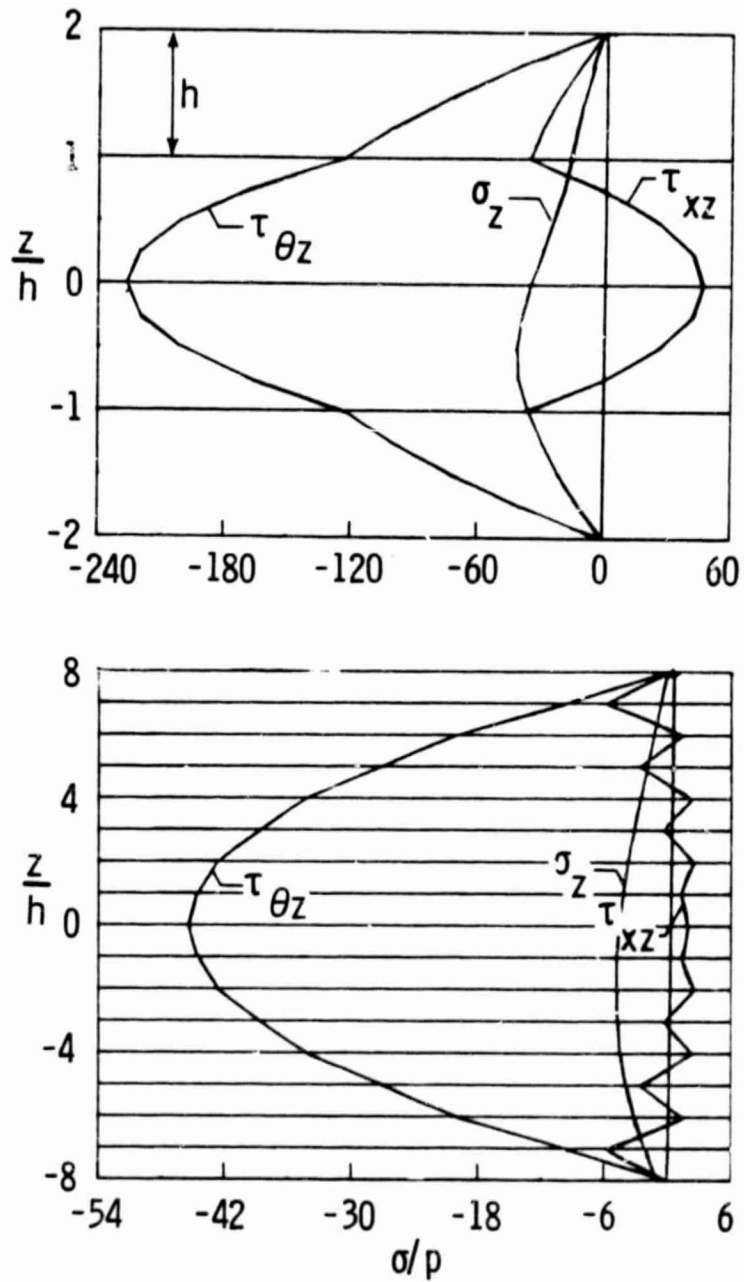
Figure 29.- Through-the-thickness distribution of normalized
interlaminar stresses at clamped edge of 4- and 16-ply [±45]
symmetric panels with 100 psi internal pressure. Results
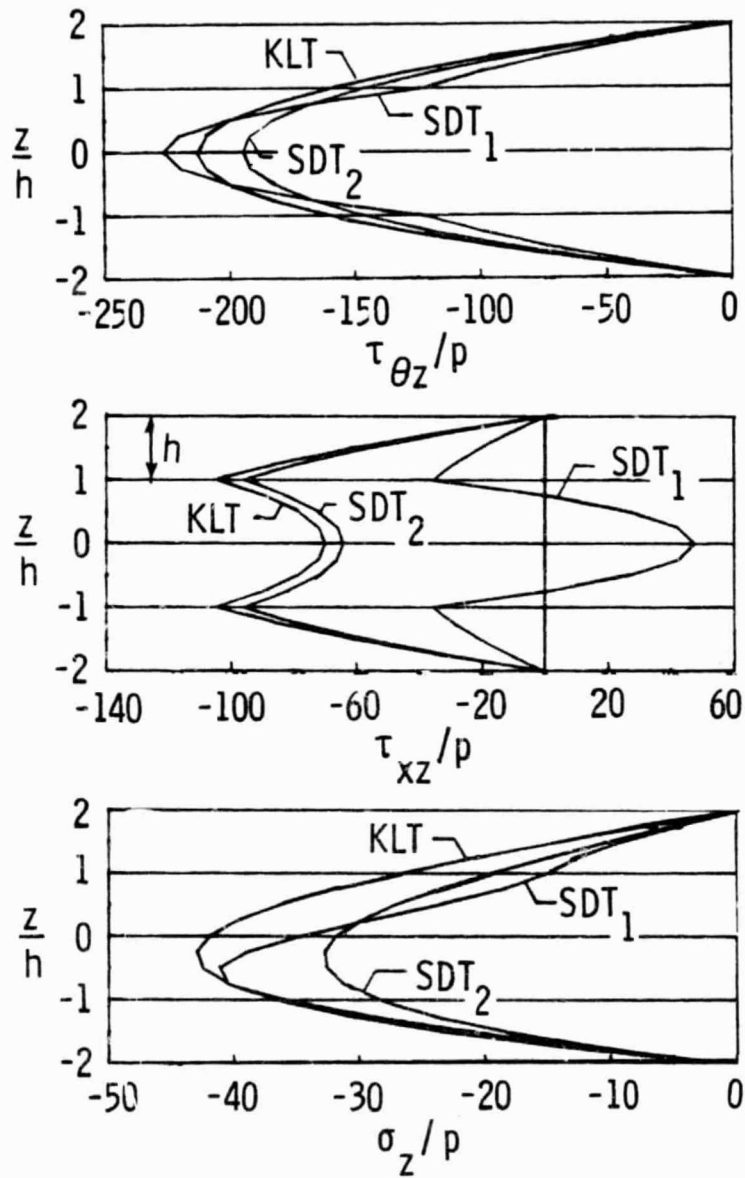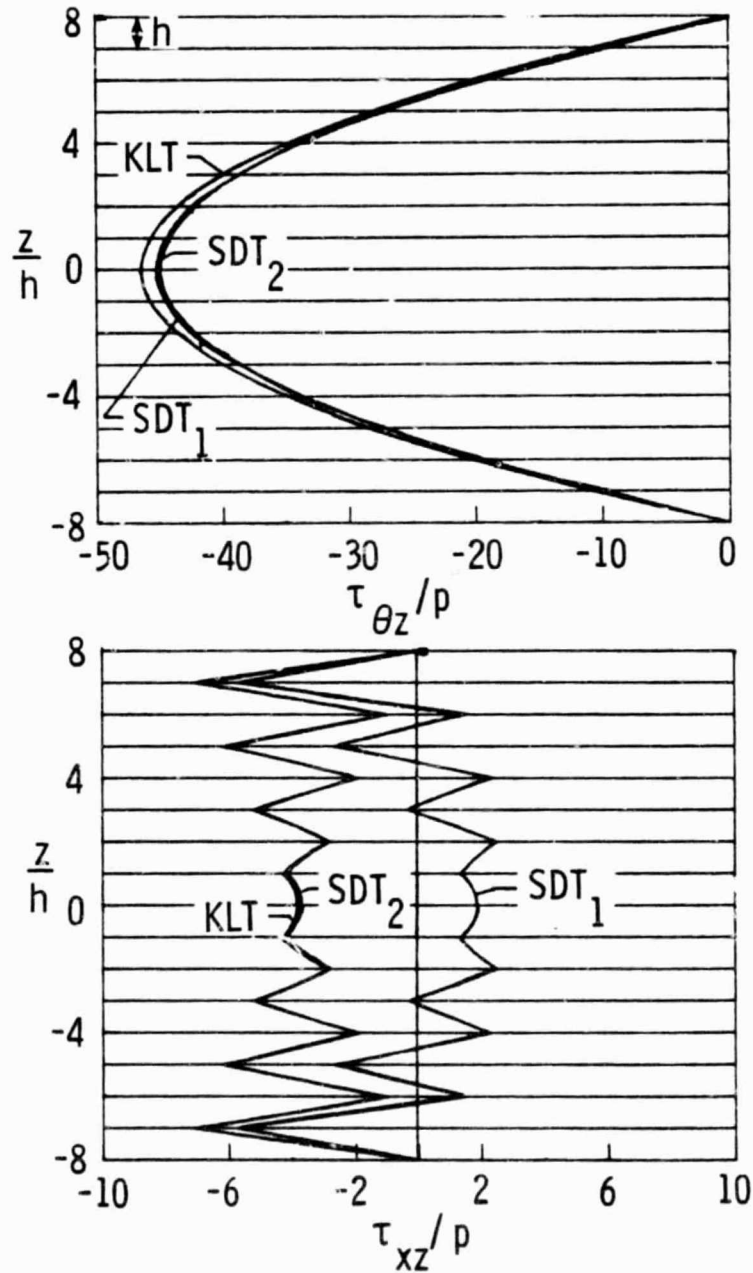calculated with SDT$_1$ theory.

113

Figure 30.– Through-the-thickness distribution of normalized interlaminar stresses at clamped edge of a 4-ply $[\pm45]_s$ panel with 100 psi internal pressure. Results calculated with KLT, SDT_1, and SDT_2 theories.
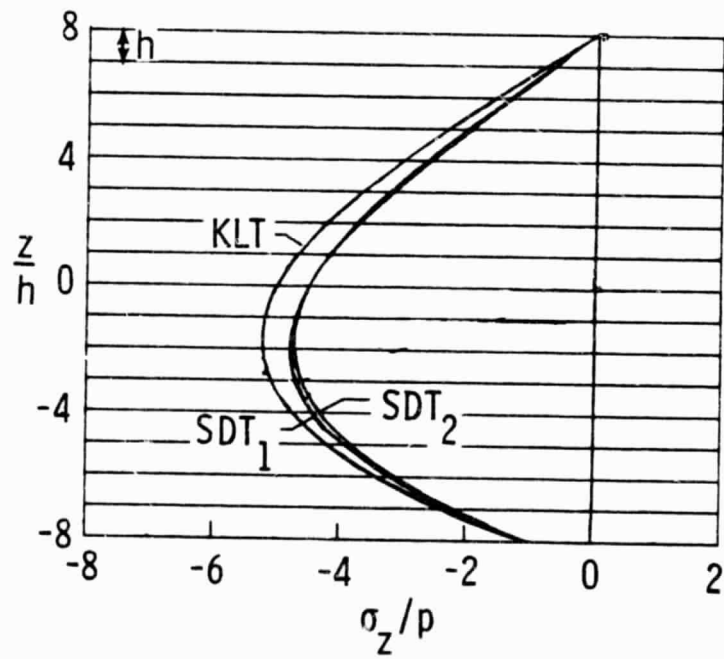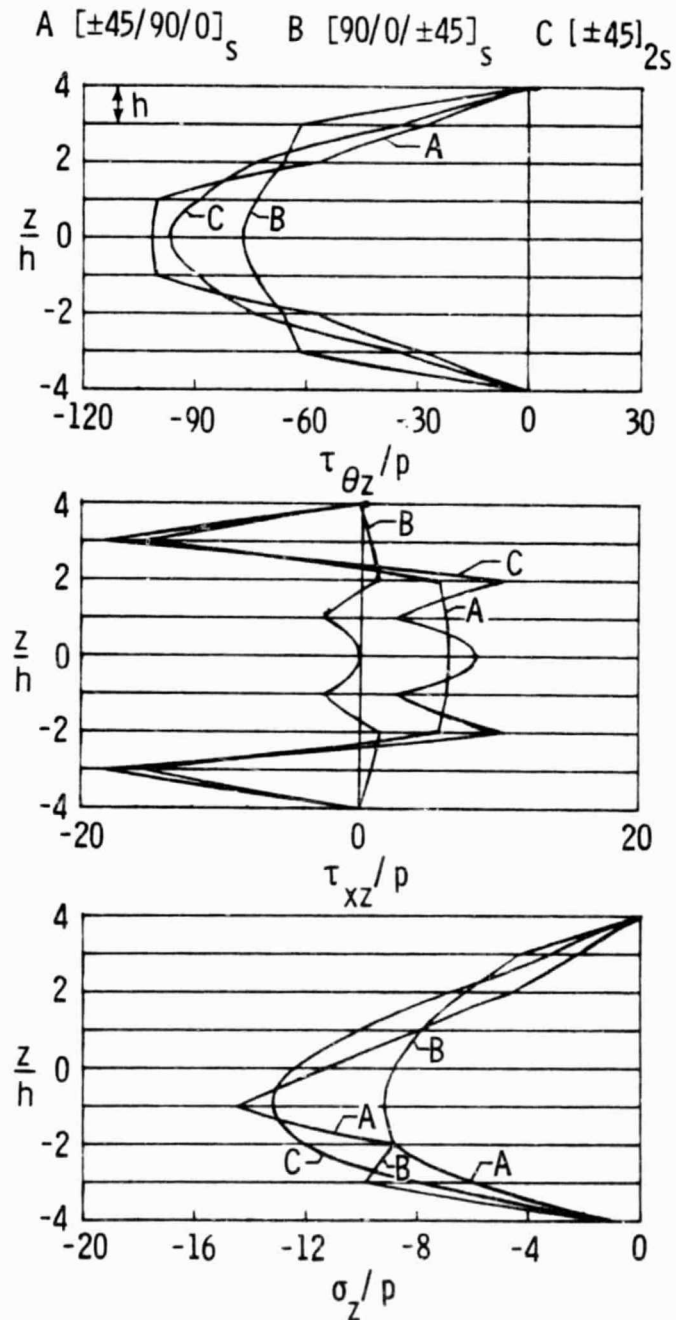
114

Figure 31.– Through-the-thickness distribution of normalized
interlaminar stresses at clamped edge of a 16-ply $[\pm 45]_{4s}$
panel with 100 psi internal pressure. Results
calculated with KLT, SDT_1, and SDT_2 theories.

Figure 31.- Concluded.

Figure 32.— Through-the-thickness distribution of normalized
interlaminar stresses at clamped edges of three different 8-
ply panels with 100 psi internal pressure. Results
calculated with SDT_1 theory.

calculated at the clamped edge using the shear deformation theory (SDT_1). The laminate stacking sequence has a large influence on all through-the-thickness stresses. The largest change in slope of the shear stresses τ_{xz} and $\tau_{\theta z}$ occurs at the interface of $\pm 45°$ plies. The largest slope changes for the normal stress (σ_z) distributions occur at the interface of the 90° ply and 0° ply on the concave side of the middle surface.

Chapter 5

COMPARISON OF ANALYSIS AND EXPERIMENT

To correlate the analysis with the experiment, it was found necessary to measure the initial shape of the panel after fitting it into the test fixture, and to measure the slipping of the panel out of the test fixture with increasing pressure. Using the measured initial geometry and the measured pressure-slip characteristics in the analytical model, the comparisons presented in this chapter establish that the analysis can predict reasonably well the experimental response data. With confidence established in the analytical model of the experiment, it is reasonable to use the stresses and strains predicted in the analytical model to analyze failure, which is the subject of Chapter 6.

Results of thirteen test specimens are given in Table 1. Most of the comparisons between analysis and experiment are carried-out on specimens G2, G4, G7, G9, and G10 listed in Table 1, because only these panels were surveyed prior to pressurization to determine their actual shape after fitting into the test fixture. The other panels were tested before it was determined that the initial shape deviated substantially from a nominal 60-inch radius cylindrical panel. Thus, comparison of analysis and experiment is presented only for the panels in which the actual shape was determined and used in the analysis. In particular, the comparisons are presented for the 4-ply (G2), 8-ply (G7), and 16-ply (G10) panels. No comparisons are presented for the 5-ply (G4) and 16-ply (G9) panels, since these results are similar to those presented for specimens G2, G7, and G10.

118

5.1 Measurements Required for the Analysis

5.1.1 Panel Stiffnesses

Some of the elastic stiffnesses utilized in the analysis were
verified by actual testing. Tensile coupons were cut from flat panels
of the same material and cured under the same conditions as the 5-ply
specimens G3 and G4 and the 8-ply quasi-isotropic specimens G5, G6, and
G7. These panels were tested in tension to failure. The specimen
elastic stiffnesses were measured and compared to their values computed
from classical lamination theory using the lamina properties given in
Section 2.1 for T300-5208 and the average lamina thickness measured from
the coupons. The experimentally determined extensional stiffnesses of
the 5-ply specimens (G3 and G4) were 97,900 lb/in. and 164,200 lb/in.
The theoretically predicted stiffnesses are 103,500 lb/in. and
167,000 lb/in., respectively. The experimentally determined extensional
stiffness of the quasi-isotropic 8-ply specimens (G5, G6, and G7) was
325,000 lb/in. and the theoretical stiffness was 321,500 lb/in. The
experimental and theoretical stiffnesses agree very well and suggest
that the use of lamination theory with the elastic properties for
T300-5208 given in Section 2.1 is sufficient for predicting the elastic
stiffnesses of the specimens. The computed stiffnesses used in the
analysis for panels G2, G4, G7, G9, and G10 are given in Table 5. The
average lamina thicknesses used in computing the stiffnesses are also
given in Table 5 for each panel.

Table 5. Laminate Thicknesses and Elastic Stiffnesses Used in Correlation of Analysis and Experiment for Specimens G2, G4, G7, G9, and G10. All Laminates Are Symmetric and the Coupling Stiffnesses B_{ij} = 0.

Specimen	Thickness, in.	A_{44}, lb/in.	A_{55}, lb/in.	A_{ij}, lb/in.	D_{ij}, lb-in.
G2	0.0212	16218.	16218.	$\begin{bmatrix} 133770. & 100340. & 0. \\ & 139770. & 0. \\ \text{sym.} & & 104610. \end{bmatrix}$	$\begin{bmatrix} 5.2349 & 3.7580 & 2.5844 \\ & 5.2349 & 2.5844 \\ \text{sym.} & & 3.9179 \end{bmatrix}$
G4	0.0261	19105.	20828.	$\begin{bmatrix} 147670. & 102630. & 0. \\ & 238290. & 0. \\ \text{sym.} & & 107880. \end{bmatrix}$	$\begin{bmatrix} 9.7129 & 6.9650 & 3.7037 \\ & 9.9187 & 3.7037 \\ \text{sym.} & & 7.2633 \end{bmatrix}$
G7	0.0424	32436.	32436.	$\begin{bmatrix} 364430. & 115790. & 0. \\ & 364430. & 0. \\ \text{sym.} & & 124320. \end{bmatrix}$	$\begin{bmatrix} 48.629 & 7.8080 & 2.5844 \\ & 79.641 & 2.5844 \\ \text{sym.} & & 9.0869 \end{bmatrix}$
G9	0.0890	68054.	68054.	$\begin{bmatrix} 764620. & 242930. & 0. \\ & 764620. & 0. \\ \text{sym.} & & 260840. \end{bmatrix}$	$\begin{bmatrix} 239.85 & 138.19 & 23.870 \\ & 812.72 & 23.870 \\ \text{sym.} & & 150.00 \end{bmatrix}$
G10	0.0832	63648.	63648.	$\begin{bmatrix} 715110. & 227200. & 0. \\ & 715110. & 0. \\ \text{sym.} & & 243450. \end{bmatrix}$	$\begin{bmatrix} 301.39 & 203.13 & 29.290 \\ & 379.50 & 29.290 \\ \text{sym.} & & 212.79 \end{bmatrix}$

5.1.2   Initial Geometry

Shape surveys of unpressurized specimens clamped in the test
fixture were conducted to determine the actual initial geometry of the
specimens. The instrumentation and procedures used to conduct these
initial geometry surveys are described in Section 2.2. The results of
typical measurements to determine the shapes of circumferential ($x = 0$)
and axial ($\theta = 0$) lines passing through the center of specimen G7 are
shown in Figures 33 and 34, respectively. A circular arc with a radius
of 39.9 in. has the same rise and chord as the measured shape and is
shown in Figure 33 for comparison. Points on the measured curve fall
inside of the circular arc and the radius of the circular arc is 33 per-
cent smaller than the nominal 60 inch panel radius. The radius of the
circular arc was used in the analysis to approximate the effects of the
initial panel geometry. The same procedure was used to determine radii
of 33.4, 43.1, 53.4, and 50.3 inches for panels G2, G4, G9, and G10,
respectively. The shape of the measured axial line through the panel
center shown in Figure 34 differs from the nominal straight line genera-
tor of a cylindrical panel indicating that the initial shape of the
specimen is also curved in the axial direction. The curvature in the
axial direction was neglected in the analyses. These differences in
shape indicate that the initial geometry of the panel is distorted from
the nominal circular cylindrical panel shape.
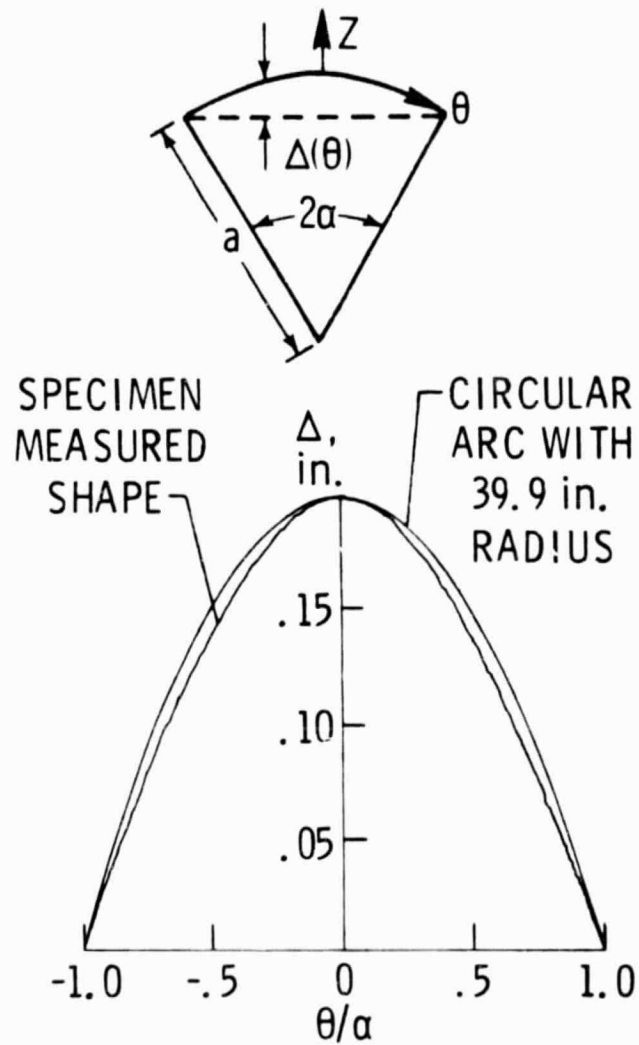
Figure 33.— Measured vertical shape along the circumferential center
line (x=0.) of specimen G7 before pressurization.
Appropriate circular shape used in analysis shown for
comparison.

ORIGINAL PAGE IS
OF POOR QUALITY
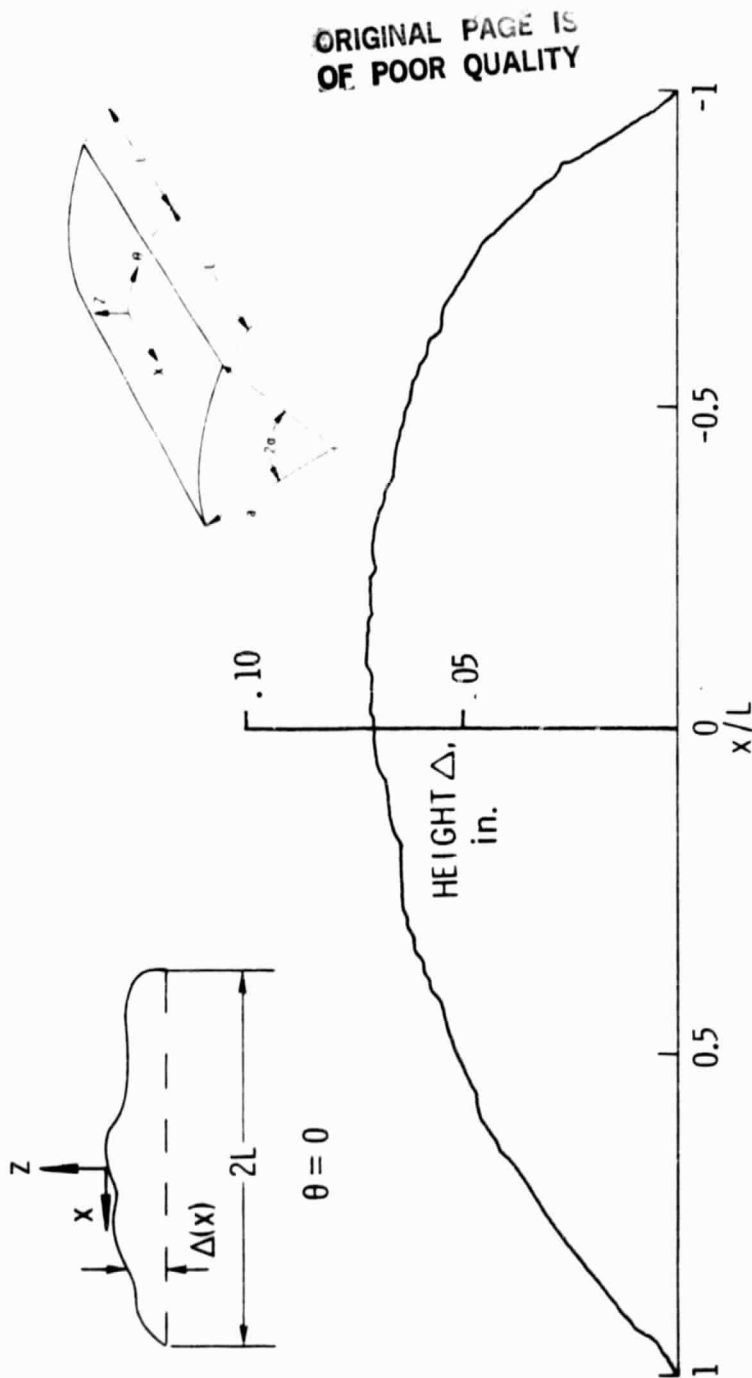
Figure 34.- Measured vertical shape along the axial center line ($\theta=0$.) of specimen G7 before pressurization.

5.1.3 Panel Slip

Applied internal pressure loading causes circumferential and axial tensile forces to be generated in a specimen. These tensile forces can cause the specimen to pull away or slip from the test fixture clamping mechanism and this slipping affects the response of the specimen.

In-plane circumferential displacements at the specimen edges were measured with direct-current differential transformers as the applied internal pressure was increased to determine the magnitude of displacements or slippage which occurred during testing. Results of typical in-plane circumferential displacement measurements at the midlength of a straight edge of specimen G7 are shown in Figure 35. The pressure-displacement curve in Figure 35 is approximately bilinear up to failure. Circumferential displacement values from these pressure-displacement curves were used as prescribed values for $\bar{v}$ (eq. (3.37)) in the one-dimensional panel analysis to approximate the effects of in-plane circumferential edge displacements on panel response. Rotations at the clamped edges also occur, but were difficult to measure for inclusion into the analysis.

The two-dimensional STAGS analysis results shown in Figure 10 indicate that the axial strains are zero at the center of an ideal panel with perfectly clamped edges. However, in the experiment back-to-back axial strain gages located at the center of the specimens indicate that tensile axial membrane strains are nonzero. The axial strain curves for specimen G7 are shown in Figure 36. The 4-, 5-, and 8-ply specimens
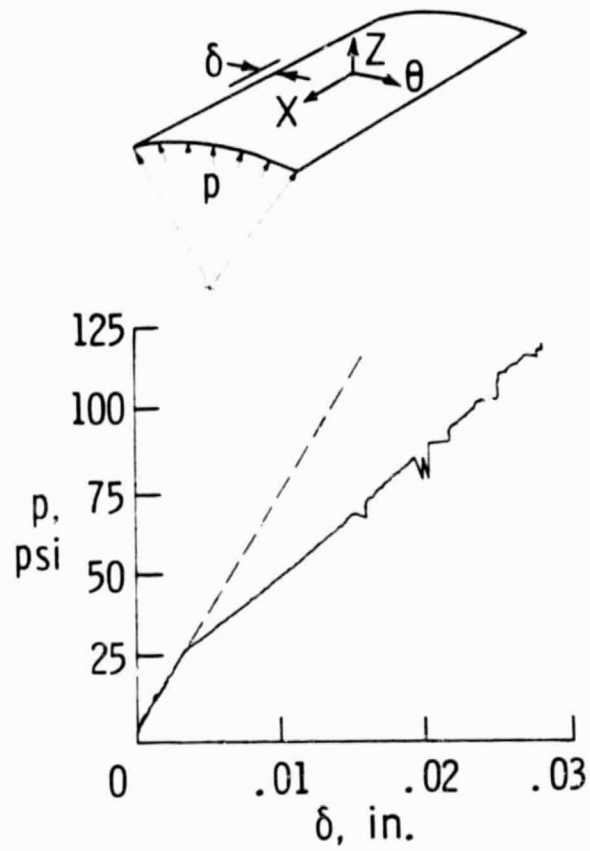
Figure 35.- Measured circumferential edge displacements u₁ ed in analysis
of panel G7.
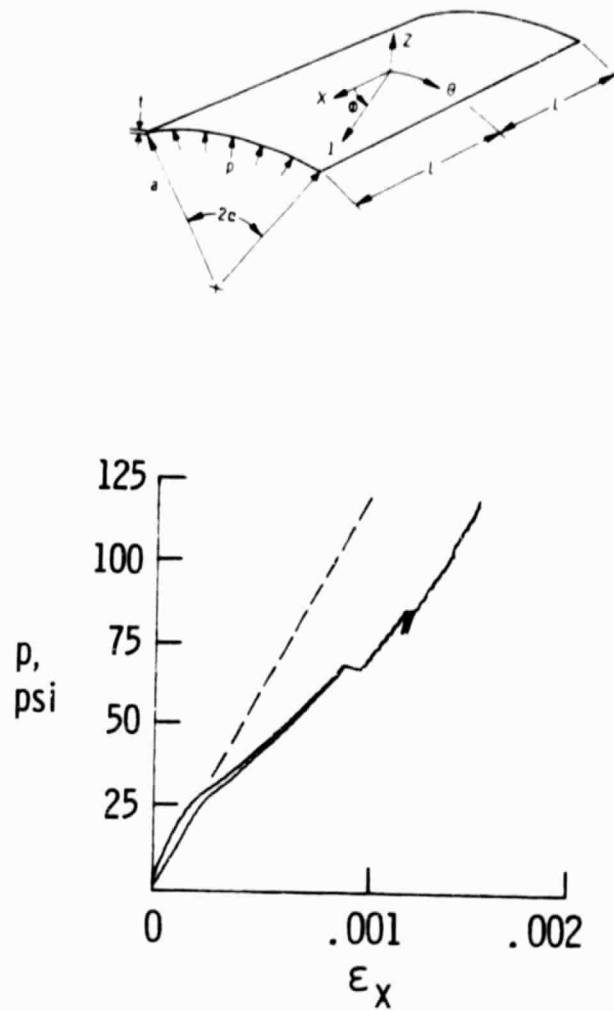
Figure 36.- Axial strain response of back-to-back gages located at center of specimen G7 and used in analysis.

tested in this study had nonzero axial membrane strains at the specimen
center. The stiffer 16-ply specimens had both nonzero axial membrane
and bending strains at the specimen center. The nonzero axial membrane
strains are a result of the two-dimensional effects associated with
pillowing and the inability of the test fixture clamping mechanism to
prevent the specimen from slipping axially at the straight edges of the
panels. In the one-dimensional analysis, the assumed axial boundary
displacements of equation (3.25) are directly responsible for the
uniform axial strain state of equation (3.29). Although the axial
boundary slip was never measured, axial slip probably occurred simul-
taneously with the measured circumferential slip. This assumption is
substantiated by comparing Figures 35 and 36 which exhibit a change in
slope at essentially the same pressure (27.6 psi) for specimen G7.
Therefore, the two-dimensional axial strain effects, caused by slipping,
are modeled as an applied axial strain $\bar{\varepsilon}$ in equation (3.65) of the
one-dimensional analysis.

5.2 Comparison of Analysis and Experiment

5.2.1 Center Deflection Versus Pressure

The effects of increasing internal pressure p on the nondimen-
sionalized radial deflections at the center w_c are shown in Figure 37
for the 4-, 8-, and 16-ply panels (specimens G2, G7, and G10, respec-
tively). The radial deflection is nondimensionalized by the panel
thickness. The solid curves in the figure represent results from the
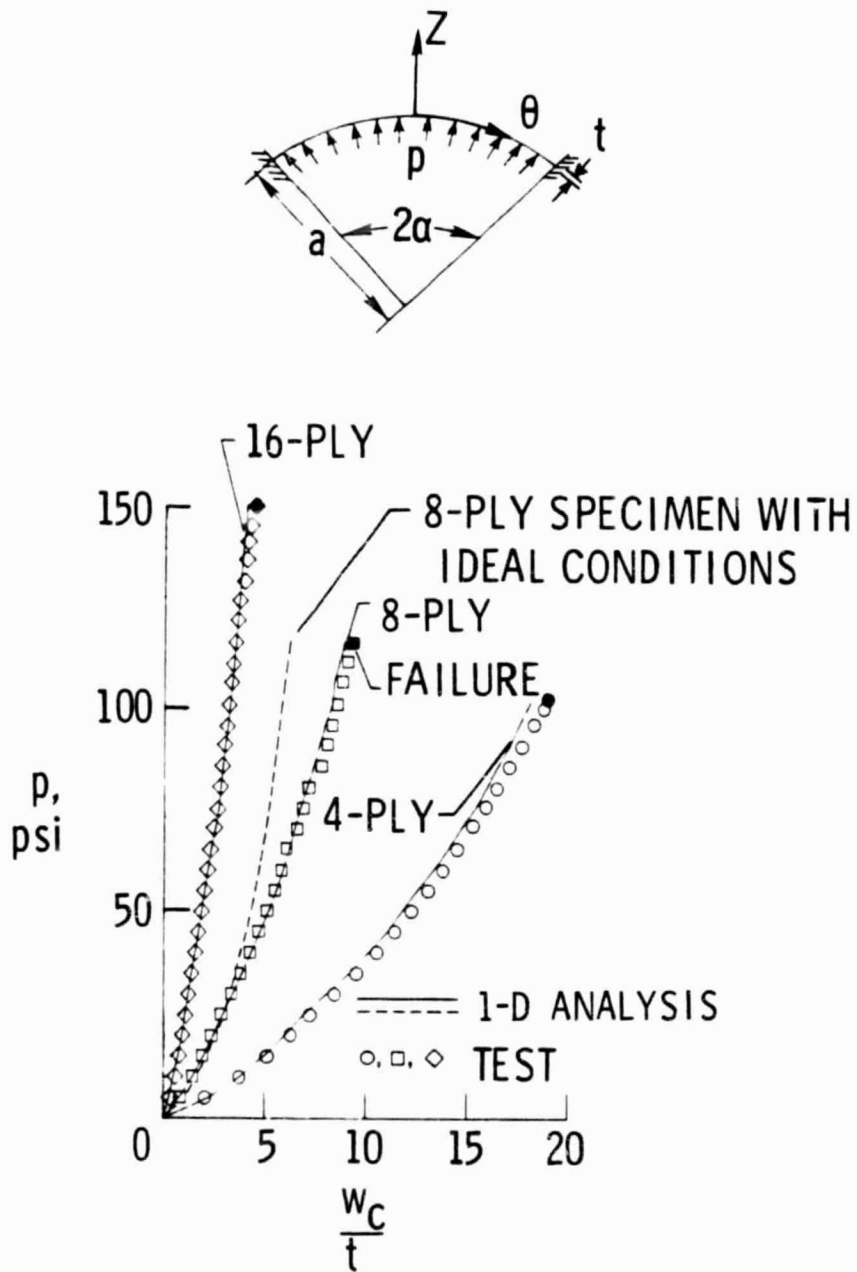
Figure 37.- Experimental and analytical radial deflection response at centers of specimens G2, G7 and G10.

one-dimensional panel analysis and the symbols represent experimental
data. The filled symbols represent specimen failure. The effects of
the initial measured radius (e.g., Fig. 33), the measured in-plane
circumferential edge displacements (e.g., Fig. 35) and measured axial
strains at the panel center (e.g., Fig. 36) are included in the analysis
of each panel. Analytical results for the 8-ply panel (G7) that do not
include the effects of measured initial radius, in-plane circumferential
edge displacements and axial strain at panel center are shown in
Figure 37 by the dashed curve. Comparing the results of the analysis
for the 8-ply panel with the experimental results indicates that the
effects of initial geometry and panel slip must be included in the
analysis for accurate correlation with experimental results. The non-
linear character of the global pressure-displacement responses in
Figure 37 is indicated by the large radial deflections relative to the
panel thicknesses and the increases in the slopes of the pressure-
displacement curves, or stiffening, as internal pressure increases.
These analytical results correlate well with the corresponding experi-
mental results up to failure.

5.2.2 Membrane Strain Versus Pressure

Circumferential membrane strains at the centers of the typical 4-,
8-, and 16-ply panels (specimens G2, G7, and G10, respectively) as a
function of internal pressure are shown in Figure 38. The solid curves
represent the analytical results and the symbols represent the experi-
mental results. The filled symbols represent specimen failure.
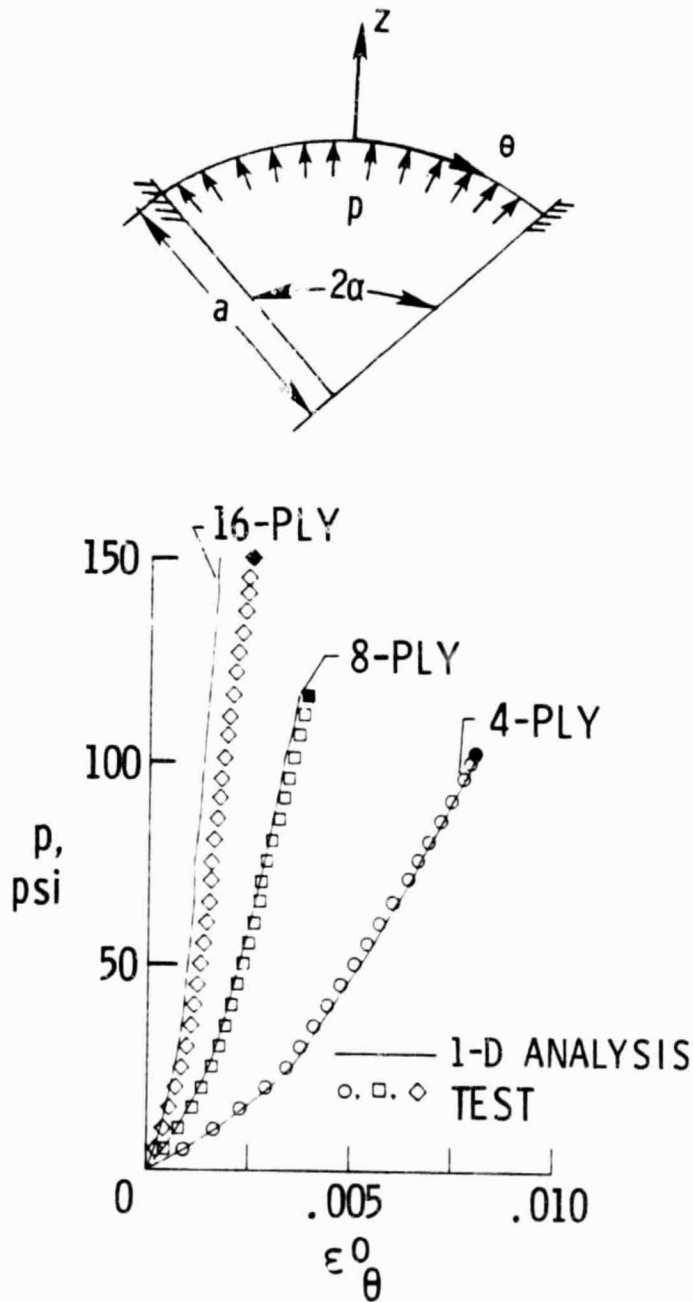
Figure 38.- Experimental and analytical circumferential membrane strain responses at center of specimens G2, G7 and G10.

These results indicate that the circumferential membrane strains at the panel center are larger at every pressure for the thinner panels than for the thicker panels, and that the analytical results for the two thinner panels correlate well with the experimental results up to failure. Although the analytical results for the 16-ply panel correlate reasonably well with the experimental results for the lower values of applied internal pressure, the analytical and experimental results do not agree as well at the higher values of the internal pressure. The back-to-back axial strain gages at the center of the 16-ply panel indicate that negligible bending strains exist at the lower pressures, but the strain gage data show that both bending and membrane strains are significant at the higher pressures and increase as the pressure is increased. For the thinner panels the bending strains were negligible up to failure. Apparently, axial bending effects at the center are more important for the stiffer 16-ply panels than for the thinner panels and become more pronounced as the applied pressure is increased.

5.2.3 Circumferential Strain Distributions at a Fixed Pressure

Circumferential surface strain distributions at the panel midlength (x = 0, Fig. 1) are shown in Figure 39 for the typical 4-, 8-, and 16-ply panels (specimens G2, G7, and G10, respectively) discussed in the previous section. The distributions are shown for only half the panel due to symmetry and are for an applied internal pressure of 50 psi. Results from the one-dimensional panel analysis are represented by the solid curves and the experimental results are indicated by the symbols.

132
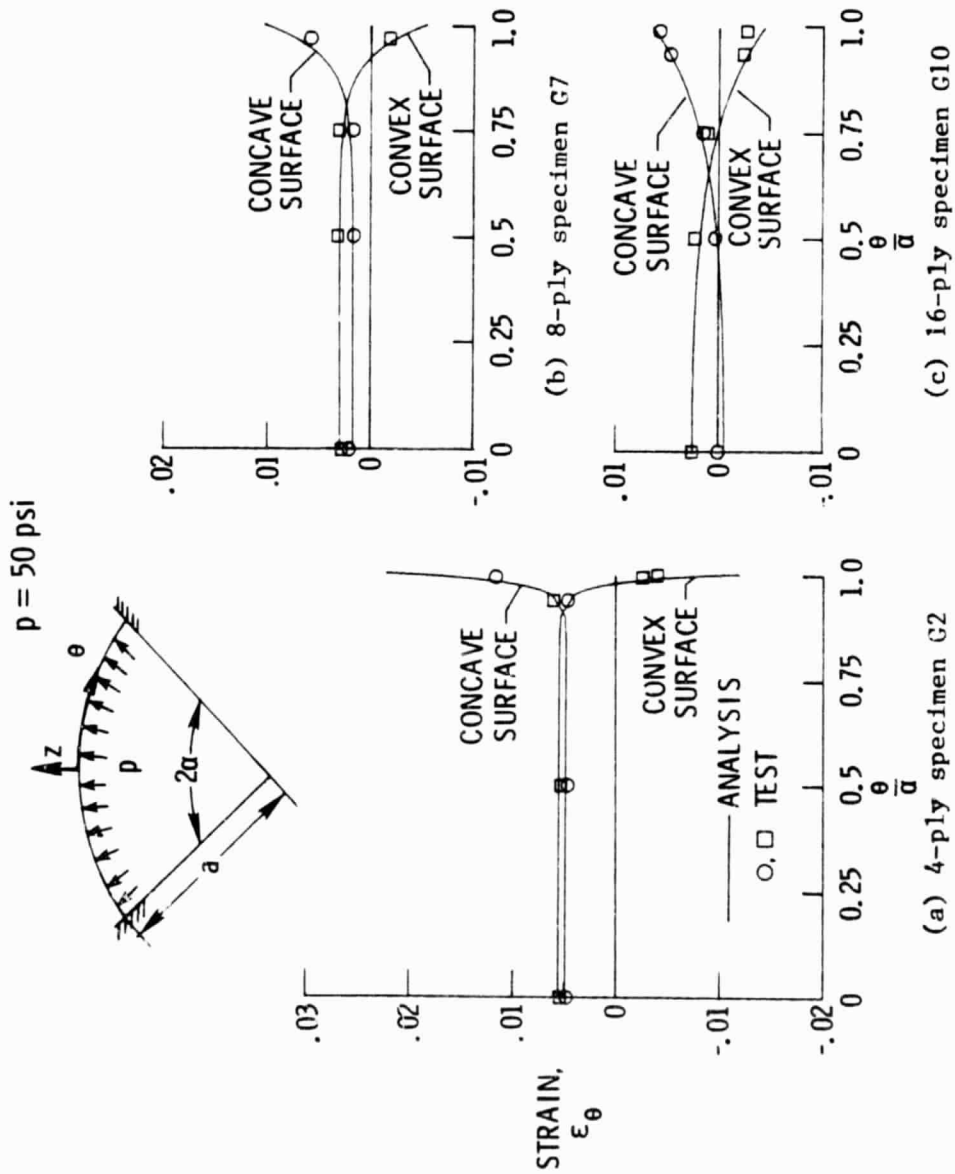
Figure 39.- Experimental and analytical circumferential surface strain distributions for an internal pressure of 50 psi.

Strain gage data for the concave surfaces are represented by the circular symbols and data for the convex surfaces are represented by the square symbols. These results indicate that the circumferential membrane strain found by averaging the two surface strains is nearly constant along the circumferential arc length for each panel as was predicted by the one-dimensional panel analysis. The surface strains are uniform near the center of the panels, but significant bending strains exist near the panel edges. These bending strains are maximum at the edges. The magnitudes of the bending strains are larger for the thinner panels than for the thicker panels, and the bending strain gradients are confined to a smaller edge region for the thinner panels. For example, the bending strain of the 4-ply panel G2 are distributed over approximately 10 percent of the circumferential arc length (see Fig. 39(a)), but are distributed over about 80 percent of the arc length of the 16-ply panel G10 (see Fig. 39(c)). The strains predicted by the analysis agree with the experimental strains and indicate the severity of the bending strain gradient near the panel edges. The magnitudes of the strains measured near the edges are smaller than those predicted by the analysis. These differences may be due to slight rotations of the specimens and clamping bars at the panel edges which relieve the bending strain. Also, differences may occur due to the difficulty of measuring strains in a region of severe bending gradient.

5.3   Prediction of Through-the-Thickness Stress Components for
       Specimens G2 and G10

The through-the-thickness stresses σ_z, τ_{xz}, and $\tau_{\theta z}$ were cal-
culated from the analyses of specimens G2 (4-ply) and G10 (16-ply) and
the results are presented in Figures 40 and 41 for an applied internal
pressure of 50 psi. The stresses shown in these figures are normalized
by this applied pressure. The distribution of interlaminar stresses
along the circumferential arc and at the panel middle surface for the
4-ply specimen G2 is shown in Figure 40(a) and those for the 16-ply
specimen G10 are shown in Figure 40(b). The normal stress σ_z is
compressive except for a small tensile region near the panel edge. At
the panel edges the magnitude of the shear stress $\tau_{\theta z}$ is greater than
the shear stress τ_{xz}, which is greater than the normal stress σ_z. The
maximum values of all interlaminar stresses are at the panel edges and
the maximum values are larger for the thinner panels than for the
thicker panels. The bending strain distribution in Figure 39 and the
equilibrium equations (3.90) to (3.92) indicate that the thinner panels
with severe bending gradients near the panel edge (e.g., see Fig. 39(a))
also have severe interlaminar stress gradients near the panel edge
(e.g., see Fig. 40(a)). The distributions of through-the-thickness
stresses at the panel edge for the 4-ply panel are shown in Figure 41(a)
and those for the 16-ply panel are shown in Figure 41(b). These results
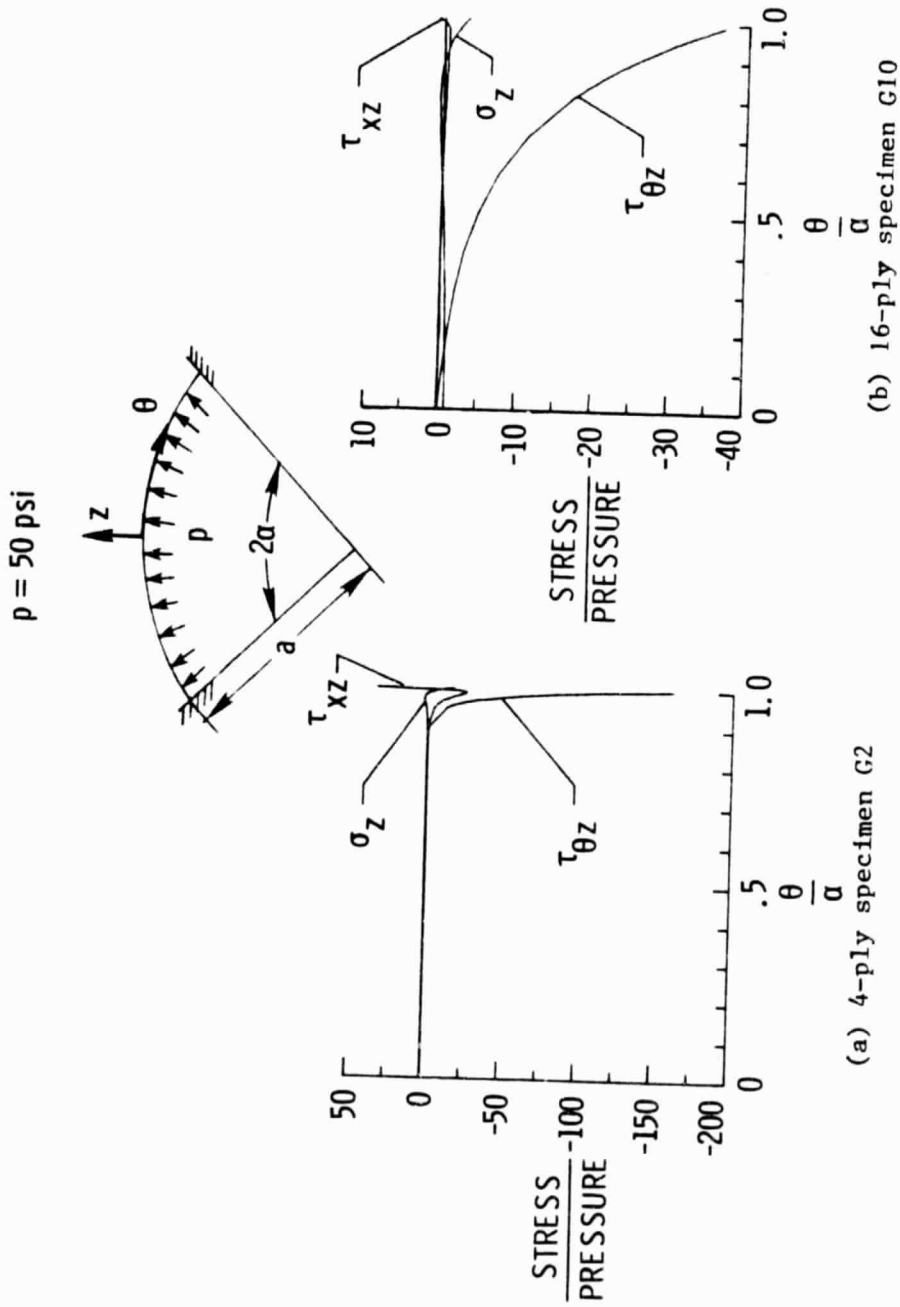
Figure 40.— Interlaminar stress distributions along the circumference at x=0, z=0, and at 50 psi for panels G2 and G10 predicted by the analysis.
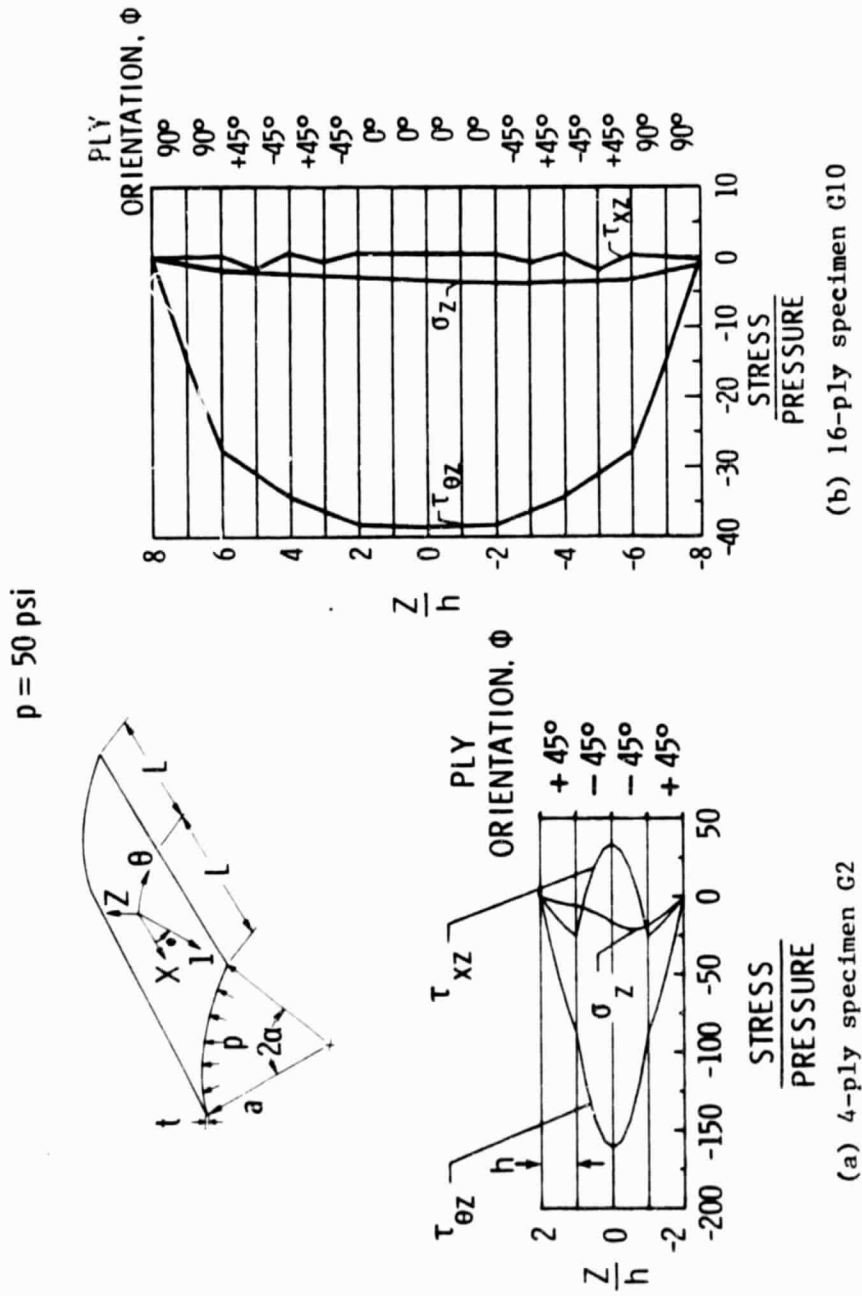
Figure 41.- Through-the-thickness distribution of normalized interlaminar stresses at the clamped edge ($\theta = \alpha$) and for an internal pressure of 50 psi for panels G2 and G10.

(a) 4-ply specimen G2

(b) 16-ply specimen G10

indicate that the shearing deformation stresses are symmetric about the middle surface and the transverse normal stress is nonsymmetric. The normal stress is equal to the applied internal pressure on the concave surface of the panel and equal to zero on the convex surface. The shear stresses are both equal to zero on the panel external surfaces. The fluctuations in the shear stress τ_{xz} are related to changes in ply orientation from +45 to -45, and the maximum value of shear stress $\tau_{\theta z}$ occurs at the panel middle surface.

Chapter 6

FAILURE

6.1 Observations of the Failed Specimens

6.1.1 Examinations of the External Surfaces

All specimens except the aluminum panel A2 were tested to failure
to study their failure characteristics, and to determine their ultimate
pressure. The applied internal pressure was slowly increased until the
specimens ruptured along a straight or curved edge and the applied
pressure could not be maintained. The failures initiated at the bound-
aries of the panels and not in the interior. Most failures occurred
along the straight edges as shown in Figure 42. Photographs of the
concave and convex surfaces of each failed panel are included in
Appendix A.

The edge failure locations for each panel shown in the photographs
in Appendix A are summarized in Table 6. The straight edges are identi-
fied as S1 and S2 and the curved edges as C1 and C2. Edge S1 is closest
to the strain gages located along the circumferential center line, and
edge C1 is closest to the strain gages located along the axial center
line. The edge failures have visible damage on both the concave and
convex surfaces. When the failure is characterized by a complete break
of all laminas through the thickness, the edge is marked with an aster-
isk superscript in Table 6. In the other cases the laminate failure
does not completely separate the interior test portion from the clamped
portion of the laminate. For example, the concave surface plies of

(a) Aluminum specimen A1

(b) Graphite-epoxy specimen G7
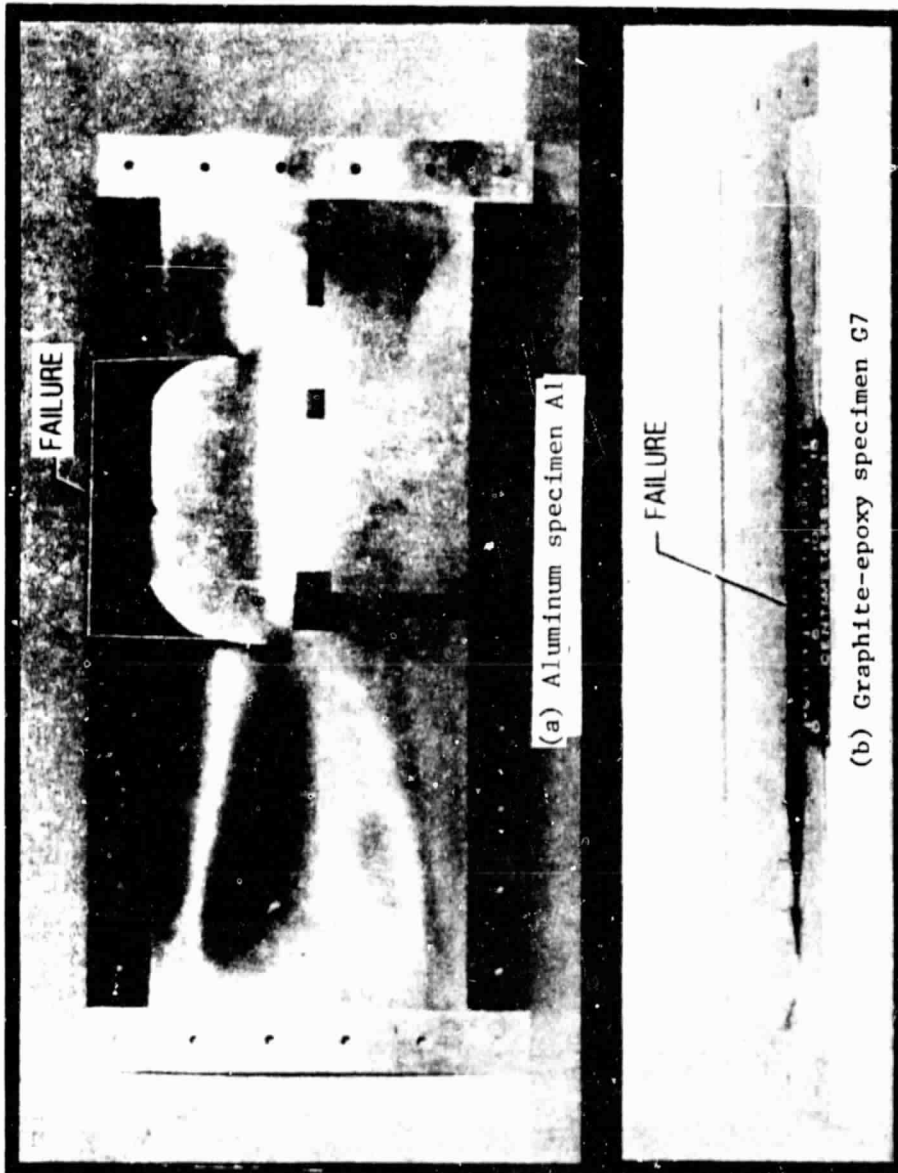
Figure 42.- Typical failed specimens.

Table 6. Edge Failure Description

Panel	Stacking Sequence	Edge Failure[1,2]	Concave Ply Failure Only
A1	--	S2*	--
A2	--	Not failed	--
G1	$[\pm45]_s$	C1* S2* C2	S1
G2	$[\pm45]_s$	C1 S2* C2	--
G3	$[\pm45/\overline{90}]_s$	C1*-S2*-C2*	--
G4	$[\pm45/\overline{90}]_s$	S1* C2* S2*	--
G5	$[90/\pm45/0]_s$	S1*	C2
G6	$[90/0/\pm45]_s$	S1*	C1 S2 C2
G7	$[90/0/\pm45]_s$	S2*	C1 S1 C2
G8	$[\pm45]_{2s}$	C1*-S2*	--
G9	$[\pm45/\pm45/90_2/0_2]_s$	S2	--
G10	$[\pm45/\pm45/90_2/0_2]_s$	S1	--
G11	$[90_2/\pm45/\pm45/0_2]_s$	S1*	--
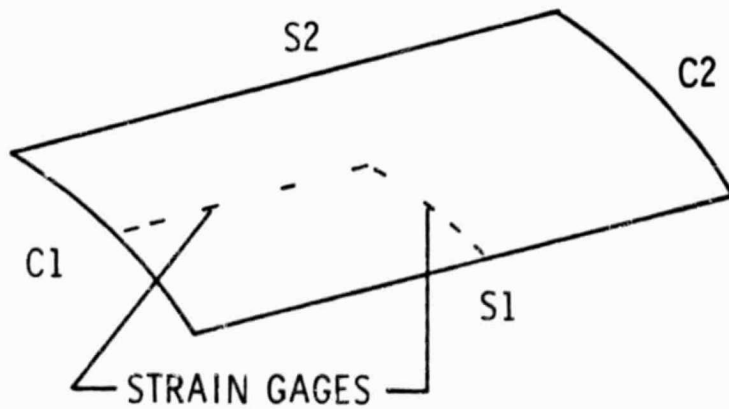
[1] An asterisk superscript on edge indicates all lamina have failed through-the-thickness

[2] A dash between edge designators indicates the failure is continuous between edges

panels G9 and G10 delaminated and failed at the bolt holes as shown in Figures A11 and A12 in Appendix A. In Table 6 a dash between two edges indicates that the edge failure is continuous between these two adjacent edges. Also in the fourth column of Table 6, the edges in which the concave surface plies failed are identified. These edges did not fail catastrophically but the concave surface ply failures may have contributed to the catastrophic failure of the other edges. Delaminations occurred at the failed edge(s) of all the specimens.

The 4- and 5-ply specimens G1, G2, G3, and G4 were composed primarily of 45° plies and failed with extensive surface fiber delamination which extends from the edge to the center as shown in Figures A3, A4, and A5 in Appendix A. These panels had more damage around the curved edge than the thicker panels. In general the thicker panels failed exclusively along the straight edge. The concave surface plies of specimens G6 and G7 have failed at the edge as indicated in Table 6. These failed plies are delaminated from the panel almost completely along the edge. Some delaminations extend as much as a distance of 2 inches normal to the edge. The 16-ply specimens G9 and G10 had failures which extended to the bolt holes on the concave surface but not completely through the thickness of the specimen at the edge. Specimens G9 and G10 had the ±45° plies located closer to the outer surfaces of the laminate rather than near the middle. The 16-ply panel G11 which had ±45° plies at the middle surface failed completely through the thickness at the edge.

6.1.2 Panel Dissection

Typically the failures occurred along one edge of the panel leaving the other edge intact. The failed edge was often too severely damaged to determine where failure initiated. The intact edge opposite the failed edge of the panel experiences an identical stress state as the failed edge prior to ultimate failure. These stress states are identical because of the symmetry in the pressure load and boundary conditions. Therefore, the intact edge should give a good indication of the local failure state immediately before failure. The results described in Table 6 are from a surface examination of the specimens and describe the edge failure locations, surface damage states and whether the crack is continuous through the thickness or not. However, it was impossible to accurately determine what was happening through the thickness of the laminate. To accomplish this examination, the panels were cut along the circumferential direction (at $x = 0$) and the cross section was polished. Only the circumferential cross section will be examined since most failures occurred along the straight edge where the one-dimensional analysis was valid. The thinner panels had a greater tendency to fail near the curved edges. The circumferential cross section was examined under a 10 power hand lens and photographs were taken to determine the extent of any local damage at the intact edge opposite the failed edge.

Photographs of the circumferential cross section of the intact and failed edges of the 16-ply specimen C9 are shown in Figure 43(a). Matrix cracks in the center four $0°$ plies are visible at both edges and
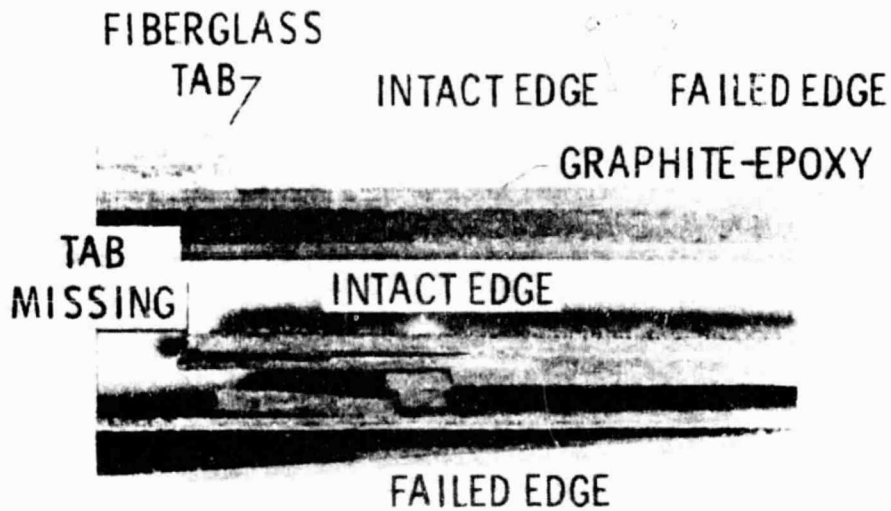
(a) 16-ply specimen G9 intact and failed edge cross sections
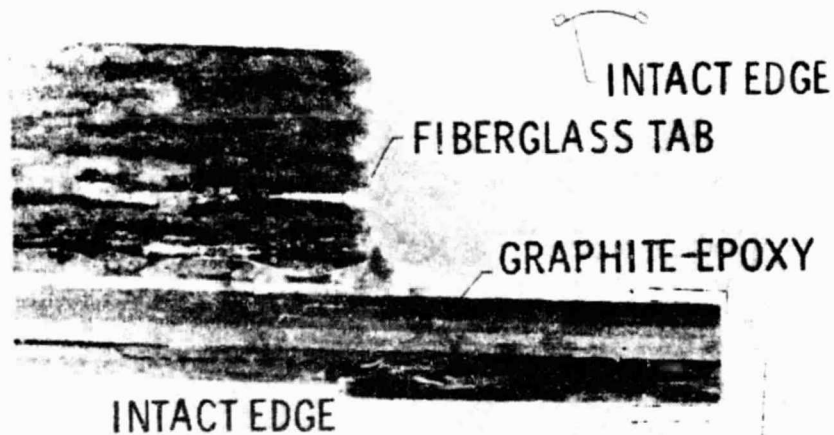
(b) 8-ply specimen G7 intact edge cross section

Figure 43.- Cross sections of intact and failed specimen edges.

may have been caused by the high transverse shear stress $\tau_{\theta z}$ and the circumferential normal stress σ_θ shown in Figure 41(b). A photograph of the cross section of the intact edge of 8-ply quasi-isotropic specimen G7 is shown in Figure 43(b). Transverse matrix cracks and delaminations are visible, and the two outer plies on the concave side have failed in tension and have delaminated.

The results of these cross-sectional examinations are summarized in Table 7. Damage at both the intact and failed edges are described in Table 7. The type of damage and the through-the-thickness ply locations are identified. Delaminations (D) and fiber breakages (F) of specific plies are identified in the table. The damage designation (D or F) is followed by numbers in the table which either identify the adjacent plies which have delaminated or identify the ply which has fiber failures. The plies are consecutively numbered from the concave surface to the convex surface. Transverse matrix cracks were visible in most of the specimen cross sections and are not included in Table 7. It is very interesting that panels with significant failure along one edge had no damage along the intact edge.

6.2 Interpretation of Strain Gage Data

In addition to the photomicrographs the response of strain gages located at the clamped edge of the panels was also very important in understanding the failure mechanisms. The strain response of back-to-back circumferential strain gages near the straight edge of specimen G7 is shown in Figure 44. The responses of the convex and concave gages

Table 7.   Observable Damage In Machined Circumferential Edge
Cross Section

SPECI-MEN	STACKING SEQUENCE	DAMAGE		COMMENTS
		INTACT EDGE	FAILED EDGE	
G1	$[\pm45]_s$	D[a] 1-2[b]	Severe	D under tab
G2	$[\pm45]_s$	D 1-2 D 3-4	Severe	D 1-2 under tab D 3-4 in test section
G3	$[\pm45/\overline{90}]_s$	D 1-2	Severe	D in test section
G4	$[\pm45/\overline{90}]_s$	Severe	Severe	Both edges failed
G5	$[90/\pm45/0]_s$	None	D 1-2 D 2-3 D 3-4 D 7-8	D 1/8" from edge D between all plies at failed edge
G6	$[90/0/\pm45]_s$	F[a]1 and 2 D 2-3 D 3-4	D 2-3 D 3-4	
G7	$[90/0/\pm45]_s$	F 1 and 2 D 2-3 D 3-4	D 2-3 D 3-4 D 5-6	D mainly in test section
G8	$[\pm45]_{2s}$	D 5-6	D 3-4	Both edges intact at cross section examined D under tab
G9	$[\pm45/\pm45/90_2/0_2]_s$	None	D 6-7 D 10-11 D 13-14	D 6-7 7/8" under tab and 2" in test section Severe damage at failed edge
G10	$[\pm45/\pm45/90_2/0_2]_s$	D 5-6 D 6-7 D 2-3	D 6-7 D 10-11	Most damage on intact edge under tab;F 1 and 2 under tabs
G11	$[90_2/\pm45/\pm45/0_2]_s$	None	D 2-3 D 5-6 D 6-7	Most D in test section

[a] D = delamination; F = fiber breakage

[b] Numbers refer to lamina location. Lamina numbered consecutively from concave to convex surface. A dash indicates delamination occurs between laminas (i.e. 1-2 indicates delamination between the first and second ply)
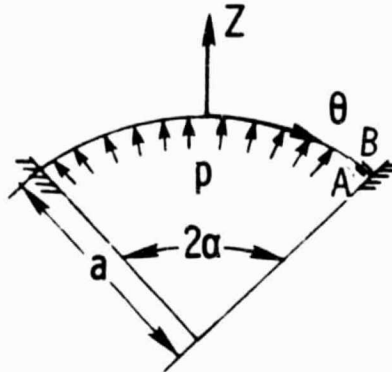
8-PLY STRAIN RESPONSE
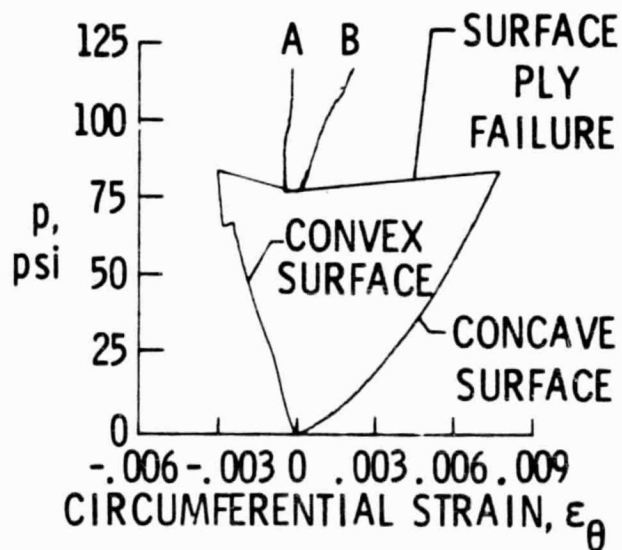
Figure 44.- Circumferential strain response of back-to-back gages located at clamped edge ($x=0.$, $\theta = 0$) of specimen G7.

are smooth until a small discontinuity occurs at approximately 61 psi.
This discontinuity is associated with an abrupt circumferential slip at
the boundary shown by the displacement response data in Figure 35. The
effect of circumferential slip on the edge strain response was shown in
Figure 20. The slip caused an increase in bending strain and a decrease
in middle surface strain. The decrease in the middle surface strain is
offset by the increase in the bending strain at the concave surface.
The opposite effect occurs at the convex surface and the slip shows up
as a discontinuity in the gage response.

Figure 44 also shows a larger discontinuity at an internal pressure
of 82.7 psi where both the convex and concave strains abruptly change.
The concave gage which was indicating a large tensile strain before the
discontinuity registers zero immediately after the event. The convex
gage which was increasing in compression registers tension immediately
after the event. As the pressure increases the concave gage changes
only slightly and continues to register nearly zero and the tensile
strain measured by the convex gage increases. This behavior is
explained by a local failure of the concave surface plies at the clamped
straight edge. This concave surface failure is substantiated by the
photomicrographs of specimen G7 shown in Figure 43. The 90° concave
surface ply in Figure 43 has failed by a tensile fiber failure at the
edge. The 0° inside ply next to the 90° ply has also failed circum-
ferentially in a tensile matrix failure mode at the edge. Delamination
of both the 0° and 90° plies is apparent from the edge inward. This
delamination propagates under the concave surface strain gage which is

located approximately one-eighth of an inch away from the edge. The strain gage on the concave surface remains attached to the two delaminated plies and registers a strain of zero reflecting the loss of load carrying capability. With the two plies on the concave side failed, the remaining laminate must now support the tensile stress resultant and the convex strain gage registers an increasing tensile strain. The responses of the edge strain gages for panels G2, G4, G7, G9, and G10 are given in Appendix B. Local edge failures, such as occur at 82.7 psi for specimen G7, have a large detectable influence on the strain gage responses shown in Appendix B.

6.3 First Major Damage Event and Ultimate Failure

The discontinuities in the edge strain gage response are believed to be caused by either a fiber fracture or delamination. Many local failures were audible during the test and their effects on panel response were detected by the edge strain gages. As will be shown in Section 6.4, the analysis predicts transverse matrix cracking to occur at lower pressures than fiber fracture. Transverse matrix cracking is classified as minor damage since it did not cause a discontinuity or abrupt slope change in the measured strain response. The strains at the first major damage event, and at ultimate pressure were determined from the edge strain response given in Appendix B and are presented in Tables 8 and 9.

Table 8. Measured circumferential strains at occurrence of first damage and ultimate pressures. Strain gages located near center of straight edge of panel.

Specimen	Gage Distance From Edge, in.	First Damage Pressure, psi	Surface Strains Before First Damage		Surface Strains After First Damage		Ultimate Pressure, psi	Surface Strains Before Ultimate	
			$\varepsilon_\theta(-\frac{h}{2})$	$\varepsilon_\theta(+\frac{h}{2})$	$\varepsilon_\theta(-\frac{h}{2})$	$\varepsilon_\theta(+\frac{h}{2})$		$\varepsilon_\theta(-\frac{h}{2})$	$\varepsilon_\theta(+\frac{h}{2})$
A1	1/8	138.6	–	–	–	–	138.6	–	–
A2	0^+	–	–	–	–	–	>225	–	–
C1	1/8	98.8	–	.0073	–	–	98.8	–	.0073
G2	0^+	61.9	–	-.0040	–	-.0040	101.3	–	.0013
C3	1/8	86.7	.0089	.0029	–	–	86.7	.0089	.0029
G4	0^+	91.3	–	-.0058	–	–	91.3	–	-.0058
G5	0^+	105.5	.0133	-.0042	–	–	105.5	.0133	-.0042
G6	0^+	88.3	.0135	-.0052	–	-.0017	106.3	–	-.0002
G7	1/8	82.6	.0077	-.0030	-.0005	.0005	114.9	-.0002	.0022
G8	1/8	134.4	–	-.0079	–	-.0062	141.3	–	-.0020
C9	0^+	75.9	.0106	-.0084	.0100	-.0085	165.9	.0210	-.0160
G10	0^+	99.7	.0106	-.0055	.0102	-.0054	148.1	.0050	-.0045
G11	1/8	147.7	.0103	-.0047	–	–	147.7	.0103	-.0047

Table 9. Measured axial strains at occurrence of first damage and ultimate pressures. Strain gages located at center of curved edge of panel.

Specimen	Gage Distance From Edge, in.	First Damage Pressure, psi	Surface Strains Before First Damage		Surface Strains After First Damage		Ultimate Pressure, psi	Surface Strains Before Ultimate	
			$\varepsilon_x(-\tfrac{h}{2})$	$\varepsilon_x(+\tfrac{h}{2})$	$\varepsilon_x(-\tfrac{h}{2})$	$\varepsilon_x(+\tfrac{h}{2})$		$\varepsilon_x(-\tfrac{h}{2})$	$\varepsilon_x(+\tfrac{h}{2})$
A1	1/8	138.6	-	-	-	-	138.6	-	-.0077
A2	1/8	-	-	-	-	-	>225	.0024	.0077
G1	1/8	98.8	-	-	-	-	98.8	-	.0058
G2	0+	74.3	-	0.	-	-	101.3	-	.0059
G3	1/8	61.2	.0069	.0027	-	.0008	86.7	-	.0047
G4	0+	56.8	.0120	-.0044	.0069	.0027	91.3	.0077	-.0025
G5	1/8	105.5	-	-	.0113	-.0036	105.5	.0128	-.0040
G6	1/8	82.0	.0063	-.0039	.0054	-.0031	106.3	.0073	.0008
G7	1/8	98.9	.0077	-.0041	.0001	-.0013	114.9	.0013	-.0015
G8	1/8	119.6	.0137	.0003	.0096	.0013	141.3	0	.0052
G9	1/8	165.9	-	-	-	-	165.9	.0087	-.0078
G10	1/8	66.3	.0068	-.0059	.0036	-.0063	148.1	.0099	-.0099
G11	1/8	147.7	-	-	-	-	147.7	.0096	-.0065

Measured circumferential surface strains near the clamped straight edge of the panel are given in Table 8 and axial strains near the clamped curved edge of the panel are given in Table 9. These strains are recorded by edge gages immediately before and after the first major damage event and at the ultimate pressure. The axial gages are located approximately at the center of the curved edge, and the circumferential gages are located at the center of the straight edge. The gages were either located one-eighth of an inch away from the edge or as close as possible to the edge which is indicated by 0^+ in Tables 8 and 9. For example, distances of 0.020 in. and 0.030 in. were measured between the strain gages and the edge for specimens G9 and G10, respectively. The strains could not be recorded to failure for all panels because in some instances the strain gages failed due to the high strains. Also, for some of the panels in the table, the strains after the first major damage event are not reported since the first major damage event occurred simultaneously with rupture at the ultimate pressure.

The first major damage event pressure and the ultimate pressure are plotted in Figure 45 for the specimens tested in this investigation. Also shown on the figure is the maximum pressure applied to the thicker aluminum specimen (specimen A2) which was not tested to failure. All specimens failed at pressures well above 20 psi which is greater than the nominal pressure used for ground test verification of pressurized fuselage structure. The aluminum specimens yielded at the specimen edges to form plastic hinges that reduced the bending strains at the edges. The lighter weight graphite-epoxy specimens failed at lower pressures than the aluminum specimens with the same nominal thicknesses.
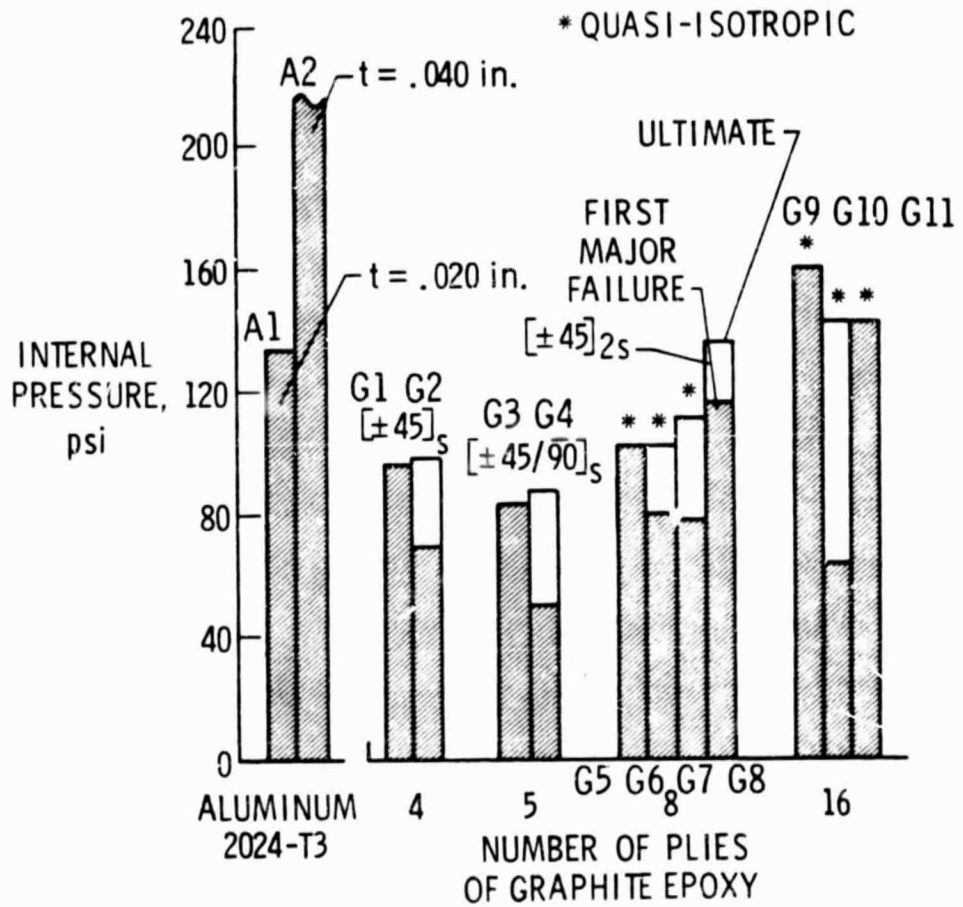
Figure 45.- First major local failure pressure and ultimate pressure of all specimens tested.

Ply orientation and laminate thickness appear to have a strong influence on the ultimate pressure capability of the graphite-epoxy specimens. As shown in Figure 45, the 16-ply quasi-isotropic panels (G9, G10, and G11) did not fail at twice the ultimate pressure of the 8-ply quasi-isotropic panels (G5, G6, and G7) and the 8-ply ±45°-angle-ply panel (G8) did not fail at twice the ultimate pressure of the 4-ply ±45°-angle-ply panels (G1 and G2). Although the strains, bending gradients and interlaminar stresses at the panel edges are more severe for the thinner panels (see Figs. 39-41), the thinner panels are more structurally efficient on a weight basis with respect to their ultimate pressure capability than the thicker panels. The 8-ply quasi-isotropic panels (G5, G6, and G7) failed at lower pressures than the 8-ply ±45°-angle-ply panel (G8) and the 5-ply $[\pm 45/\overline{90}]_s$ panels (G3 and G4) failed at lower pressures than the 4-ply ±45°-angle-ply panels (G1 and G2). Graphite-epoxy specimens G1, G3, G5, G9, and G11 ruptured with a sudden loss of pressure and with no indication from the response of the edge strain gages of progressive local failures or damage occurring at pressure below the ultimate pressure. The other graphite-epoxy specimens had one or more major local failures (e.g., fiber fracture or delamination) occur at pressures below the ultimate pressure.

6.4 Evaluation of Failure Criteria

The stresses computed from the one-dimensional panel analysis were used to determine if the first major damage event could be predicted by some commonly used failure criteria. Stresses at the straight edges of

panels G2, G4, G7, G9, and G10 were determined at the pressures asso-
ciated with the major damage events given in Table 8. The analyses
utilized the measured radius, circumferential slip, and axial strain for
each specimen to model the response as accurately as possible. The
strains and stresses determined from the analyses were substituted into
phenomenological and individual mode failure criteria. Six different
individual modes of failure and two phenomenological failure criteria
were examined. The individual failure modes included tensile fiber,
compressive fiber, tensile matrix, compressive matrix, tensile inter-
laminar, and compressive interlaminar failure modes (Ref. 21) and are
shown in Appendix C. The material strength properties used in the
failure criteria are given in Table 10. The phenomenological failure
criteria include a two-dimensional Tsai-Wu failure criterion which is
based on the in-plane stresses (σ_{xx}, $\sigma_{\theta\theta}$, and $\tau_{x\theta}$), and the more
general three-dimensional Tsai-Wu functional which includes the in-plane
stresses and the through-the-thickness stresses (τ_{xz}, $\tau_{\theta z}$, and σ_{zz}).
The Tsai-Wu functional utilizing the full three-dimensional stress state
is given in Appendix D. The two-dimensional Tsai-Wu failure criterion
found in many composite material text books is a specialized case of the
three-dimensional criterion. These failure criteria were examined
across the circumference and through the thickness of the panels. The
maximum value (dimensionless) of each criterion occurs at the clamped
edge but at different locations through the thickness. These values are
given in Table 11 at the first major damage event pressures. Values
greater than unity indicate failure in each criterion. The value of the

Table 10. Material Strength Properties of T300/5208 Used in the
          Failure Criteria

Property[1]	Symbol	Strength, ksi
Axial Tensile Strength	X_t	218.0
Axial Compressive Strength	X_c	-218.0
Transverse In-plane Tensile Strength	Y_t	6.1
Transverse In-plane Compressive Strength	Y_c	-21.4
Transverse Thickness Tensile Strength	Z_t	6.1
Transverse Thickness Compressive Strength	Z_c	-21.4
Shear Strength in x-y Plane	S_{xy}	9.8
Shear Strength in x-z Plane	S_{xz}	9.8
Shear Strength in y-z Plane	S_{yz}	6.0

[1] Coordinate x refers to the axial or fiber direction

Coordinate y refers to the transverse in-plane direction

Coordinate z refers to the transverse thickness direction

Table 11. Maximum Values of Failure Criteria at First Damage
Pressure. All Maximum Failure Criteria Values Occur
at the Clamped Edge.[1]

Specimen	Pressure, psi	Failure Criterion			
		2-D Tensor Polynomial	3-D Tensor Polynomial	Tensile Fiber	Compressive Fiber
G2	61.93	22.41 (I)	22.40 (I)	1.29 (I)	0.69 (0)
G4	86.69	27.45 (I)	27.44 (I)	1.44 (I)	0.93 (0)
G7	82.55	7.12 (1-2*)	7.56 (1-2*)	1.35 (I)	0.66 (0)
G9	75.94	5.64 (I)	5.63 (I)	0.64 (4-5*)	0.42 (0)
G10	99.69	3.75 (2-3*)	3.78 (2-3*)	1.11 (I)	0.83 (0)

Specimen	Pressure, psi	Failure Criterion			
		Tensile Matrix	Compressive Matrix	Tensile Interlaminar	Compressive Interlaminar
G2	61.93	44.04 (I)	10.99 (I)	2.45 (M)	2.29 (M)
G4	86.69	55.09 (I)	13.70 (I)	3.67 (2-3*)	3.45 (3-4*)
G7	82.55	15.27 (1-2*)	1.69 (1-2*)	0.82 (M)	0.76 (M)
G9	75.94	8.97 (I)	2.32 (I)	0.45 (M)	0.40 (9-10*)
G10	99.69	5.41 (2-3*)	1.43 (2-3*)	0.53 (M)	0.46 (9-10*)

[1] The through-the-thickness failure prediction location are identified by the following notation:

I - Failure predicted at the inside or concave surface fiber

0 - Failure predicted at the outside or convex surface fiber

M - Failure predicted at the middle surface

1-2* - Failure predicted at the interface of plies 1 and 2, and in ply 2 marked with an asterisk. Plies are numbered consecutively beginning with the concave surface ply

tensile matrix failure mode is much greater than unity which indicates that tensile matrix cracking was predicted at a pressure lower than the pressure of the first major damage event. The two-dimensional and three-dimensional Tsai-Wu functions are also very large due to the influence of a similar transverse matrix term in the criteria. No abrupt changes in the panels response nor substantial water leaking was observed due to the occurrence of transverse matrix cracking. The maximum value of the three-dimensional Tsai-Wu function occurs at the same location as the two-dimensional Tsai-Wu function and the values of each do not significantly differ. The influence of the through-the-thickness stresses which are a maximum at or near the middle surface is not significant on the magnitude or location through the thickness of the maximum Tsai-Wu value. The values of the failure criterion do change significantly at the midplane of the laminate where the through-the-thickness stresses are largest and the bending stresses vanish. For most of the panels the tensile fiber mode has values closer to unity than any of the other criteria. For four of the panels the analysis predicts tensile fiber mode of failure values greater than unity. The analysis did not model all phenomena which were observed in the experiment. Transverse matrix cracking and edge rotation from incomplete clamping affect the experimental response but are not modeled analytically. The tensile fiber mode is analogous to the maximum-stress failure criterion applied in the tensile fiber-direction and appears to correlate reasonably well with the pressures corresponding to the first major damage event.

Chapter 7

CONCLUDING REMARKS

An experimental and analytical investigation was conducted to study
the nonlinear response and failure characteristics of internally pres-
surized 4- to 16-ply-thick graphite-epoxy cylindrical panels with
clamped edges. The panels were selected to simulate the skin between
two frames and two stringers of a typical transport fuselage structure.
The stiffness of each panel tested, as measured by the slope of the
response curve relating the radial deflection of the panel center to the
applied internal pressure, increased with increasing internal pressure
which is characteristic of a geometrically nonlinear response. Clamping
the panel edges caused local bending and interlaminar stress gradients
near the panel edges and these gradients were found to be more severe
for the thinner panels. The radial deflections of the panels were uni-
form in the axial direction over a substantial portion of the central
region of the panels.

A one-dimensional cylindrical panel analysis based on nonlinear
shallow shell theory was derived and used to determine the nonlinear
response of the central region of the panels. The formulation included
through-the-thickness shear deformations which introduce the twist-
coupling coefficient D_{26} into the analysis. Twist-coupling coeffi-
cient effects were determined to be important for response quantities in
the region of severe bending gradients near the clamped straight edge.
Neglecting through-the-thickness shear effects in the analysis gives

158

edge stresses which are higher than those predicted with through-the-thickness shear for some laminates, but lower for other laminates. This nonconservative nature limits the use of the Kirchhoff-Love shell theory. When the measured initial radius and the effects of measured in-plane circumferential displacements at the panel edges and measured axial membrane strain at the panel center are included, the one-dimensional panel analysis accurately predicts the nonlinear response of panels away from the curved edges. The analytical results correlate well with the experimental results up to the first major damage event including the severe local bending gradients at the panel straight edges.

Different boundary conditions were examined to study the nature of the geometric nonlinearity, to approximate more closely "real life" conditions, and to evaluate experimental boundary condition anomalies. The important geometric nonlinearity in this problem results from the product of the membrane hoop tension and the slope of the radial deflection. The nonlinearity disappears when the edge is allowed free radial expansion. In this case the radial deflection slope goes to zero since every point on the circumferential curve deforms uniformly in the radial direction. Another boundary condition evaluated was the rotation. The circumferential and radial boundary displacements were set to zero and the limiting cases of clamped and simply supported edge rotation were examined. The differences between clamped and simply supported boundary conditions in the panel responses at the panel centers were very small for thin panels. Rotations of the panel edges allowed by incomplete

clamping and individual ply failures at the edge did not have a large influence on the center response of the panels. The fact that the panel center response was relatively insensitive to the extremes in rotational constraint imposed by clamped and simply supported boundary conditions explains why such good correlation existed between the test and clamped analysis results for pressures up to the ultimate pressure. The local bending strains near the edge were vastly different for the two different boundary conditons. The simply supported panels had no bending strains at the edge. The clamped panels had rapid variations in the bending strain near the edge with the maximum occurring at the edge.

The graphite-epoxy panels failed along the panel edges where the local bending and interlaminar stress gradients occur. Some graphite-epoxy panels ruptured with a sudden loss of pressure and with no indication of local failures or damage occurring at pressure below the ultimate pressure. The other graphite-epoxy panels had one or more major local failures at pressures below the ultimate pressures. The failures appear to be caused by tensile lamina failures at the panel edges. Transverse matrix cracking and delaminations also occurred in regions with local bending and interlaminar stress gradients. Aluminum panels tested for comparison yielded and formed plastic hinges at the panel edges before rupture. A nonlinear analysis is required to predict accurately the stresses in regions with severe local bending and interlaminar stress gradients. These accurate local stress predictions are necessary in order to predict the onset of failure in brittle graphite-epoxy laminates. All graphite-epoxy panels failed at pressures well

above the 2C psi nominal pressure used for ground test verification of pressurized fuselage structure. The experimental results indicate that ply orientation and laminate thickness have a strong influence on the failure characteristics and ultimate pressures of graphite-epoxy curved panels.

In conclusion, the present study has identified and resolved important aspects in the response to internal pressure of an aircraft fuselage skin. The response was determined from experiment to be non-linear. A one-dimensional geometrically nonlinear analysis was developed and correlated well with the measured panel response. Both testing and analysis identified the skin region adjacent to the stiffeners as the critical area of the pressurized panel. A bending gradient exist in the skin near the stiffeners and initiated failure of all panels tested. The edge gradient response of the aluminum panels was different than the response of the composite panels. The aluminum relieved the edge bending gradient by yielding, whereas, the brittle graphite-epoxy developed transverse matrix cracks, fiber breakage, and delaminations at the edge. Although all panels carried pressures much greater than the design ultimate pressure, the long term durability issues of pressurized composite skins must be examined.

REFERENCES

1. Pugsley, A. G.; and Leggett, D. M. A.: "The Theory of Thin Plates Under Transverse Pressure." R. & M. No. 2094, British Aeronautical Research Council, August 1941.

2. Flügge, W.: "Stress Problems in Pressurized Cabins." NACA TN-2612, February 1952.

3. Houghton, D. S.: "The Influence of Frame Pitch and Stiffness on Stress Distribution in Pressurized Cylinders." The College of Aeronautics, Cranfield, England, CoA Note No. 79, February 1958.

4. Williams, D.: "Pressure-Cabin Problems." An Introduction to the Theory of Aircraft Structures, Edward Arnold (Publishers) Ltd., 1960, Chapter 9.

5. Wang, J. T.-S.: "Orthogonally Stiffened Cylindrical Shells Subjected to Internal Pressure." AIAA Journal, Vol. 8, No. 3, March 1970, pp. 455-461.

6. Dickson J. N.; and Biggers, S. B.: "Design and Analysis of a Stiffened Composite Fuselage Panel." NASA CR-159302, August 1980.

7. Thrall, E. W., Jr.: "Failures in Adhesively Bonded Structures." In Bonded Joints and Preparation for Bonding, AGARD Lecture Series No. 102, March 1979.

8. Boitnott, R. L.; Starnes, J. H., Jr.; and Johnson, E. R.: "Nonlinear Response and Failure Characteristics of Clamped Internally Pressurized Graphite-Epoxy Cylindrical Panels." In proceedings of AIAA/ASME/ASCE/AHS 25th Structures, Structural Dynamics, and Materials (SDM) Conference, AIAA Paper No. 84-0955-CP, Palm Springs, California, May 14-16, 1984, pp. 514-525.

9. Waltz, T. L.; and Vinson, J. R.: "Interlaminar Stresses in Laminated Cylindrical Shells." AIAA Paper No. 75-755, 1975.

10. Yuceoglu, U.; and Updike, D. P.: "Stresses in Two-Layer Bonded Orthotropic Cylindrical Shells." Emerging Technologies in Aerospace Structures, Design, Structural Dynamics and Materials, J. R. Vinson, ed., The Aerospace Division, ASME, August 1980, pp. 53-65.

11. Sanders, J. L.: "Nonlinear Theories for Thin Shells." Q. Appl. Math, Vol. 21, No. 1, 1963, pp. 21-26.

12. Koiter, W. T.: "General Equations of Elastic Stability for Thin Shells." In Proceedings-Symposium on the Theory of Shells to Honor Lloyd Hamilton Donnell, D. Muster, ed., University of Houston, Houston, Texas, 1967, p. 198.

13. Jones, R. M.: Mechanics of Composite Materials. Scripta Book Company, 1975.

14. Mindlin, R. D.: "Influence of Rotatary Inertia and Shear on Flexural Motions of Isotropic, Elastic Plates." Journal of Applied Mechanics, Vol. 18, No. 1, March 1951, pp. 31-38.

15. Whitney, J. M.: "Stress Analysis of Thick Laminated Composite and Sandwich Plates." Journal of Composite Materials, Vol. 6, October 1972, pp. 426-440.

16. Whitney, J. M.: "Shear Correction Factors for Orthotropic Laminates Under Static Load." Journal of Applied Mechanics, Vol. 40, No. 1, March 1973, pp. 303-304.

17. Whitney, J. M.; and Pagano, N. J.: "Shear Deformation in Heterogeneous Anisotropic Plates." Journal of Applied Mechanics, Vol. 37, No. 4, Dec. 1970, pp. 1031-1036.

18. Lekhnitskii, S. G.: Theory of Elasticity of an Anisotropic Elastic Body, translated from the Russian edition by Fern, P., Holden-Day, Inc., 1963, pp. 107-108.

19. Bromberg, E.; and Stoker, J. J.: "Non-Linear Theory of Curved Elastic Sheets." Quarterly of Applied Mathematics, Vol. III, No. 3, October 1945, pp. 246-265.

20. Wang, J. T.-S.: "On the Solution of Plates of Composite Materials." Journal of Composite Materials, Vol. 3, July 1969, pp. 590-592.

21. Rosen, B. W.; Nagarkar, A. P.; Pipes, R. B.; and Walsh, R.: "Research Study to Define the Critical Failure Mechanisms in Notched Composites Under Compression Fatigue Loading." Material Science Corporation, Report Number MSC TFR 1201/1801, Contract Number N00019-79-C-0633, March 1981, pp. 5-8 and 33-35.

22. Pipes, R. B.; and Cole, B. W.: "On the Off-Axis Strength Test for Anisotropic Materials." Journal of Composite Materials, Vol. 7, April 1973, pp. 246-256.

APPENDIX   A

PHOTOGRAPHS OF THE FAILED PANELS
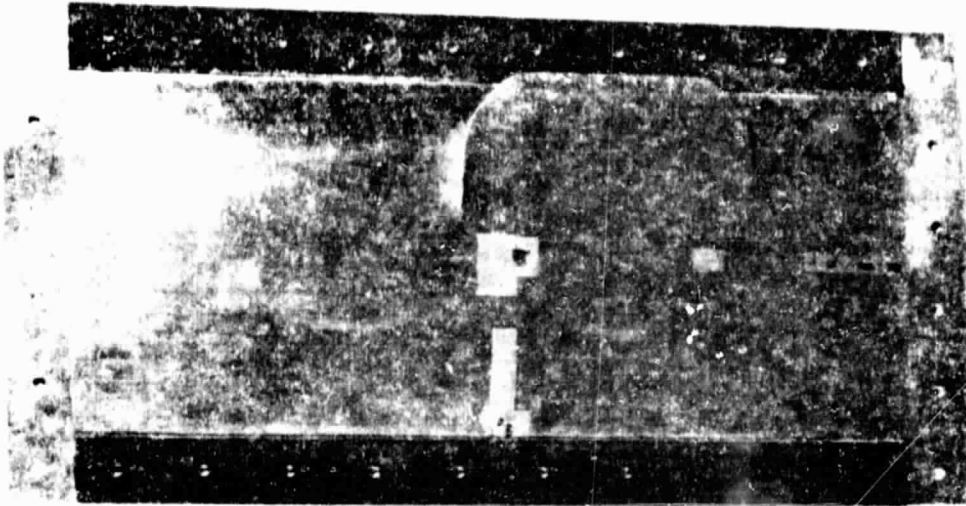
Convex Surface
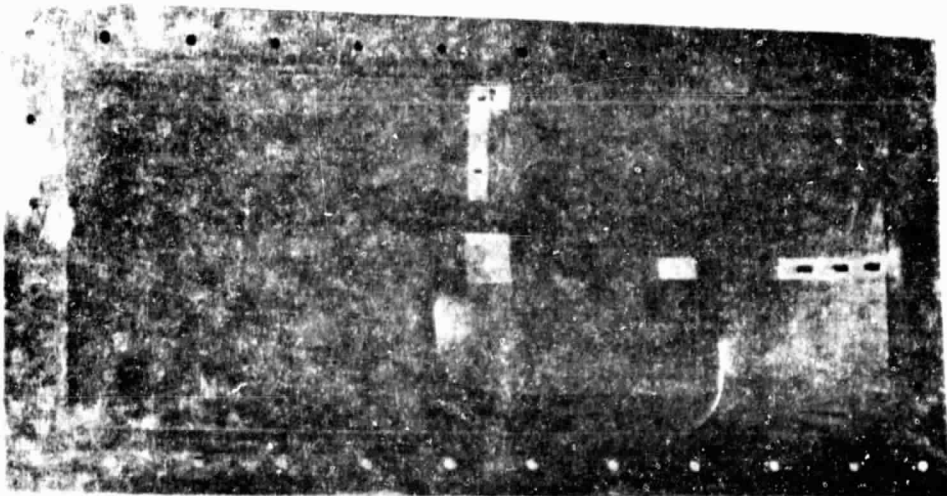
Concave Surface

Figure A1.- Aluminum Specimen A1
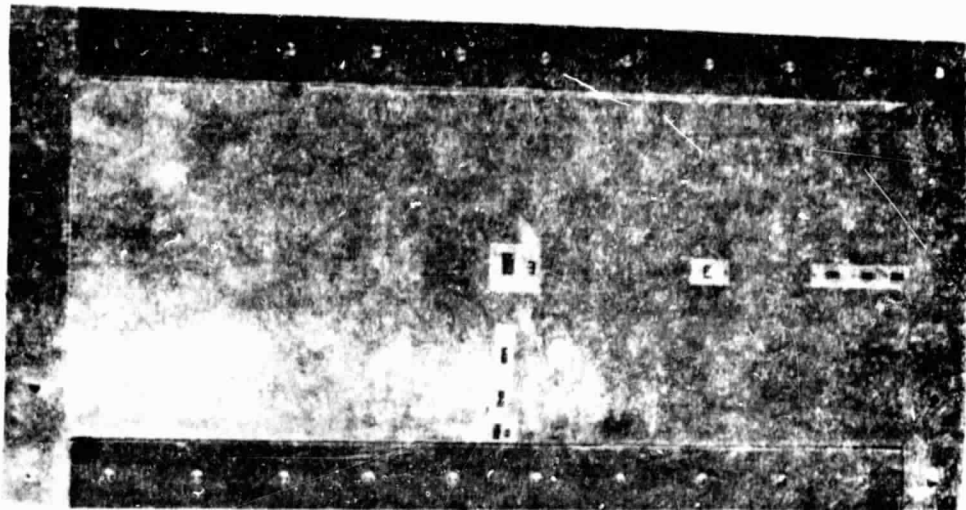
Convex Surface
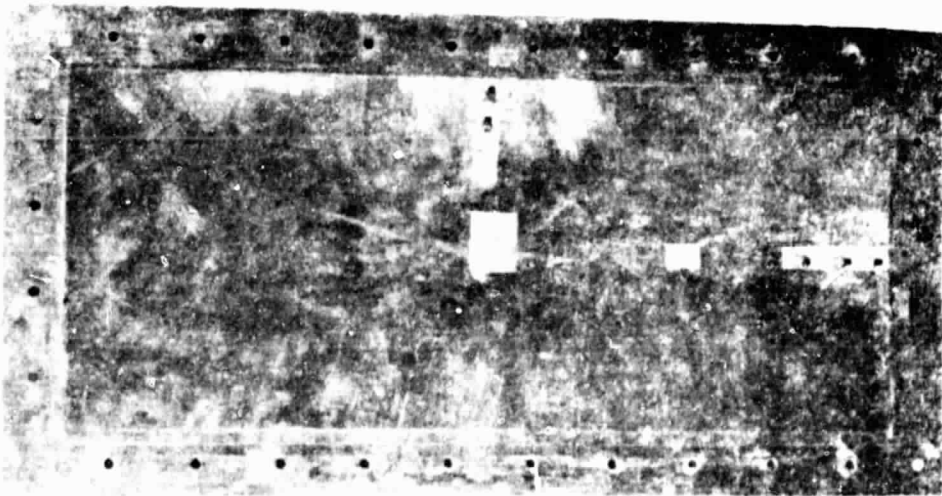
Concave Surface

Figure A2.- Aluminum Specimen A2
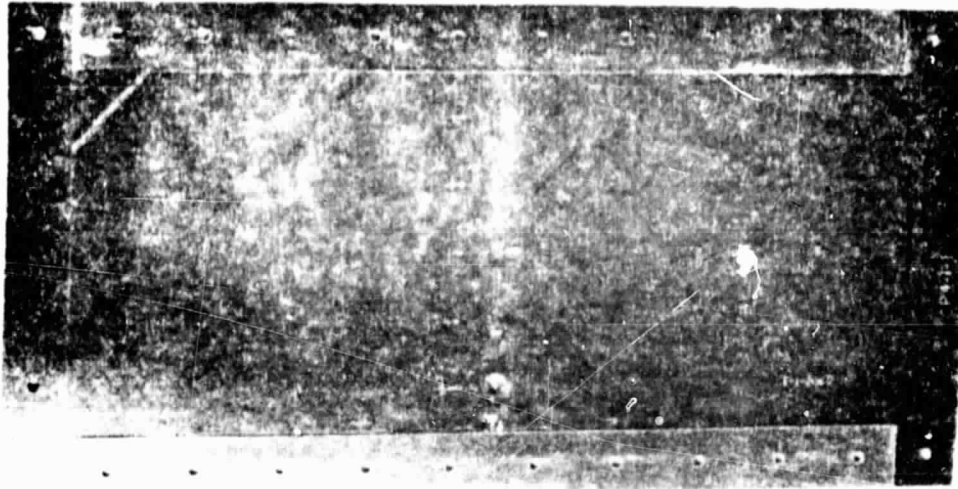
Convex Surface
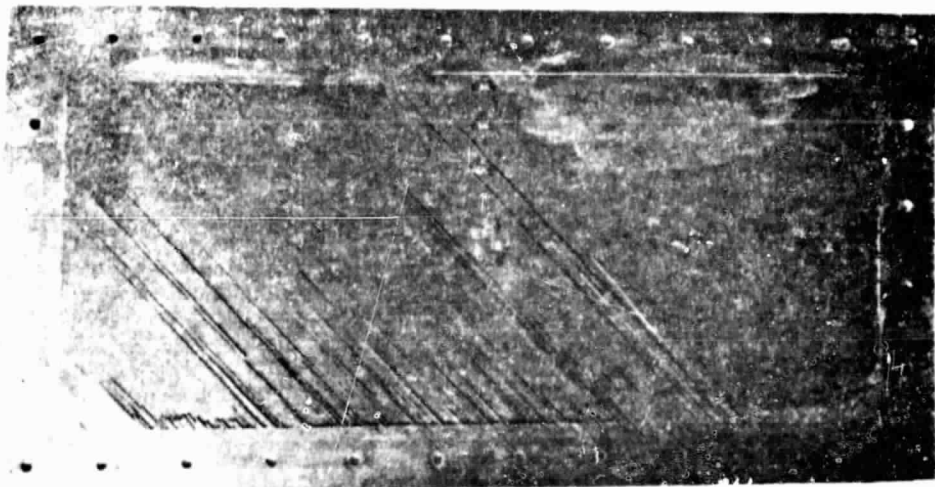
Concave Surface

Figure A3.- Graphite-epoxy Specimen C1; $[\pm 45]_s$
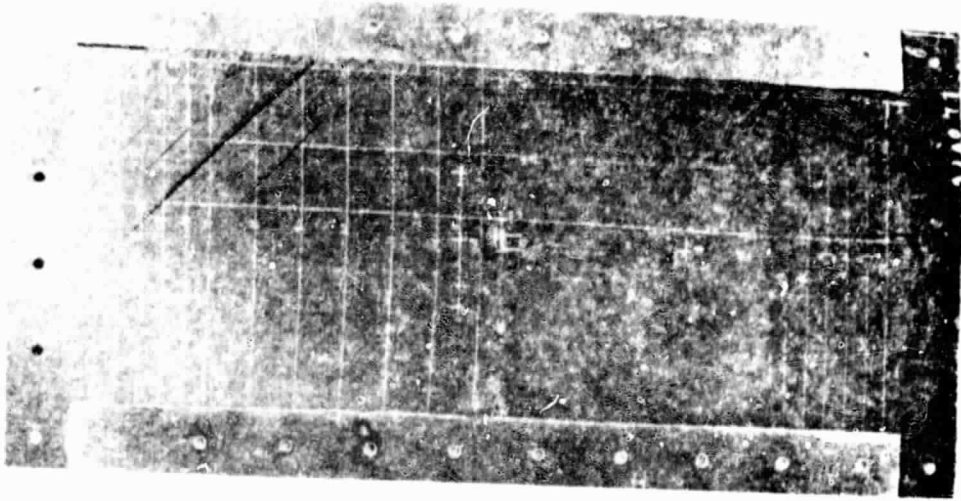
Convex Surface
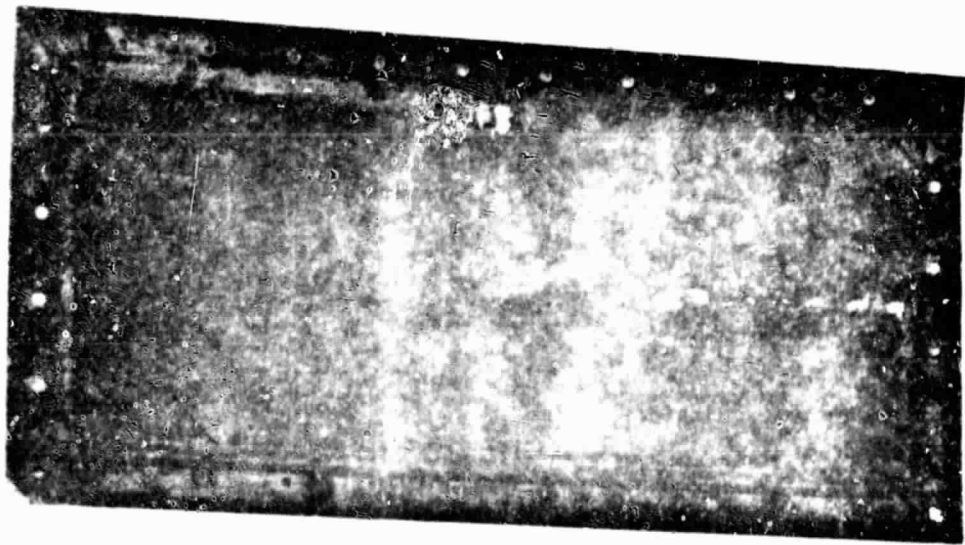
Concave Surface

Figure A4.- Graphite-epoxy Specimen G2; $[\pm45]_s$
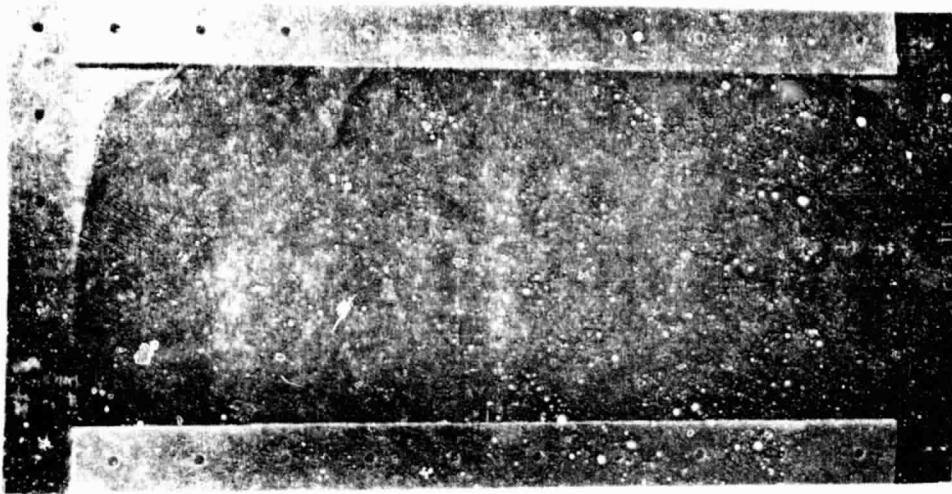
Convex Surface
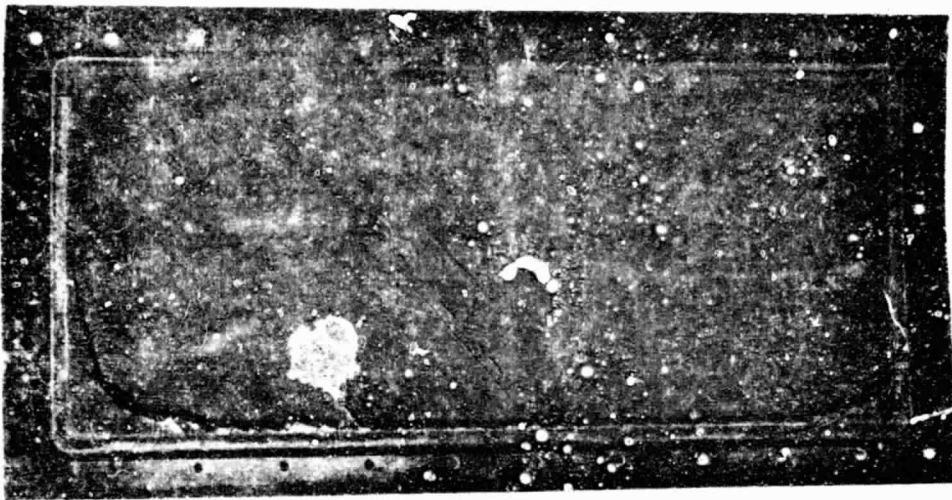
Concave Surface

Figure A5.- Graphite-epoxy Specimen G3, $[\pm 45/\overline{90}]_s$
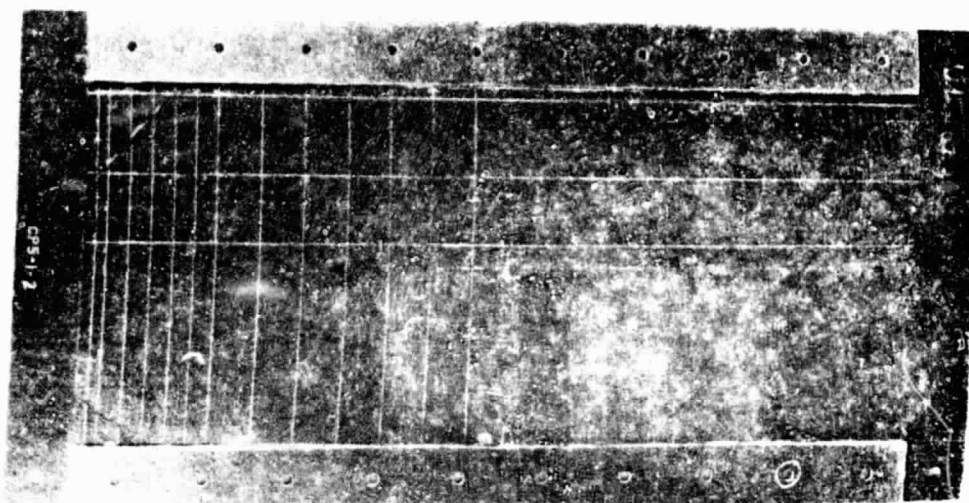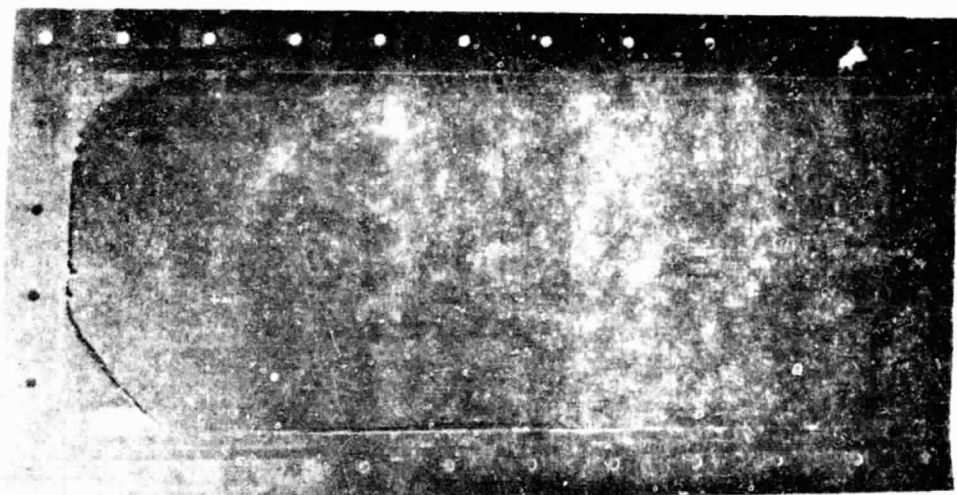
Convex Surface

Concave Surface

Figure A6.- Graphite-epoxy Specimen G4; $[\pm 45/\overline{30}]_s$
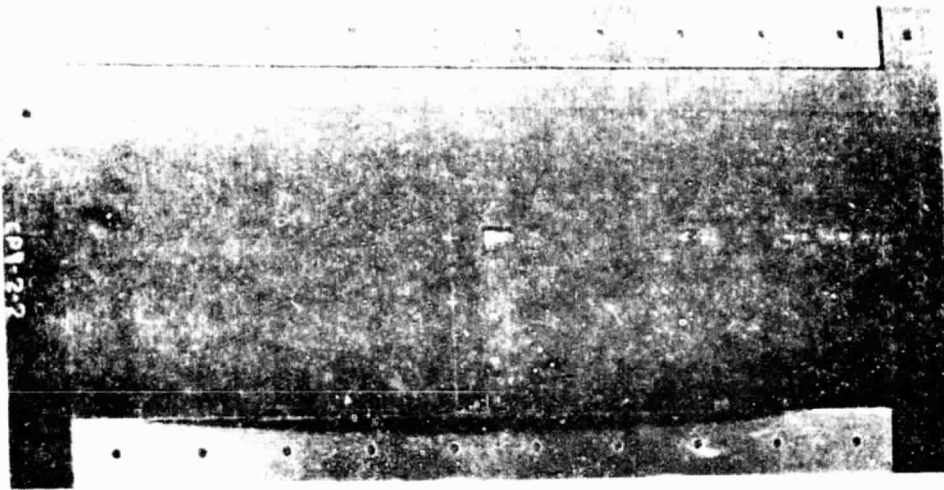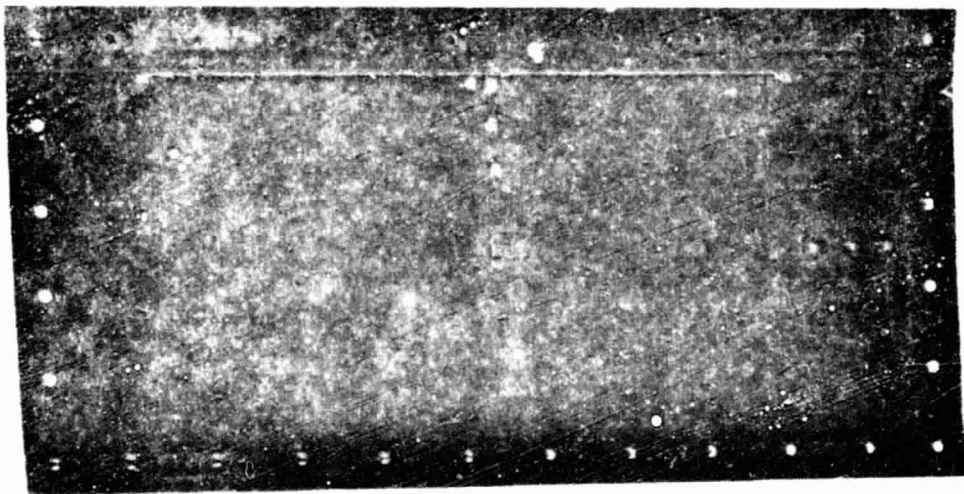
Convex Surface

Concave Surface

Figure A7.- Graphite-epoxy Specimen G5; $[90/\pm45/0]_s$
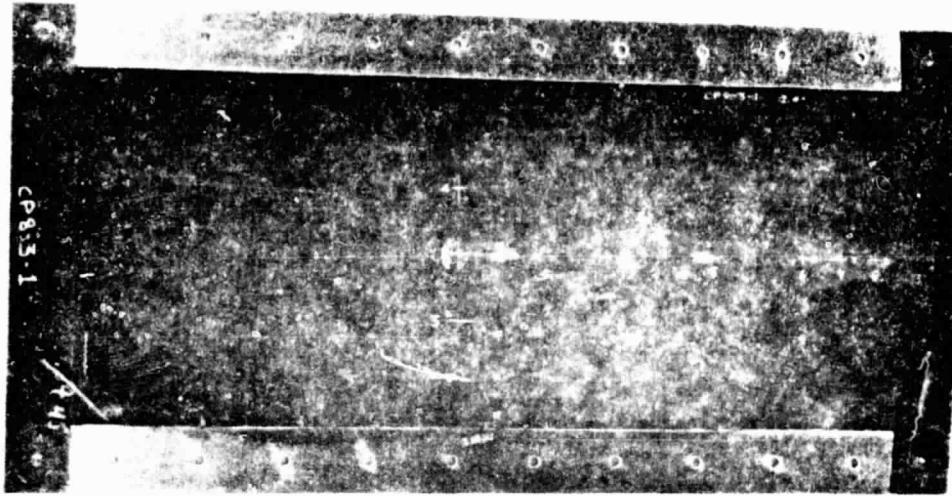
Convex Surface
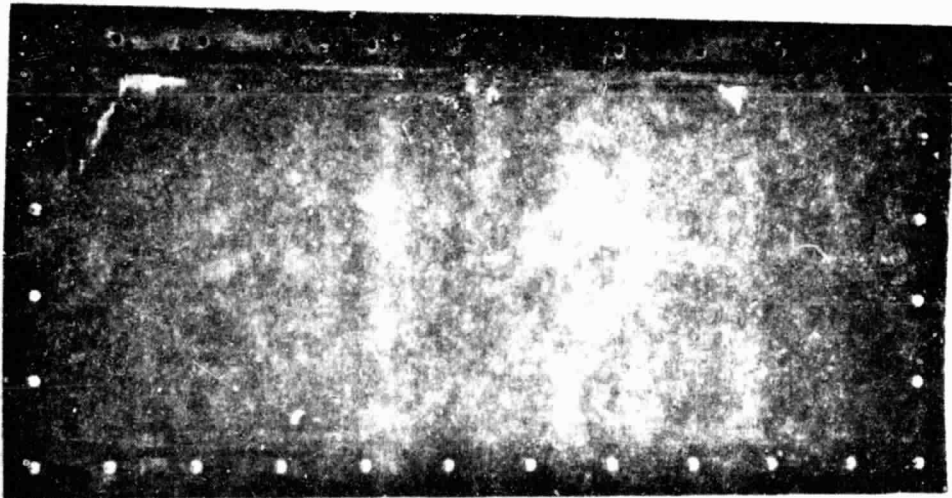
Concave Surface

Figure A8.- Graphite-epoxy Specimen G6; $[90/0/\pm45]_s$
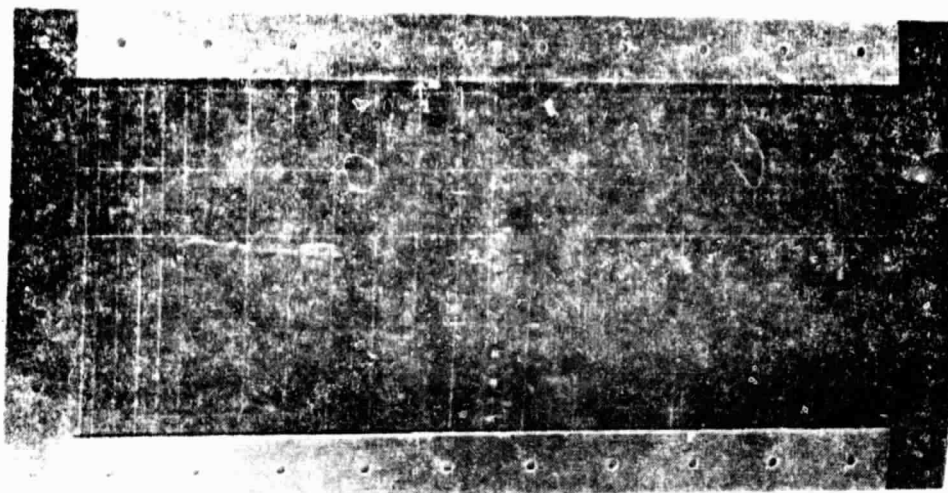
Convex Surface
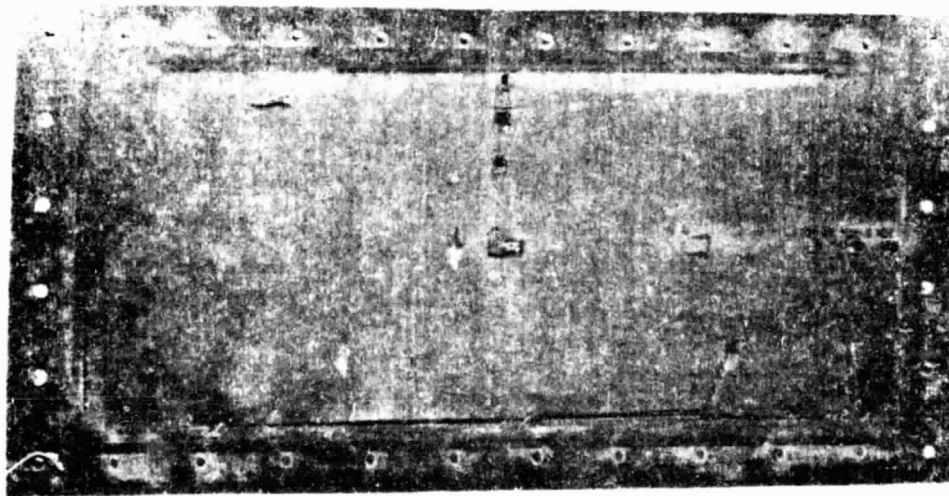
Concave Surface

Figure A9.- Graphite-epoxy Specimen G7; [90/0/±45]$_s$

Convex Surface
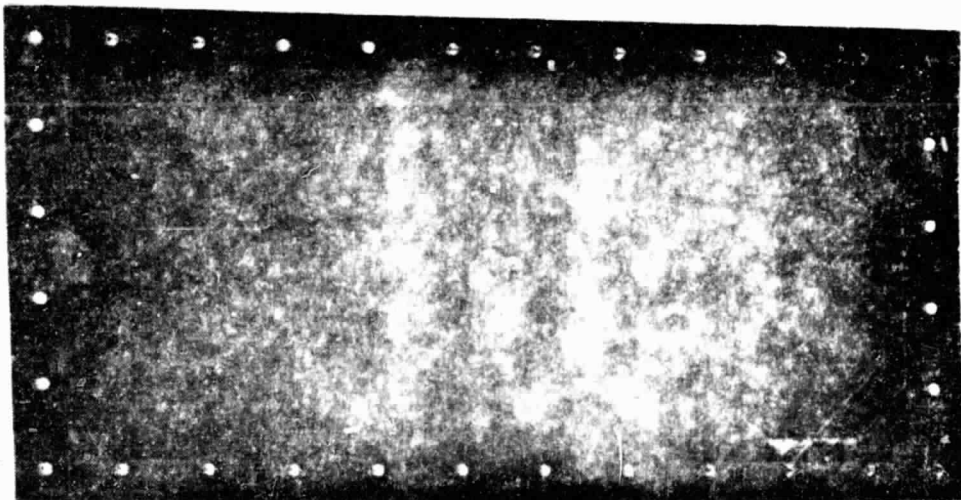
Concave Surface

Figure A10.- Graphite-epoxy Specimen G8; $[\pm45]_{2s}$
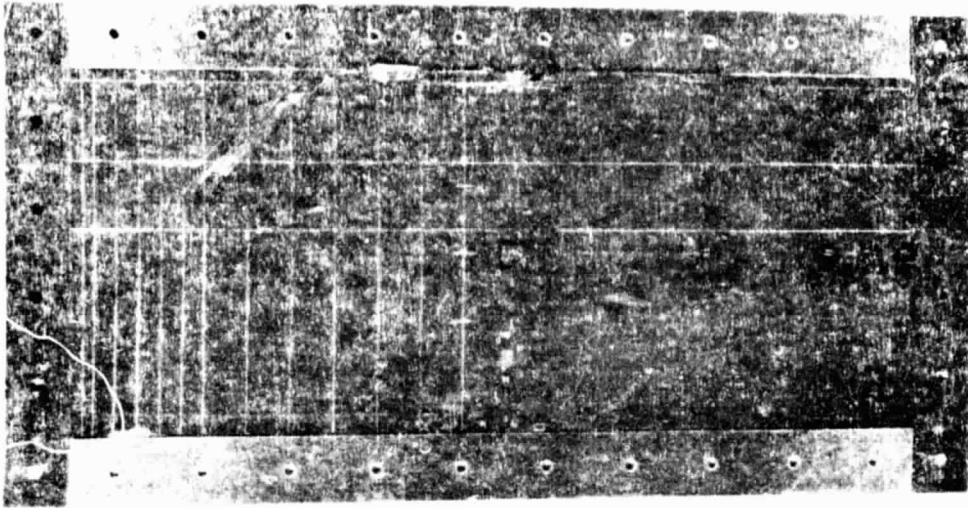
Convex Surface
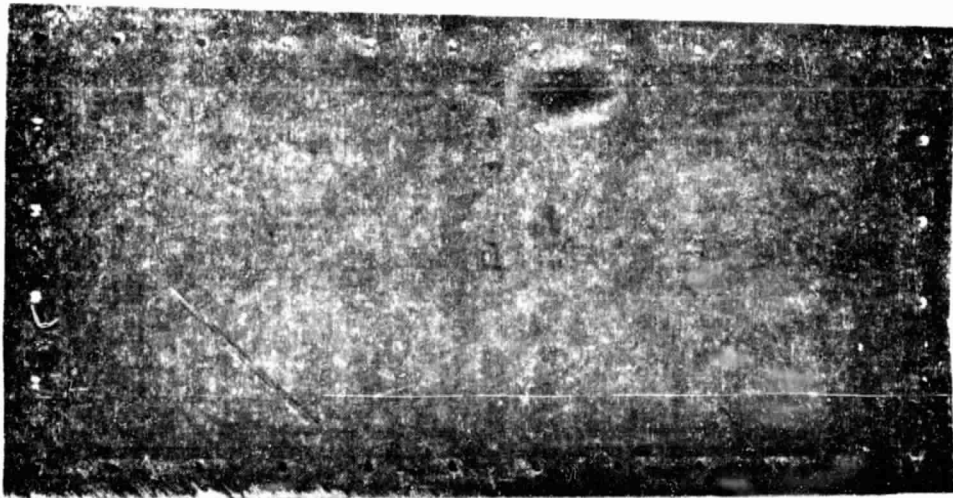
Concave Surface

Figure A11.- Graphite-epoxy Specimen G9; $[\pm 45/\pm 45/90_2/0_2]_s$
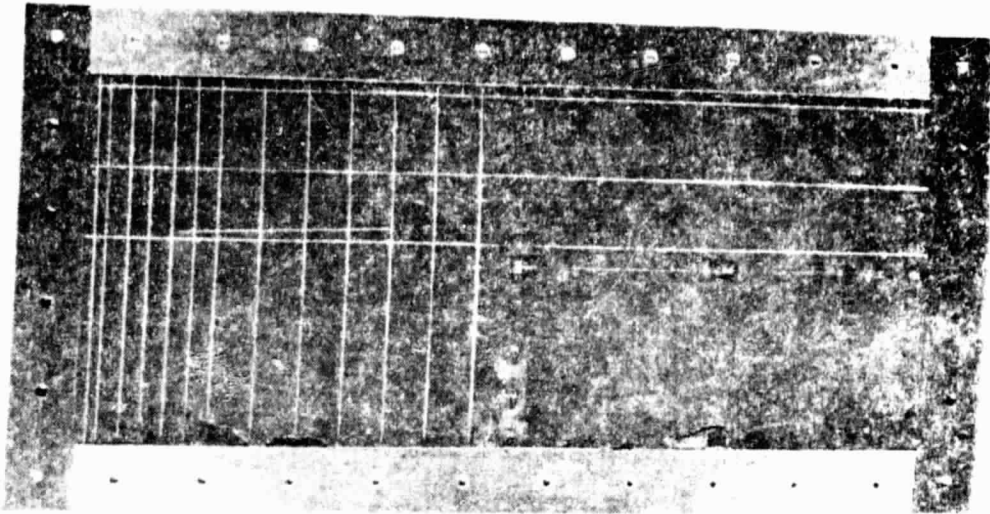
Convex Surface

Concave Surface

Figure A12.- Graphite-epoxy Specimen G10; $[\pm45/\pm45/90_2/0_2]_s$
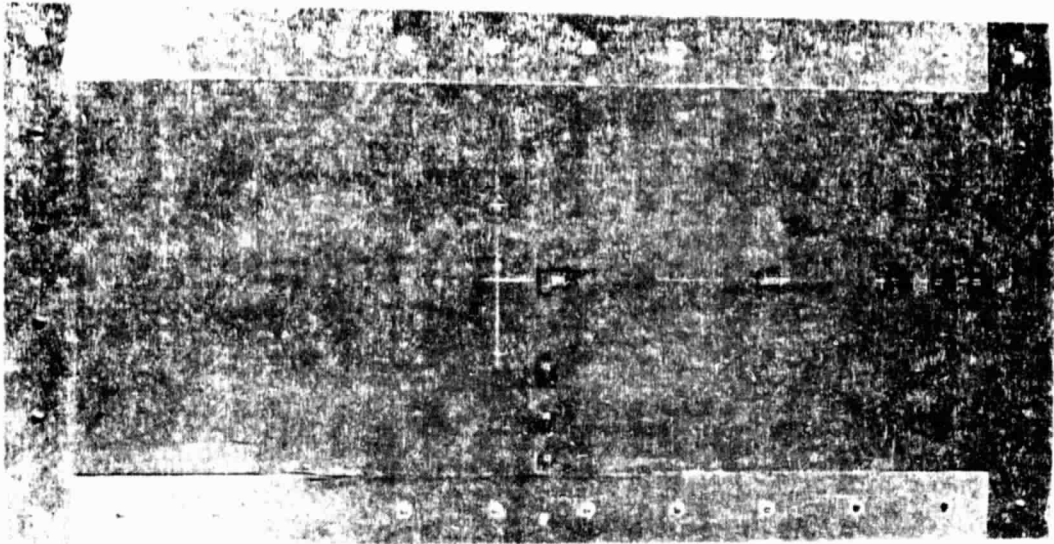
Convex Surface
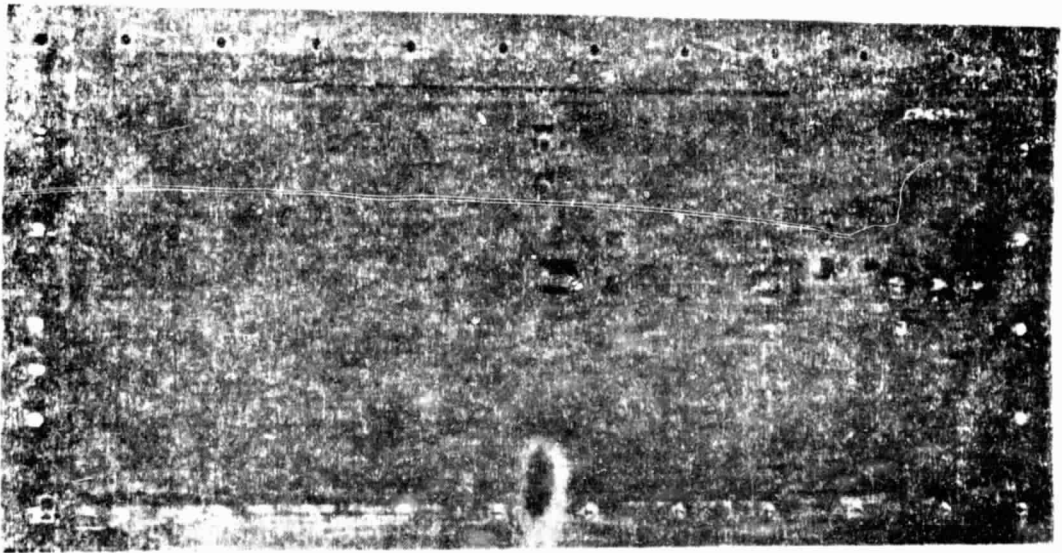
Concave Surface

Figure A13.- Graphite-epoxy Specimen G11; $[90_2/\pm45/\pm45/0_2]_s$

APPENDIX   B

STRAIN GAGE DATA
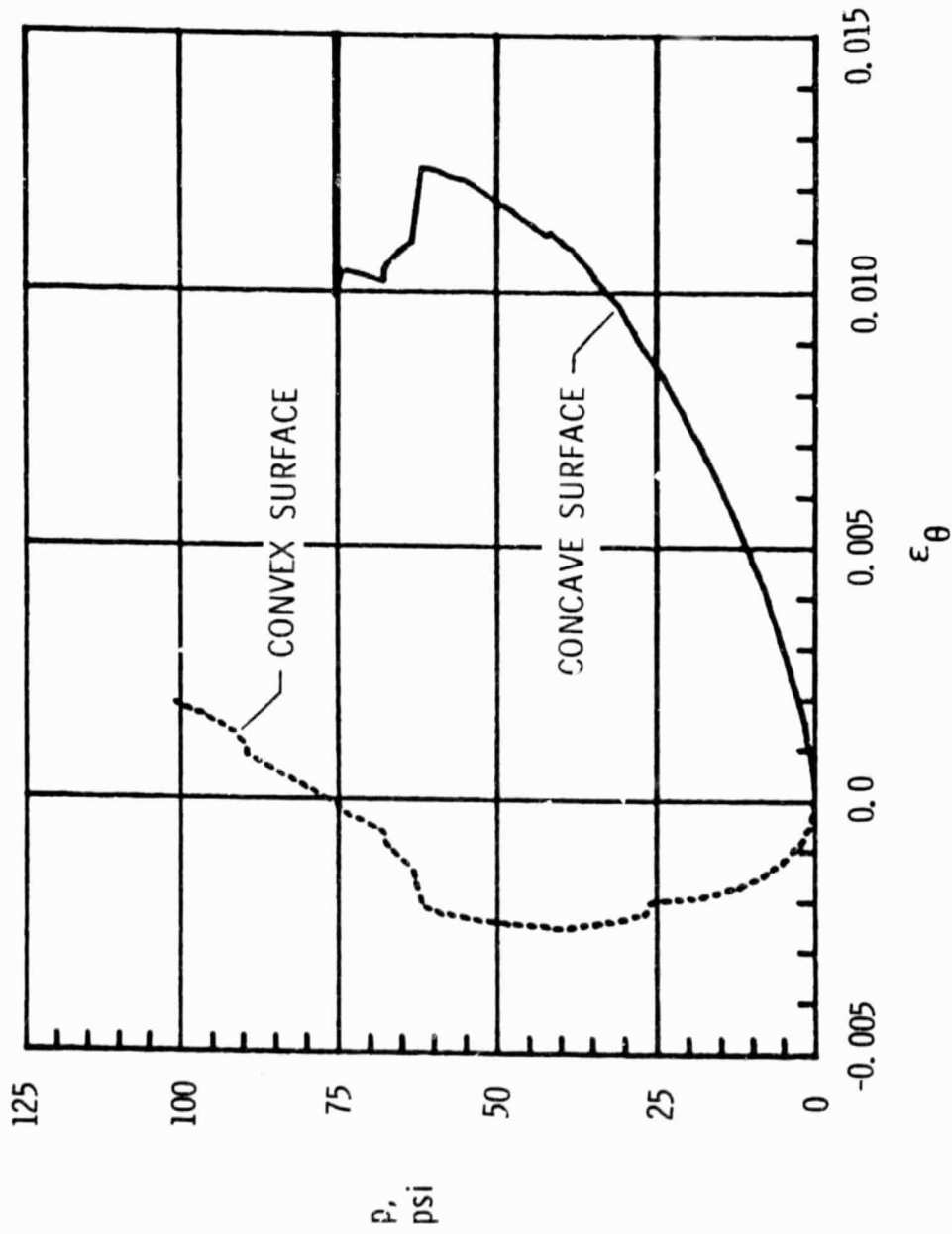
Figure B1.- Circumferential strain response of back-to-back gages located 0.030 inches from the straight edge of specimen G2.
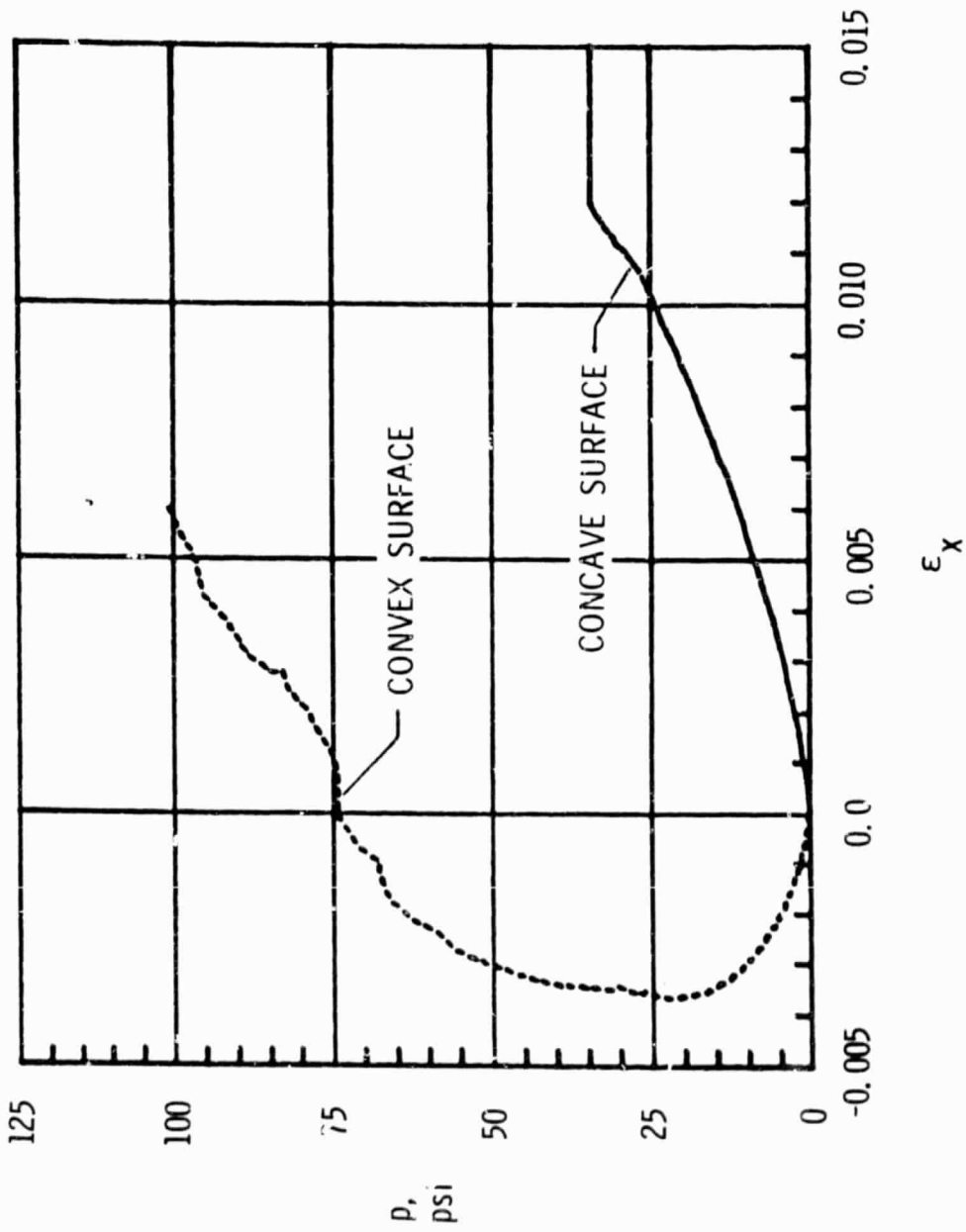
Figure B2.- Axial strain response of back-to-back gages located 0.040 inches from the curved edge of specimen G2.
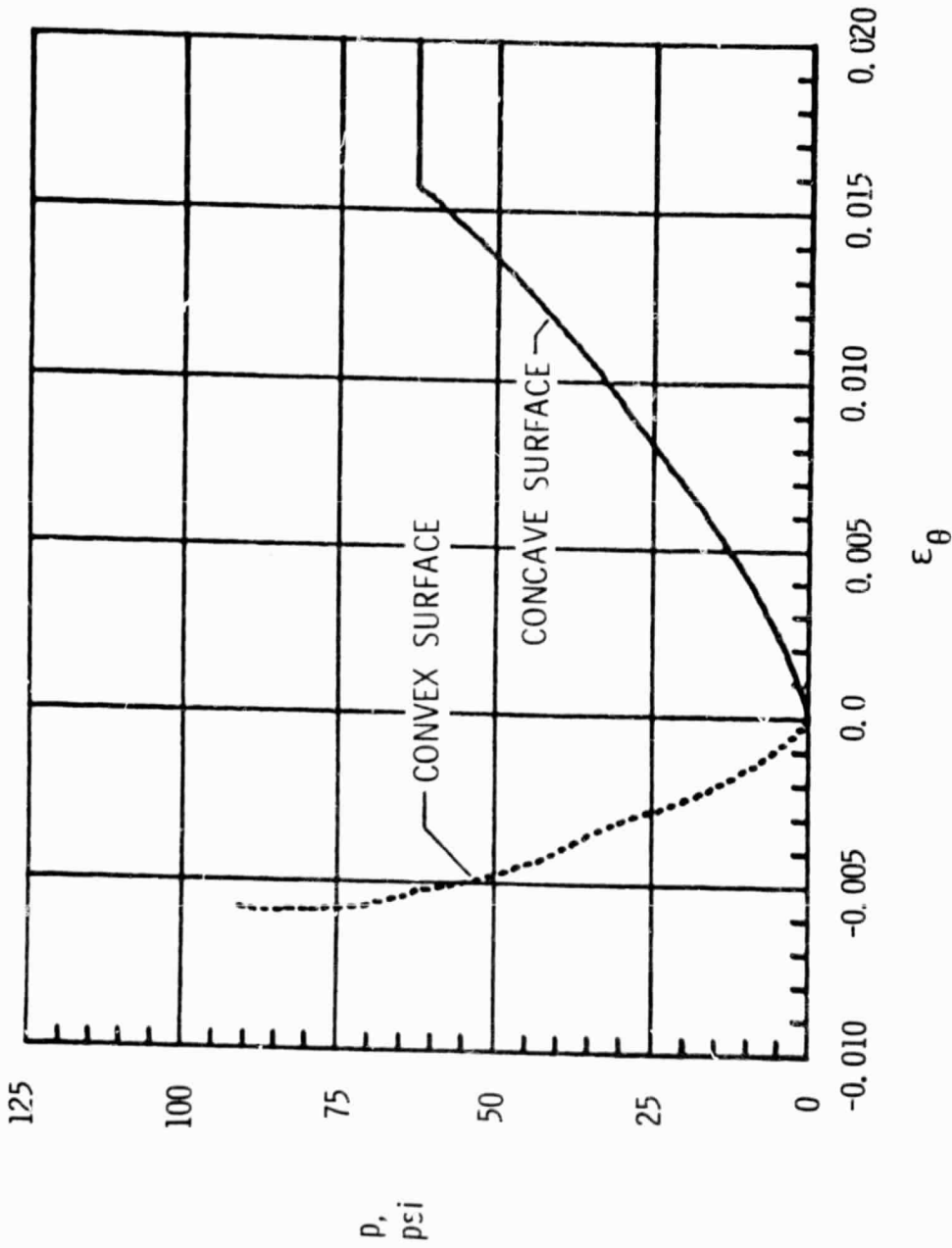
Figure B3.- Circumferential strain response of back-to-back gages
located as close as possible to the straight edge of
specimen G4.
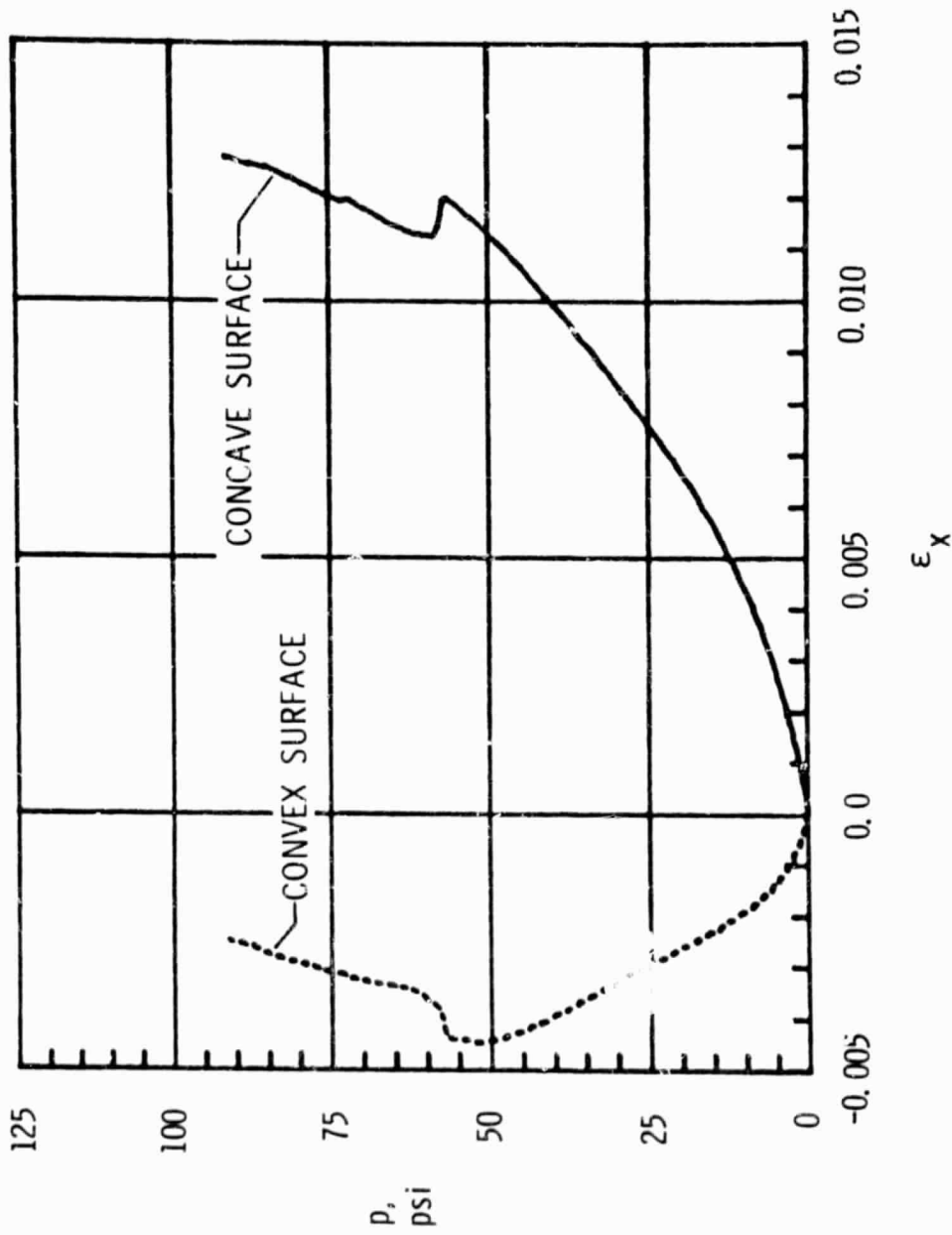
Figure B4.- Axial strain response of back-to-back gages located 0.050 inches from the curved edge of specimen G4.
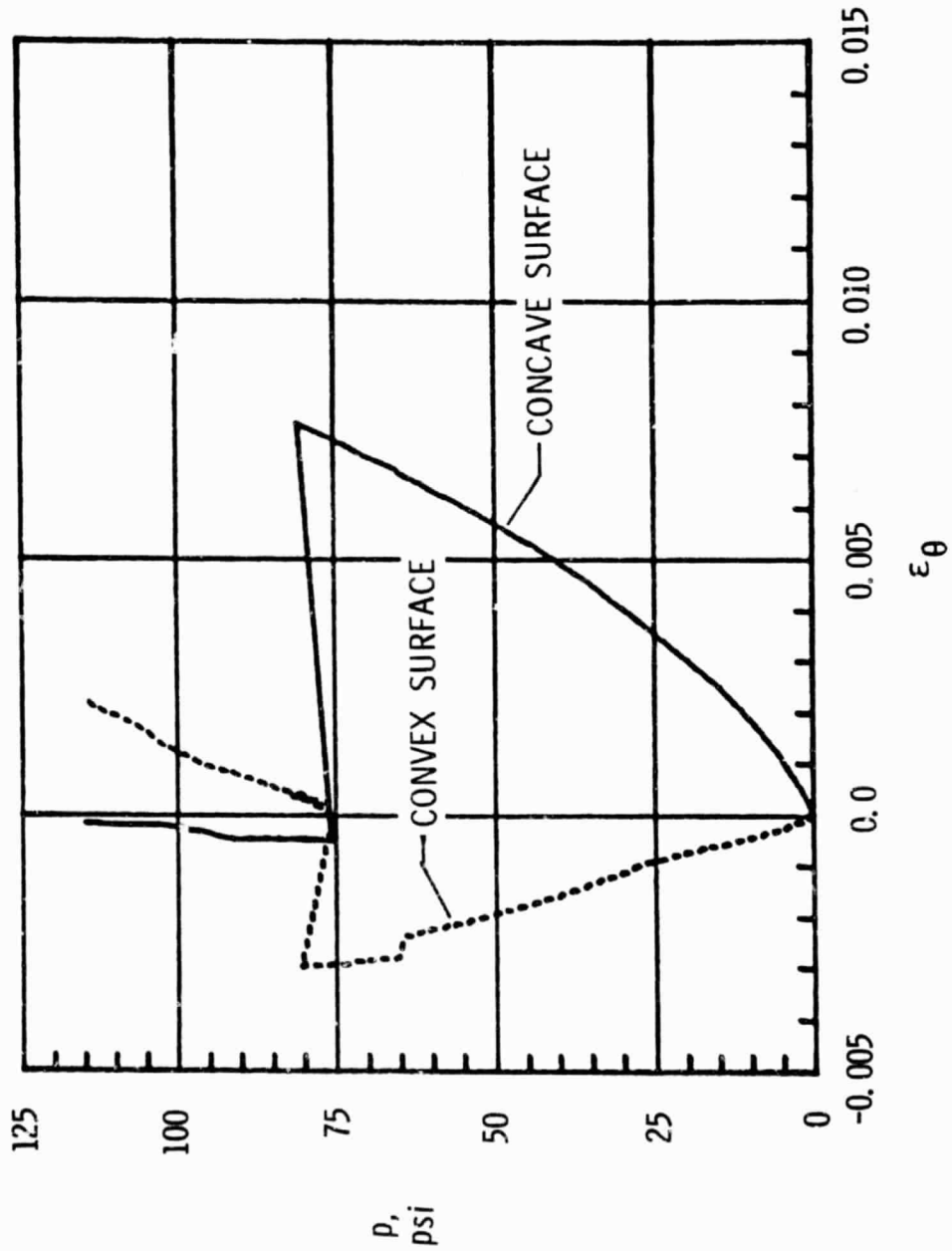
Figure B5.- Circumferential strain response of back-to-back gages located 0.125 inches from the straight edge of specimen G7.

C-3
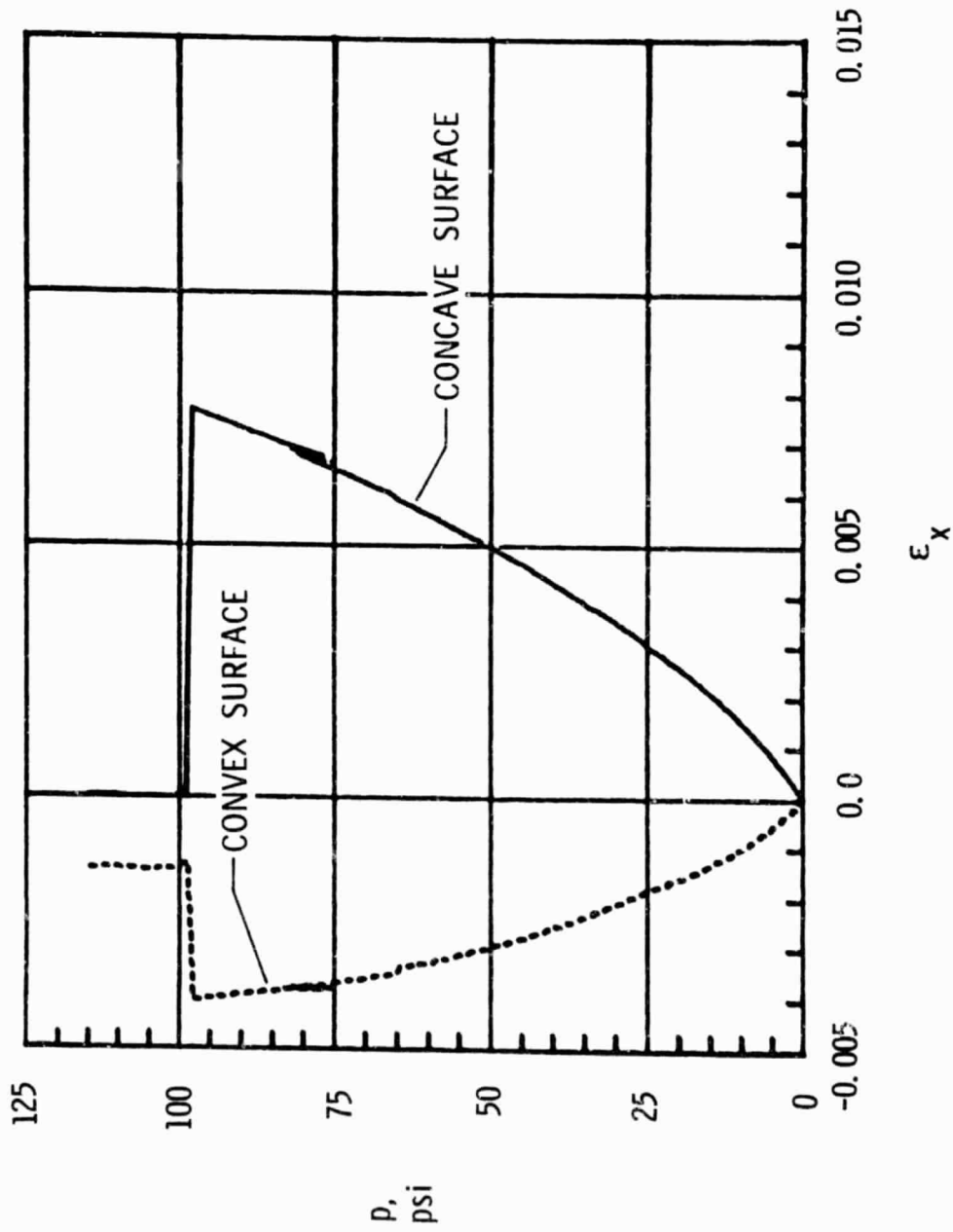
Figure B6.– Axial strain response of back-to-back gages located 0.125
inches from the curved edge of specimen G7.
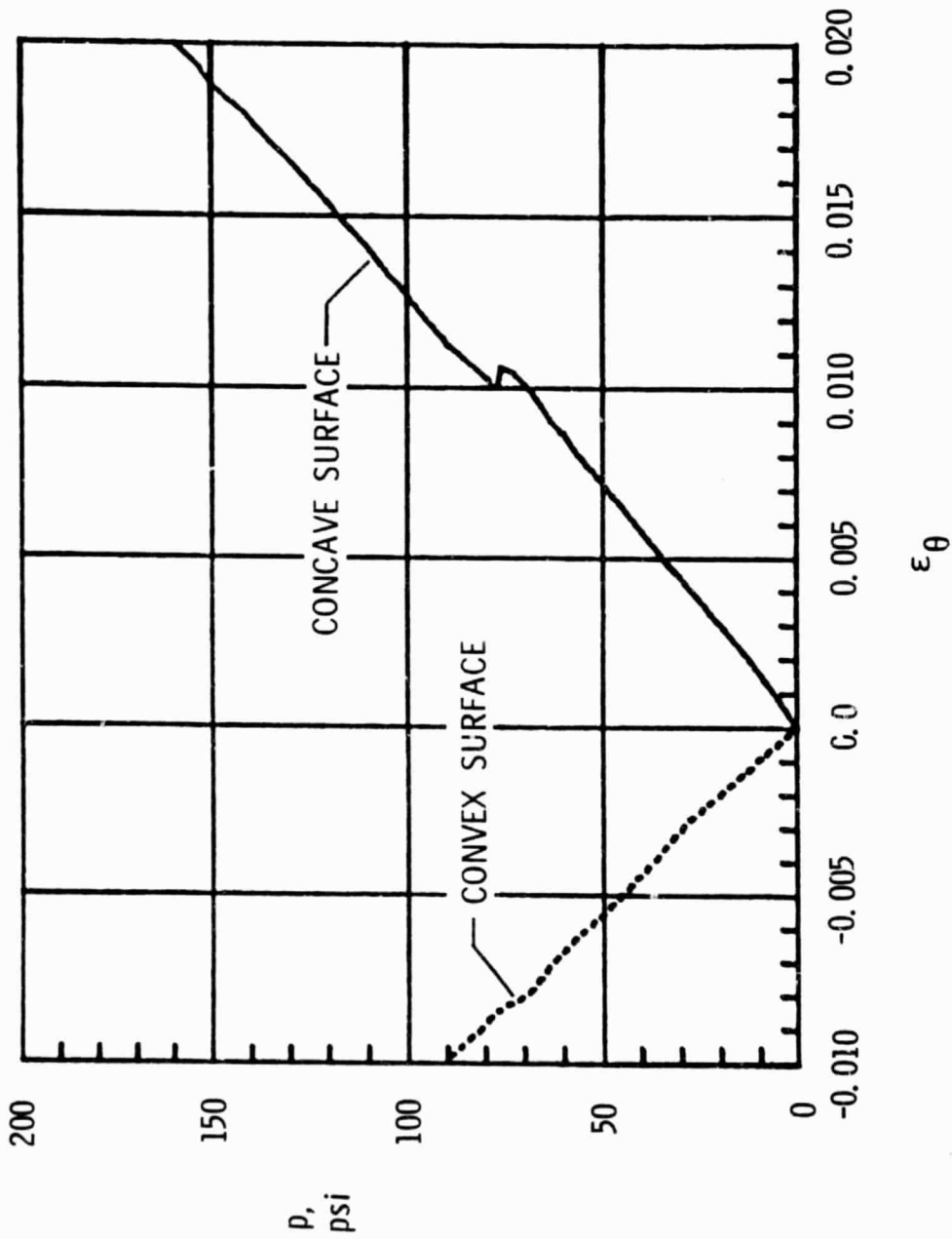
Figure B7.- Circumferential strain response of back-to-back gages located 0.020 inches from the straight edge of specimen G9.
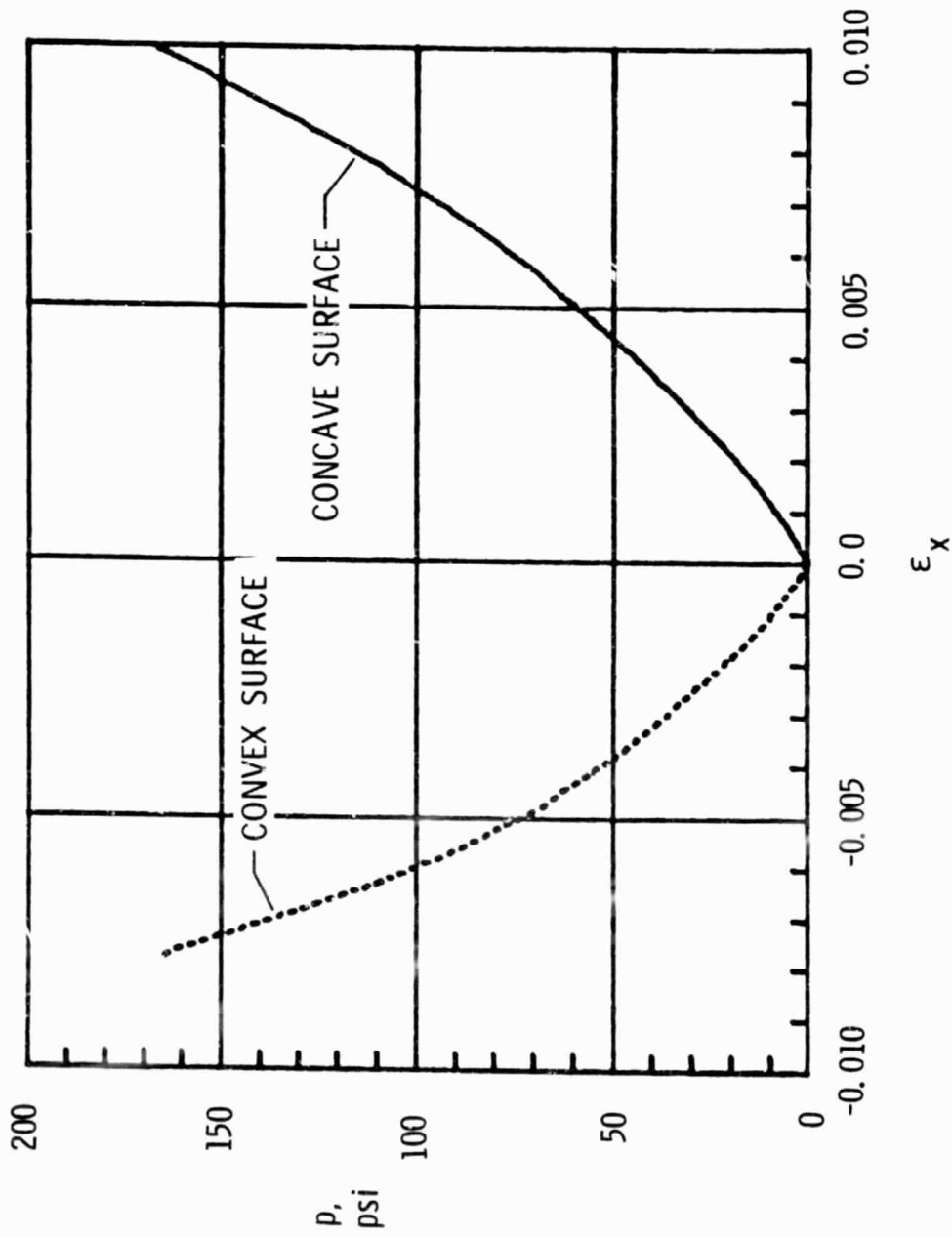
Figure B8.- Axial strain response of back-to-back gages located 0.125 inches from the curved edge of specimen G9.
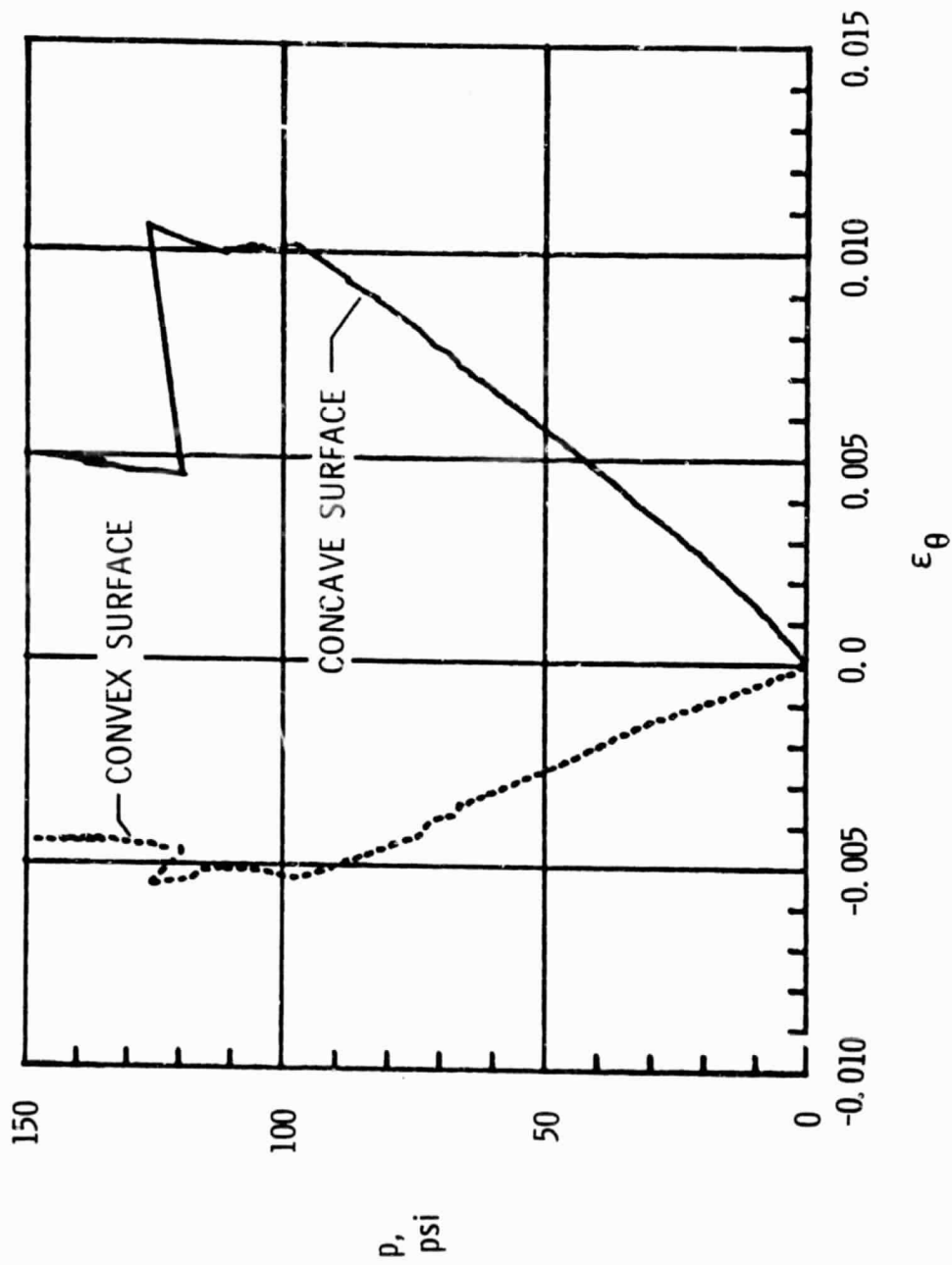
Figure B9.– Circumferential strain response of back-to-back gages located 0.030 inches from the straight edge of specimen G10.
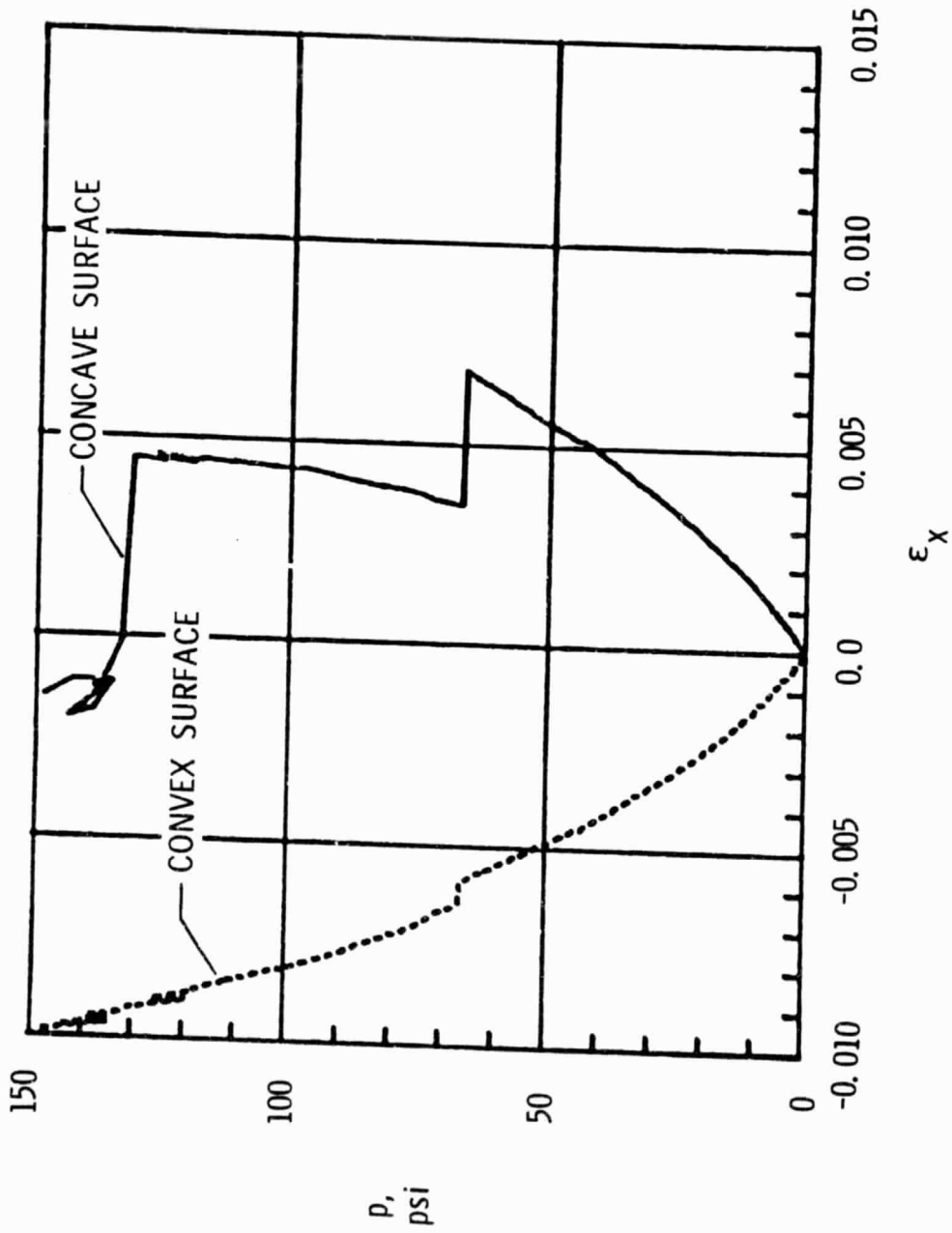
Figure B10.- Axial strain response of back-to-back gages located 0.125 inches from the curved edge of specimen G10.

APPENDIX   C

FAILURE MODE CRITERIA

Appendix C. Failure Mode Criteria

The following failure criteria are used to predict different failure modes. Values equal to or greater than one indicate failure in all the criteria. These failure criteria were extracted from Reference [21].

Tensile Fiber Mode

$$\frac{\sigma_{11}}{X_t} = 1$$

Compressive Fiber Mode

$$\frac{\sigma_{11}}{X_c} = 1$$

Tensile Matrix Mode

$$\frac{\sigma_{22}^2}{Y_t} + \frac{\tau_{12}^2}{S_{xy}^2} = 1$$

Compressive Matrix Mode

$$1 - \left(\frac{Y_c}{2S_{xy}}\right)^2 \frac{\sigma_{22}}{Y_c} + \frac{\sigma_{22}^2}{4S_{xy}^2} + \frac{\tau_{12}^2}{S_{xy}^2} = 1$$

Tensile Interlaminar Mode

$$\frac{\sigma_{33}^2}{Z_t^2} + \frac{(\tau_{13}^2 + \tau_{23}^2)}{S_{yz}^2} = 1$$

Compressive Interlaminar Mode

$$1 - \left(\frac{Z_c}{2S_{yz}}\right)^2 \frac{\sigma_{33}}{Z_c} + \frac{\sigma_{33}^2}{4S_{yz}^2} + \frac{(\tau_{13}^2 + \tau_{23}^2)}{S_{yz}^2} = 1$$

APPENDIX D

THREE-DIMENSIONAL TSAI-WU FAILURE CRITERION

Appendix D. Three-Dimensional Tsai-Wu Failure Criterion

The Tsai-Wu failure criterion is a special case of the tensor polynominal failure criterion where only linear and quadratic terms are included. The Tsai-Wu failure criterion is commonly used for two-dimensional stress states but can be expanded to three-dimensional stress states. For three-dimensional stress states the Tsai-Wu failure criterion has the following form

$$F_1\sigma_{11} + F_2\sigma_{22} + F_3\sigma_{33} + F_{11}\sigma_{11}^2 + 2F_{12}\sigma_{11}\sigma_{22} + 2F_{13}\sigma_{11}\sigma_{33}$$
$$+ F_{22}\sigma_{22}^2 + 2F_{23}\sigma_{22}\sigma_{33} + F_{33}\sigma_{33}^2 + F_{44}\tau_{23}^2 + F_{55}\tau_{31}^2$$
$$+ F_{66}\tau_{12}^2 = 1. \tag{D.1}$$

In the above expression the coefficients F_4, F_5 and F_6 which correspond to the linear τ_{23}, τ_{31} and τ_{12} terms are zero. These must be zero since the shear strength is independent of the loading direction. The coefficients in the failure criterion are determined in terms of the strength properties given in Table 10 by considering one-dimensional loadings. Consider the case of a tensile loading in the fiber- or one-direction such that

$$\sigma_{11} \neq 0 \quad \text{and} \quad \sigma_{22} = \sigma_{33} = \tau_{23} = \tau_{31} = \tau_{12} = 0. \tag{D.2}$$

At failure $\sigma_{11} = X_t$ and the Tsai-Wu failure criterion becomes

$$F_1 X_t + F_{11} X_t^2 = 1 \tag{D.3}$$

Next compressive loading in the fiber direction is considered where at failure $\sigma_{11} = X_c$ and the Tsai-Wu failure criterion becomes

$$F_1 X_c + F_{11} X_c^2 = 1 \tag{D.4}$$

The strength coefficients F_1 and F_{11} are determined by solving Eqs. (D.3) and (D.4) simultaneously.

$$F_1 = \frac{1}{X_t} + \frac{1}{X_c} \tag{D.5}$$

and

$$F_{11} = - \frac{1}{X_t X_c} \tag{D.6}$$

Similarly it may be easily shown that

$$F_2 = \frac{1}{Y_t} + \frac{1}{Y_c} \tag{D.7}$$

and

$$F_{22} = - \frac{1}{Y_t Y_c} \tag{D.8}$$

from consideration of tensile and compressive loadings in the transverse or two-direction. Furthermore two additional coefficients may be determined from loadings in the thickness direction.

$$F_3 = \frac{1}{Z_t} + \frac{1}{Z_c} \tag{D.9}$$

and

$$F_{33} = - \frac{1}{Z_t Z_c} \tag{D.10}$$

By considering the three possible shear loadings separately the following coefficients may be determined

$$F_{44} = \frac{1}{(S_{yz})^2} \tag{D.11}$$

$$F_{55} = \frac{1}{(S_{xz})^2}$$

and

$$F_{66} = \frac{1}{(S_{xy})^2}$$

The coefficients F_{12}, F_{23} and F_{13} may only be determined from biaxial stress states. Such tests are very difficult to conduct and these coefficients were assumed to be equal to the following values

$$F_{12} = F_{23} = F_{13} = -0.58 \times 10^{-10}$$

This value was found to give good correlation with off-axis tests for boron/epoxy by Pipes and Cole [22]. when used for F_{12} in the two-dimensional Tsai-Wu criteria.